Czech Technical University in Prague
Faculty of Nuclear Sciences and Physical Engineering
Department of Solid State Engineering

Defects in nitride-based scintillation heterostructures

Dissertation

Ph.D. student: Ing. František Hájek

Supervisor: Ing. Jiří Oswald, CSc.

Supervisor-specialist: Mgr. Vlastimil Křápek, Ph.D.

Year: 2023

Bibliografický záznam

Autor:	Ing. František Hájek
	České vysoké učení technické v Praze
	Fakulta jaderná a fyzikálně inženýrská
	Katedra inženýrství pevných látek

Název Práce:	Defekty ve scintilátorových strukturách na bázi nitridů
Studijní program:	Aplikace přírodních věd
Studijní obor:	Fyzikální inženýrství

Školitel:	Ing. Jiří Oswald, CSc.
	Fyzikální ústav Akademie věd České republiky
Školitel specialista:	Mgr. Vlastimil Křápek, Ph.D.
	Vysoké učení technické v Brně

Akademický rok:	2022/2023
Počet stran:	114
Klíčová slova:	Scintilátor, luminiscence, nitridy, defekty

Bibliographic Entry

Author:	Ing. František Hájek
	Czech Technical University in Prague
	Faculty of Nuclear Sciences and Physical Engineering
	Department of Solid State Engineering
Title of Dissertation:	Defects in nitride-based scintillation heterostructures
Degree Programme:	Applications of Natural Sciences
Field of Study:	Physical Engineering
Supervisor:	Ing. Jiří Oswald, CSc.
	Institute of Physics of the Czech Academy of Sciences
Supervisor specialist:	Mgr. Vlastimil Křápek, Ph.D.
	University of Technology Brno
Academic Year:	2022/2023
Number of Pages: 114	
Keywords: Scintillator, luminescence, nitrides, defects	

Abstrakt

Rostoucí poptávka po vysoce účinných scintilátorech potřebných v aplikacích vyžadujících navíc i rychlou odezvu, jako je například pozitronová emisní tomografie, vede ke zkoumání nových tříd materiálů jako potenciálních scintilátorů. Jedním ze slibných kandidátů na rychlé scintilátory jsou heterostruktury na bázi nitridů. Pro zamýšlenou aplikaci je však třeba eliminovat defekty způsobující luminiscenční pásy s dlouhými dosvity nebo defekty chovající se jako nezářivá centra. V této práci jsou studovány nejběžnější bodové defekty ve scintilátorových strukturách InGaN/GaN vypěstovaných metodou organokovové epitaxe z plynné fáze a jsou navrženy metody eliminace jejich negativního vlivu. Hlavní část práce se skládá ze 6 článků.

Je ukázáno, že pomalou žlutou luminiscenci z vrstev GaN způsobenou uhlíkovým defektem lze urychlit na přijatelnou úroveň pomocí n-typového dopování. Dále jsou představeny modely popisující zkrácení doby dosvitu s vyšší koncentrací dopování založené na rekombinaci buď donoro-akceptorových párů (DAP) nebo elektron-akceptorové rekombinaci a tyto modely jsou porovnány s experimentálními daty.

Následně je nalezen a potlačen zdroj kontaminace Zn v InGaN kvantových jamách. Příměs Zn není ve vzorku rozložena homogenně, ale je přítomna především v InGaN kvantových jamách, přičemž největší koncentrace Zn se nachází ve spodní InGaN kvantové jámě vyrostlé na GaN podkladové vrstvě. Hloubkový profil je modelován s ohledem na různé formační energie Zn_{Ga}, které závisí na dopování Si, polarizačními poli na rozhraní InGaN/GaN a povrchovém potenciálu.

Luminiscence Zn pásu je rovněž studována pomocí časově rozlišené radio- a fotoluminiscence a na intenzitě excitace závislé fotoluminiscence. Velké posuny pásu k vyšším energiím s rostoucí intenzitou excitace jsou vysvětleny pomocí DAP modelu. Výsledky ukazují, že za účinnou luminiscenci tohoto pásu může efekt kvantování způsobující silnější lokalizaci elektronů vázaných na donorech.

Vakance Ga jako potenciální nezářivá centra jsou zkoumány pozitronovou anihilační spektroskopií (PAS). Navzdory očekávání je zjištěno, že intenzita luminescence GaN excitonu (či volných nosišů) roste s vyšší koncentrací Ga vakancí. Předpokládá se, že hlavními nezářivými centry v GaN mohou být komplexy Ga vakancí s vodíkem. Ty bohužel nelze pozorovat technikou PAS.

Proto je použita nepřímá metoda pro studium komplexů vodíku s vakancemi. Hmotnostní spektroskopie sekundárních iontů ukazuje, že intenzita luminiscence klesá s vyšší koncentrací vodíku ve vzorku. Navíc je pozorována konkurence mezi koncentrací vodíku a zinku, což znamená, že Ga vakance mohou být vyplněny atomy Zn, které brání tvorbě komplexu vodík-vakance.

Ná základě výsledků jsou navrženy optimální podmínky růstu pro jednotlivé vrstvy heterostruktury. Tyto podmínky však vedou k tvorbě tzv. V-pitů. Na závěr jsou tedy diskutovány problémy morfologie a jejich souvislost s optimálními růstovými podmínkami z hlediska bodových defektů.

Abstract

Increasing demand for efficient scintillators sought in applications requiring fast response, like time-of-flight positron emission tomography, has led to exploring a new class of scintillators. One of the promising candidates for fast scintillators are nitride-based heterostructures. However, for the intended application, the defects producing luminescence bands with long decay times or defects acting as non-radiative centres must be eliminated. In this thesis, the most abundant point defects in InGaN/GaN scintillator structures grown by Metal Organic Vapour Phase Epitaxy are studied and the methods for elimination their negative influence are suggested. The main part of the thesis is composed of 6 papers.

It is shown that slow yellow luminescence from GaN layers caused by carbon defect can be accelerated to acceptable range by n-type doping. Moreover, a model describing the decrease of the decay time with higher doping concentration based on the donor-acceptor pair (DAP) recombination or electron-acceptor recombination is introduced and compared with experimental data.

Next, a source of Zn contamination in InGaN quantum wells (QWs) is found and supressed. The Zn impurity is not distributed homogeneously in the sample but is present mainly in the InGaN QWs, the largest Zn concentration being found in the bottom InGaN QW grown atop the GaN buffer layer. The depth profile is modelled taking into account different Zn_{Ga} formation energies which are altered by intentional Si doping and polarization fields at the InGaN/GaN interfaces and surface potential.

The luminescence of Zn band is also studied by time-resolved radio- and photoluminescence and excitation intensity-dependent photoluminescence techniques. Large blue-shifts of the band with increasing excitation intensity are explained by DAP model considering quantum confinement effect causing stronger localization of electrons bound to donors.

As potential non-radiative centres, Ga vacancies are studied by positron annihilation spectroscopy (PAS). Surprisingly, it is found the luminescence intensity of GaN near-band-edge emission is increasing with higher Ga vacancy concentration. It is suggested that complexes of Ga vacancies with hydrogen might be the main non-radiative centres in GaN. Unfortunately, these cannot be observed with PAS technique.

Thus, different method for studying hydrogen-vacancy complexes is introduced. Secondary ion mass spectroscopy reveals that luminescence intensity is decreasing with higher hydrogen concentration in the sample. Moreover, a competition between hydrogen and zinc concentration is observed meaning that Ga vacancies might be filled with Zn atoms prohibiting the hydrogen-vacancy complex formation.

From the results, the optimal growth conditions for particular layers of the structure are suggested. However, these conditions lead to formation of so-called V-pits. Therefore, the morphology problems and their connection with the optimal growth conditions from the point defect perspective are discussed.

Table of contents

Sworn declaration:

I declare under oath that I have prepared the paper at hand independently and without the help of others and that I have not used any other sources and recourses than the ones stated. Parts that have been taken literally or correspondingly from published or unpublished texts or other sources have been labelled as such. This paper has not been presented to any examination board in the same or similar form before.

Measurements:

František Hájek (author): Characterization by means of electron microscopy, photoluminescence (excitation wavelength 375 nm), time-resolved photoluminescence (paper 3), Nextnano simulations
Alice Hospodková, Tomáš Hubáček, Markéta Slavická-Zíková, Jiří Pangrác: Samples preparation
Jiří Oswald: Photoluminescence (excitation wavelength 375 nm)
Karla Kuldová, Radek Novotný: Photoluminescence measurements (excitation wavelength 325 nm)
EAG laboratories: Secondary ion mass spectroscopy (papers 1, 2, 3, 4, 5)
Jakub Čížek, Maciej O. Liedke, Eric Hirschmann, Maik Butterling, Andreas Wagner: Positron annihilation spectroscopy (papers 4, 5)
Vítězslav Jarý: Time-resolved photoluminescence spectroscopy (paper 1)
Zuzana Gedeonová: Transport measurements
Vladimír Babin, Maxim Buryi: Thermally stimulated luminescence, time-resolved radioluminescence (paper 1)
Tomáš Vaněk, Petr Bábor: Secondary ion mass spectroscopy (paper 6)
Filip Dominec, Robert Horešovský: Fitting of PL spectra (paper 2)
Gilles Ledoux, Christophe Dujardin: Excitation-emission maps, time-resolved radioluminescence (paper 3)
Pavel Kejzlar: White-light interferometry (paper 6)
Alexander Vetushka: Atomic probe tomography
Artur Lachowski: Transmission electron microscopy (paper 6)

Date, signature

List of abbreviations

Abbreviation	Full collocation	Abbreviation	Full collocation
BB1	Blue band (from Zn)	SEM	Scanning electron microscopy
BB_C	Blue band (from C)	SIMS	Secondary ion mass spectroscopy
CL	Cathodoluminescence	TEGa	Triethylgallium
DAP	Donor-acceptor pair	TEM	Transmission electron microscopy
DFT	Density functional theory	TMGa	Trimethylgallium
e-A	Electron-acceptor	TMIn	Trimethylindium
FTIR	Fourier transform infrared spectroscopy	TOF-PET	Time-of-flight positron emission tomography
HEMT	High electron mobility transistor	TSL	Thermally stimulated luminescence
HVPE	Hydride Vapour Phase Epitaxy	UL	Underlayer
LD	Laser diode	(VE)PAS	(Variable energy) positron annihilation spectroscopy
LY	Light yield	XRD	X-Ray diffraction
MOVPE	Metal Organic Vapour Phase Epitaxy	YB	Yellow band
PL	Photoluminescence	ZPL	Zero phonon line
PMT	Photomultiplier tube	ZnB	Zn band (in InGaN)

1 Introduction

1.1 Brief history of nitrides from application point of view

Binary compounds of Ga, In, Al and B with N called nitrides and their ternary alloys occupy the second largest market share after the traditional semiconductor, silicon. However, the tremendous success of nitrides was hardly imaginable as late as 1980s. The interest for the principal representant of the nitride family, gallium nitride (GaN), was driven by the optoelectronic applications, mainly the blue LEDs and laser diodes (LDs). In late 1970s, luminescence properties of GaN doped or implanted with variety of elements were studied and even electroluminescence was achieved [1–4]. Unfortunately, the efficiency of these first LEDs was too low for commercial applications and many believed that it cannot be improved significantly [5]. The most serious problems were lack of suitable substrate for GaN growth resulting in heteroepitaxial growth with large dislocation densities and inefficient p-type doping. Despite the general scepticism in 1980s, several scientists endured and discovered ways how to eliminate the problems behind the low GaN-based LEDs efficiency. Three of them were awarded by Nobel prize in 2014 [6]. The first blue LEDs based on InGaN/GaN heterostuctures became commercially available in middle 1990s.

The blue component of the spectra is necessary for white light illumination. First attempts to get the white light emission from InGaN/GaN structure included doping of InGaN layers by Zn and Si [7,8]. The doping led to white light emission but only at low excitation intensities. The luminescence band caused by Zn and Si doping was shifting with higher excitation intensities to higher energies which resulted in solely blue emission. However, the shifting of the emission was not satisfactorily explained that time. The commercially available white LEDs nowadays usually contain a phosphorus layer like YAG [9] or $(Sr,Ba,Ca)_3SiO_5$:Eu [10] which converts the blue light into the yellow or amber one. The full-nitride white LEDs with different nitride layers producing the white light are still under development [11,12]. Hot topic for future market are µLEDs which are keystone for high-resolution, high-efficient, long-lifetime displays [13,14].

Besides optoelectronic devices, nitrides are widely used in radiofrequency, high-temperature and power electronics. The main advantages for GaN over and related nitrides over traditional Si devices are high saturation velocity, high breakdown field and high temperature operation range [5]. The superior characteristics of GaN based electronics are connected with possibility to create nitride heterostructures. Devices composed of GaN/AlGaN heterostructure rely on large conduction band offset and strong polarization field at the interface which confines electrons in the channel near this interface. Such devices with large 2D electron density (typically in order of 10^{13} cm^{-2} [15]) alongside with the high mobility (reaching more than 2000 $cm^2V^{-1}s^{-1}$ [16]) at room temperature) are called high

electron mobility transistors (HEMTs). It is expected that the market with HEMTs will grow more steeply than those with optoelectronic devices in future (Fig. 1) [17].

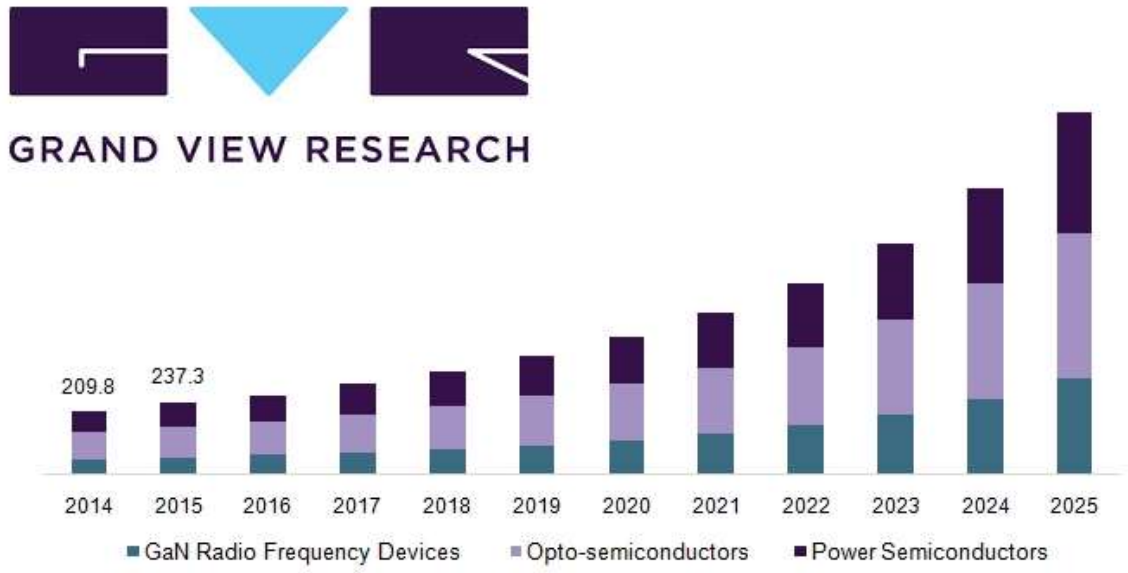

Figure 1: Prediction of nitride market evolution in the near future. Reproduced from [17].

Moreover, it is predicted that GaN-based transistors will play dominant role in applications requiring simultaneous high operation frequency and high breakdown voltage. Typical example are networks of a new generation [18,19].

Emerging optoelectronic applications under development include also UV detectors [20,21], UV LEDs [22,23] and lasers [24], photovoltaic cells [25,26] or scintillators [27–29], as will be discussed in detail in chapter 1.4.

1.2 Nitrides: basic properties

Elements of the group III in periodic table may form binary compounds with nitrogen commonly referred as nitrides. Because this work is focused on scintillator application, the relevant nitrides are only InN, GaN and AlN and their alloys which are grown as single-crystals. Therefore, speaking about nitrides will refer only to these ones. The possible crystal forms for these nitrides are wurtzite, sphalerite or NaCl-type. For the common ranges of temperatures and pressure, the wurtzite is the stable one [30], although some attempts to access sphalerite forms were successful [31,32]. The bond has covalent character with a little addition of ionic bond character. The ionic contribution C^{Ion} is increasing in the order $C_{AlN}^{Ion} < C_{InN}^{Ion} < C_{GaN}^{Ion}$ [30]. All these nitrides are considered semiconductors, although especially p-type doping by conventional methods of AlN is difficult [33], with the direct band gap.

Property	InN	GaN	AlN
Lattice parameter a [nm]	0.386	0.320	0.311
Lattice parameter c [nm]	0.580	0.522	0.502
Band gap at 0K [eV]	0.69	3.50	6.23
c/a ratio	1.618	1.633	1.616
Spontaneous polarization [Cm^{-2}]	-0.042	-0.034	-0.090

Tab. 1: Basic properties of binary nitrides. Lattice parameters are from [34]*, band gap energies from* [35]*, spontaneous polarization values from* [36].

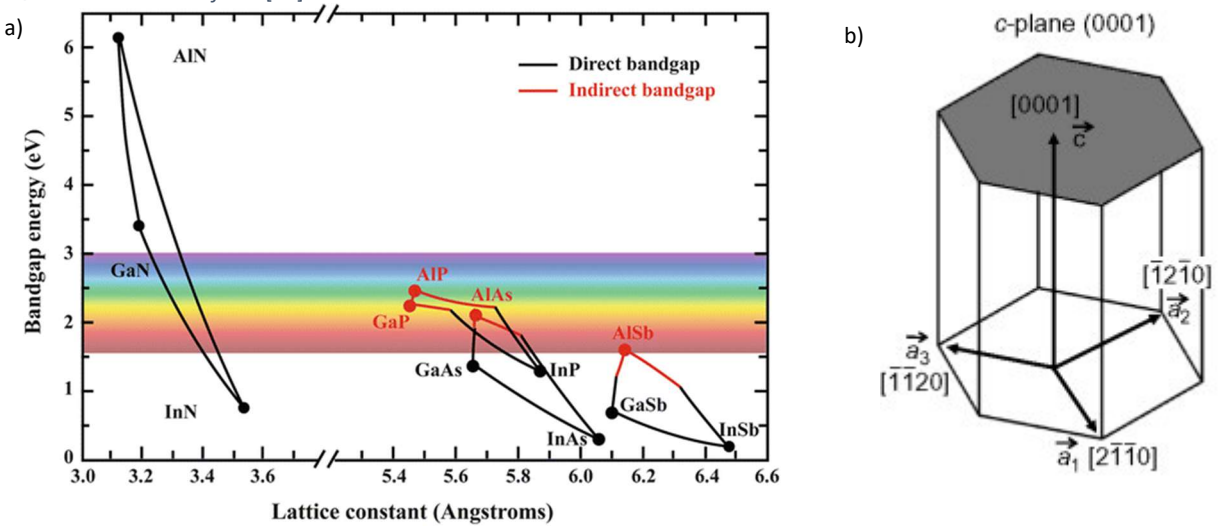

Figure 2: a) Band gap of nitrides dependence on the lattice parameter [35]*, b) GaN elementary cells forming the hexagonal strcuture* [37].

The basic crystallographic parameters of the wurtzite binary nitrides are given in Tab. 1. It is evident that the *c/a* ratio is different for these nitrides. The band gap energy of the alloys can cover spectral range from UV to near-infrared, as can be seen from fig. 1a).

Wurtzite structures are usually represented by 4 Bravais-Miller indexes (*h, k, i, l*), but 3 indexes notation is also used. The index *i* is superfluous and it must satisfy $i = -(h + k)$. However, 4 indexes notation is useful to recognize the hexagonal symmetry of the planes and directions (fig. 2b)).

Because the wurtzite structure lacks the centre of symmetry, spontaneous polarization is present in nitride crystals. Direction of polarization is parallel to *c* axis (direction (0001)). Values, which were obtained by first-principle calculations, are given in Tab 1. Interface between different nitrides like GaN and AlN means discontinuity of spontaneous polarization resulting in generation of internal polarization field. Beside it, a piezoelectric field must be taken into account on the interfaces of different nitrides. These polarization fields alternate the band structure of a material. More detailed discussion can be found in the next section 1.3.

Many properties of ternary alloys like InGaN, AlGaN or InAlN, are not linear functions of the relative concentrations of the III group elements. They can be approximated by quadric relationships known as quadratic Vegard's law (although the dependence for InAlN is even more complicated [36]). A material property $P(x)$ in ternary alloy $A_xB_{1-x}N$ can be therefore expressed by

$$P(x) = x \times P_A + (1 - x) \times P_B + b \times x \times (1 - x) \quad (1)$$

The physical reasons for this non-linear dependence lie in the bond length alternation, volume deformation (different *c/a* ratio for different binary nitrides) or a disorder of the alloy [36]. The quadratic term is specified by the bowing parameter *b*.

1.3 InGaN/GaN heterostructures: basic properties

InGaN/GaN heterostructures are a unique physical system, especially from the luminescence mechanism point of view. One of the surprising characteristics is high luminescence efficiency also in the high dislocation-density regime, although dislocation are thought to behave as non-radiative centers [6]. In conventional materials used for LED fabrication like GaP or GaAs, dislocation density is required to be in order 10^5 or 10^6 cm^{-2} to obtain 50 % internal efficiency. However, InGaN/GaN based LEDs can work with the same efficiency with dislocation density more than 2 or 3 orders of magnitude higher. One of the possible explanation can be connected with V-pits, as discussed in section 1.7 [38]. Another widely-excepted explanation involves local potential minima occurring in InGaN layer caused by random alloy fluctuations (or quantum well width fluctuations in the case of QW structure) [39].

These potential minima might localize carriers before they can non-radiatively recombine on dislocations [40]. However, there are still observations hardly explainable by this theory.

One of them is connected with very long lateral diffusion length of carriers reaching up to tens of micrometres [41] which is far beyond the average dislocation distances in the high dislocation density regime. The long diffusion length of carriers is confirmed also by problems connected with lateral downsizing of the InGaN/GaN material for microLEDs fabrication [14]. Second question arises from the time-resolved photoluminescence. Presence of local potential minima should results in non-monoexponential decay curves with shape similar to donor-acceptor (DAP) recombination, as proposed in [42]. However, the decays are often found to be of different character. A different model suggesting presence of both bound exciton and free (uncorrelated) carriers was found to fit large variety of experimental data well [43]. This would suggest that high efficiency of luminescence found in the samples without the carriers localized on lateral potential minima have different origin.

As was mentioned briefly in the previous section 1.2, the interface between different nitrides like GaN and InGaN results in presence of piezoelectric and spontaneous polarization field. The field modifies the band edges of the heterostructure. In conventional Ga-face InGaN/GaN quantum well structure, it leads to a spatial separation of electrons and holes which should lead to lower radiative efficiency and longer decay times compared to polarization-free structures.

Spontaneous polarization for InGaN/GaN heterostructure with in content x can be obtained using [36]

$$P^{SP}(x) = -0.042x - 0.034(1-x) + 0.037x \times (1-x). \tag{2}$$

The piezoelectric field is calculated from the Hook's law [36]:

$$\sigma_i = C_{ij}\varepsilon_j, \qquad i,j = 1,2,\ldots 6, \tag{3}$$

where we use Voigt notation and σ_i are components of stress tensor, ε_j are components of deformation tensor and C_{ij} are components of the elastic tensor. Elastic tensor for wurtzite crystal has the form

$$C = \begin{pmatrix} C_{11} & C_{12} & C_{13} & 0 & 0 & 0 \\ C_{12} & C_{11} & C_{13} & 0 & 0 & 0 \\ C_{13} & C_{13} & C_{33} & 0 & 0 & 0 \\ 0 & 0 & 0 & C_{44} & 0 & 0 \\ 0 & 0 & 0 & 0 & C_{44} & 0 \\ 0 & 0 & 0 & 0 & 0 & \frac{1}{2}(C_{11} - C_{12}) \end{pmatrix}, \tag{4}$$

For a conventional InGaN/GaN growth in [0001] direction without shear stresses, the only relevant non-zero components are $\varepsilon_1 = \varepsilon_2 = \varepsilon_0 = \frac{a_{\mathrm{GaN}} - a_{\mathrm{InGaN}}}{a_{\mathrm{InGaN}}}$ and $\sigma_1 = \sigma_2$. Considering this, the σ_1 has the form

$$\sigma_1 = \varepsilon_1 (C_{11} + C_{22} - \frac{2C_{13}}{C_{33}}), \tag{5}$$

And finally, the only non-zero component of piezoelectric polarization can be expressed as

$$P_3^{PZ} = d_{31}(\sigma_1 + \sigma_1) = 2d_{31}\varepsilon_1 (C_{11} + C_{22} - \frac{2C_{13}}{C_{33}}), \tag{6}$$

where d_{31} is a piezoelectric constant. After numerical evaluation, the eq. (6) has the form

$$P_3^{PZ}(x) = 0.148x - 0.0424x(1-x) \quad (\text{in Cm}^{-2}). \tag{7}$$

The total polarization is then given as the sum of the piezoelectric and spontaneous polarizations

$$P(x) = P^{SP}(x) + P^{PZ}(x). \tag{8}$$

The sheet carrier density σ at the InGaN/GaN interface is given as a difference between the total polarization of GaN and InGaN $\sigma = P(0) - P(x)$. Electric field in the growth direction can be finally obtained by integrating this sheet charge density from all interfaces presented in the structure as

$$E(r) = \frac{1}{4\pi\varepsilon} \iint \frac{\sigma(r')dA}{(r'-r)^2}, \tag{9}$$

where ε is the permittivity.

However, electric fields of different origin are always present in the InGaN/GaN structure, too. These include electric field generated by ionized donors and/or acceptors or surface potential of a semiconductor. In the simulation of the band structure all these charges generating electric field must be considered in the integration of eq. (9) [44].

1.4 InGaN/GaN heterostructures as scintillators

Historically, first application of materials as scintillators ($CaWO_4$ and ZnS) is connected with discovery of X-ray radiation [45] at the end of 19$^{\text{th}}$century. Since then, many other scintillator applications with different demands have emerged. In general, requirements for scintillator include [45]:

1. high light yield (LY)
2. stopping power for given type of radiation
3. scintillation response - decay time τ_d and rise time τ_r
4. spectral matching between the scintillator emission spectrum and photo-detector

5. chemical stability and radiation resistance
6. linearity of light response with the incident particle or photon energy – energy resolution

InGaN/GaN scintillators have potential to match all these criterions:

1. InGaN/GaN heterostructures have been reported to possess ultimately high internal quantum efficiency over 80 % [46]. Theoretical maximal LY is inversely proportional to bandgap of a material, which also favors InGaN/GaN over conventional scintillators with larger bandgaps.
2. (In)GaN material is dense material with density of 6.15 g/cm^3.
3. Wannier excitons in GaN have binding energy around 25 meV [47] and excitons in InGaN quantum wells (QWs) should have binding energy even higher which should ensure existence of excitons with fast decay times at room temperature.
4. InGaN/GaN emission energy can be tuned in theory from near UV to near infrared spectral region [35].
5. Nitrides are stable even in highly-corrosive environments [48]
6. If excitonic radiative process is the dominant one, linearity should be ensured.

However, specific requirements are needed in the case of individual applications and one universal material for scintillator can be hardly obtained. InGaN/GaN heterostructures are suitable for only several applications, example of which will be discussed below. Main limitation of these structures is the thickness of active region with InGaN QWs which is up to few micrometers at best while the penetration depth of for example 511 keV photon is about 210 µm (if we assume that the photon loses its energy through Compton scattering). This limitation is discussed in our previous work [49].

A large demand for scintillator with fast rise and decay times emerged for example in field of positron emission tomography (PET) where time-of-flight (TOF) detectors with sufficient time resolution are necessary for higher real-space precision. Nowadays, conventional scintillators based on ionic crystals doped with either transition metals or rare-earth elements are still in use. For TOF-PET applications, the state-of-art scintillators used are LYSO:Ce crystals with LY around 40 000 photons/MeV and decay time 40 ns which limits the best time resolution given as $CTR \approx \sqrt{\frac{\tau_r \tau_d}{LY}}$ to 72 ps. However, application nowadays demand time resolution better than 10 ps [50]. InGaN/GaN heterostructures are promising candidates to reach this limit. Due to the limited thickness of InGaN/GaN heterostructure, a special sandwich structures are usually considered for this application. The sandwich consists of bulk scintillator with high LY which provides energy resolution while the fast scintillator (InGaN/GaN) serves as the time tagger [51,52].

Aside from high-energy photon detection, large demand for high-energy particle detection is important for several applications. In the case of low-penetration depth of such particles which would

hand over all their energy in the active region, InGaN/GaN scintillators might benefit from the high internal radiative efficiency and fast decay time.

1.5 Point defects in GaN and InGaN

Point defects are usually referred as 0D defects meaning that their size is comparable or smaller than the lattice parameter in all dimensions. Depending on their origin, they can be divided into extrinsic and intrinsic point defects. Presence of intrinsic defects (vacancies, interstitials or antisite defects) are unavoidable since the material is grown at non-zero temperature.

From the scintillator perspective, point defects can act as radiative or non-radiative centres or as a electron or hole trap. Usually the point defects are considered to be detrimental for scintillator performance: non-radiative defects degrade the maximal LY, traps will deteriorate the luminescence decay times of all radiative channels and radiative defects have commonly very long decay times. Moreover, defects can affect diffusion length of excited by carriers and absorption of luminescence can be also significant [53]. Recently, attention is paid to so-called defect-assisted Auger recombination mechanism which might be the main non-radiative process in moderate excitation intensity regime [54]. Therefore, understanding the defect formation and their luminescence characteristics are fundamental for successful fabrication of a scintillator.

Probability of defect formation can be presumed by computing formation energy diagrams. These diagrams rely on a density functional theory (DFT) calculations. The basic concept is to calculate formation energy E_f. For example, for a defect on a Ga site the formation energy is calculated as [55]:

$$E_f = E_{tot}^{d} - E_{tot}^{GaN} + \mu_{Ga} - \mu_{def} + q(E_F + E_V) + \Delta^q, \quad (10)$$

where E_{tot}^{d} is the total energy of supercell containing the defect in charge state q, E_{tot}^{GaN} is the total energy of the supercell without defect, μ_{Ga} and μ_{def} are chemical potentials of Ga and defect species, E_F the Fermi level position with respect to valence band maximum E_V and term Δ^q represents the finite cell correction. For defects on nitrogen site, interstitials or vacancies, the equation (10) has to be reformulated accordingly.

A short review of the most common point defects presented in GaN and InGaN is given below.

1.5.1 Carbon on N site C_N

Carbon is one of the most frequently observed contaminants in (In,Al)GaN crystals. Its presence during the growth by Metal Organic Vapor Phase Epitaxy (MOVPE), technique widely used in industry, is unavoidable since C-rich precursor gases like trimethylgallium or triethylgallium are dominant precursor for cations [56,57]. Carbon incorporates preferentially on nitrogen site at low carbon

concentration when the Fermi level is in the upper part of the bandgap, where it acts as deep acceptor (Fig. 3a). This is can be confirmed by Raman spectroscopy or Fourier-Transform infrared (FTIR) spectroscopy [58]. When the Fermi level is pinned to the lower part of the bandgap, carbon will incorporate as a donor. According to the first principle calculations, it should be presented as carbon on Ga site (C_{Ga}) acting as resonant donor. However, no experiment so far has confirmed its presence in this form. On the opposite, FTIR measurements indicate that carbon will form tri-carbon complexes C_N-C_{Ga}-C_N [59] at high carbon concentrations, although theoretical calculations predict very high formation energies for this complex (Fig. 3c).

High-quality unintentionally doped MOVPE-grown GaN samples are usually n-type conductive [60]. Carbon is one of the most widely used acceptor for n-type conductivity compensation which is needed for example in HEMT structures. However, due to the amphoteric behavior of carbon described in the paragraph above, the resistivity of GaN:C layers is limited [61].

A luminescence behavior of carbon in GaN is quite well understood nowadays. Although early papers suggested C_N to be a shallow acceptor with luminescence band around 3.25 eV and ionization energy 230 meV [62], further experiments and theoretical calculation revealed that C_N acts as deep acceptor with transition level (0/-) and ionization energy 0.9 eV giving rise to (in)famous yellow band (YB) with maximum at 2.2 eV in GaN [63–67]. It behaves as very efficient luminescence centrum with hole capture coefficient $C_p = 4 \times 10^{-7}\ \mathrm{cm}^3 s^{-1}$[68]. However, C_N forms also a second transition level (+/0) which is observed in luminescence spectra as blue band (BB_C) with maximum at 2.85 eV [69]. To observe this band in PL spectra, C_N defect has to capture two holes, meaning it can be observed mostly at high excitation intensities and in resistive samples when the time decay of luminescence is slow due to the low electron concentration.

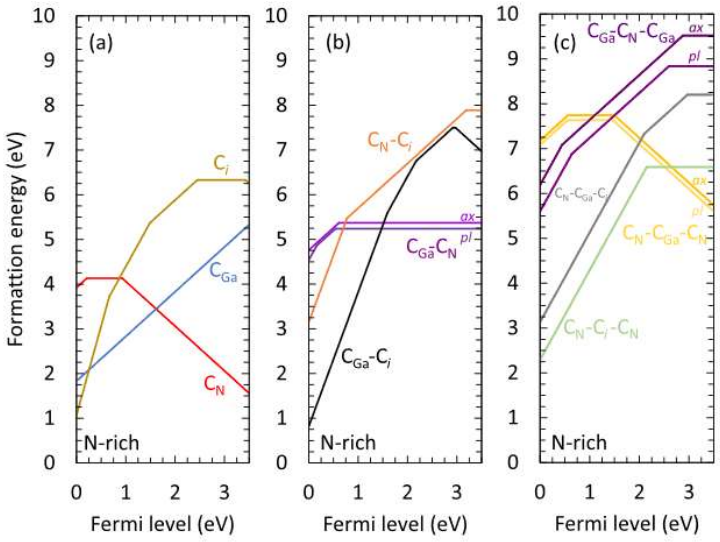

Figure 3: a), b), c): Formation energies of C-related defects from [55].

It should be emphasized that while C_N is very common defect in MOVPE grown GaN, the role of carbon in InGaN layers is not well documented. Carbon concentration in InGaN layers is usually much lower than in the GaN counterparts since MOVPE growth of InGaN layers require very large V/III ratio leading to highly N-rich conditions which decrease the C_N formation probability. Carbon concentration was found to depend on reactor pressure and was suggested to act as nonradiative centrum in InGaN layers [70].

1.5.2 Zinc on Ga site Zn_{Ga}

GaN doped with Zn is known for its high resistivity since 1970s [71]. Zn sits preferentially on the Ga site where it acts as quite deep acceptor with the ionization energy between 300 and 400 meV [72]. Similar to C_N, Zn_{Ga} is a very efficient luminescence centrum in GaN with a hole capture coefficient $C_p = 5 \times 10^{-7}\ \mathrm{cm}^3 s^{-1}$ [68]. The only transition level (0/-) is responsible for a blue emission at 2.9 eV with well resolved zero phonon line (ZPL) at 3.09 eV at low temperatures [72]. However, older reports suggest more levels in GaN bandgap caused by Zn doping. These were manifested by broad PL bands at 2.6, 2.2 and 1.8 eV and attributed to Zn_N defect formed when the samples were heavily Zn-doped [73]. Zn_{Ga} is also one of the few documented acceptors which give rise to a exciton-bound-on-acceptor peak in GaN luminescence spectra which helps to unambiguously identify the defect by PL spectroscopy [73].

Unlike carbon on nitrogen site, zinc on gallium site is readily incorporated into InGaN layers when present during the growth in the chamber. The emission wavelength of Zn band (BB1) depends on InGaN bandgap [8]. Zn doping was studied as a potential way for white LEDs in 1990s and at the beginning of the new millennium, as described in the section 1.1.

1.5.3 Ga vacancies V_{Ga} and their complexes

The presence, concentration and properties of Ga vacancies in GaN are still a research topic with no definitive conclusions. From the intrinsic (native) defects, only Ga and N vacancies might have small enough formation energies to be found in GaN in detectable concentration according to the first principle calculations [53,74]. However, V_{Ga} concentrations found in GaN samples are much larger than predicted by theory, typically in order of $10^{17} - 10^{18}$ cm^{-3} in bulk GaN grown by a Hydride Vapor Phase Epitaxy (HVPE) or ammonothermal methods [75–77].

Ga vacancy should form four transition levels in GaN bandgap, from (-3/-2) to (0/1) states. In the n-type GaN, the ground state should be −3, acting as a compensation centrum. However, from the first principle calculations, V_{Ga} concentration is negligible and Ga vacancies can be found much more likely in complexes. Formation energies of the most relevant complexes for typical MOVPE growth of GaN are depicted in Fig. 4a,b [78].

Ga vacancies are mostly studied by positron annihilation spectroscopy (PAS), as described in Experimental section 2.4. Since PAS measurements are sensitive to defects with open volume, complexes of vacancies with two or three hydrogen atoms can be hardly detected with this technique since the volume is filled with the additional atoms. On the other hand, vacancies complexed with oxygen on nitrogen site have very similar positron lifetime as bare Ga vacancy making it hard to distinguish between them although Doppler broadening spectroscopy might help to overcome this problem [79]. Also, FTIR spectroscopy can be used to identify vacancy complexes with hydrogen. However, this possibility is limited to bulk crystals only [80].

Since there are uncertainties even in the presence and form of Ga vacancies in GaN, their optical or electrical behavior is still matter of debate. In the past, Ga vacancies or their complexes with oxygen were reported to be responsible for YB [77,81,82]. Recent calculations suggest that Ga vacancies should act as a non-radiative centrum in GaN and in InGaN [78].

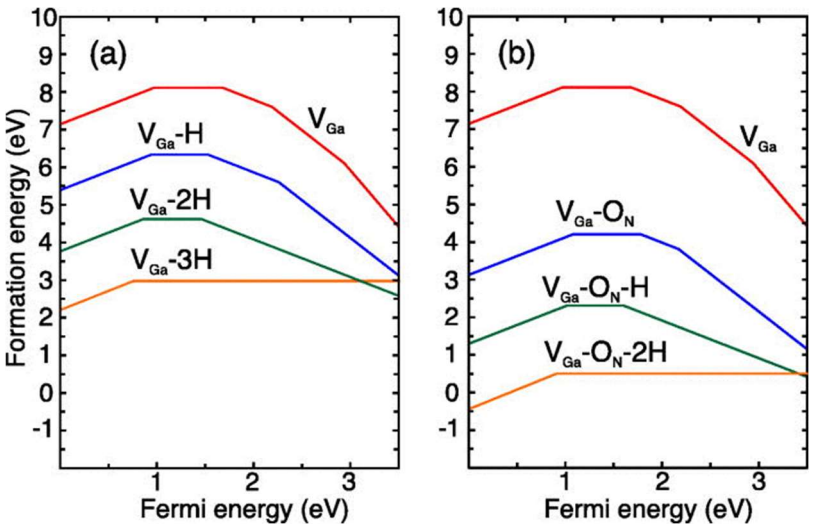

Figure 4: Formation energies of Ga vacancy and its complex with a) hydrogen, b) oxygen and hydrogen according to [78].

1.6 Dislocations in GaN

Non-radiative centers in GaN and InGaN are not restricted to point defects. The luminescence efficiency can be influenced also by presence of 1D defects like dislocation or 2D defects like stacking-faults. Stacking faults are typical defects present in wurtzite GaN layers grown in non- or semi-polar direction or in zinc-blende structure GaN [83–86].

For wurtzite GaN grown in [0001] direction on foreign substrate, for example sapphire, the most abundant defects include dislocations. Lattice mismatch between the sapphire substrate and GaN results in misfit dislocation formation at the interface. Misfit dislocation can also form on InGaN/GaN interfaces to release the strain [87]. However, the problems with the device performance are linked mainly to the threading dislocations [88]. Threading dislocation can be described as edge (or a type) with Burges vector $\frac{1}{3}\langle 11\bar{2}0\rangle$, screw dislocation (or c type) with Burges vector $\frac{1}{3}[0001]$ or mixed (a+c type) with Burges vector $\frac{1}{3}\langle 11\bar{2}3\rangle$ [88].

Threading dislocations' formation mechanism at the sapphire-GaN interface is not clear yet. One of the theories suggest that threading dislocation come from different tilt or twist of initial GaN islands grown during the nucleation phase of the growth relative to the sapphire substrate and their subsequent coalescence [89,90]. However, transmission electron microscopy (TEM) study [91] challenged this theory and suggested that coalescence of two Frank's faults is the main source of threading dislocations in GaN on sapphire. Most probably, the dominant source of the threading dislocation is growth-conditions dependent [88].

It should be noted that there is still no consensus about the dislocation density determination. Since it is an important characteristic of the sample, a method for dislocation density determination should be

non-destructive (this eliminates etching method). TEM technique will provide accurate dislocation density, but only on statistically very limited ensemble, plus the sample is destroyed, too. The most common technique is X-ray diffraction (XRD). According to classical models (sometimes referred as models of misoriented blocks), the dislocation density can be obtained from peak FWHM of suitable rocking curve [92–94]. Because of discrepancies of this simple models with dislocation density obtained from TEM for GaN on a sapphire substrate, a more advanced models based of peak FWHM were additionally developed [95]. However, further studies showed that the FWHM is not sufficient parameter to determine the dislocation density. The main problem lies in the spatial correlation of the dislocations and the fact, that tilt and twist of misoriented blocks are not suitable description of GaN crystal structure grown on sapphire. Models which account for the above mentioned discrepancies are under development [96–98].

In semiconductors, dislocations are usually considered to act as non-radiative centers [88]. However, the GaN-based LEDs have high efficiency despite the high dislocation density compared to other semiconductors like GaP or GaAs. Therefore, the question whether dislocations in GaN act as non-radiative centers was studied. Several groups concluded that dislocation indeed behave non-radiatively [99,100]. The method which is usually adopted in similar studies involve cathodoluminescence (CL) mapping accompanied by an electron beam-based imaging technique.

However, the non-radiative center theory can be justly challenged since according to results in [101,102], dislocations are charged in GaN. Therefore, CL mapping just provides contrast due to charge repelling from dislocation cores instead of non-radiative recombination. The question about dislocation acting as non-radiative center remains quite open, especially if we take into account excitonic recombination mechanism which should not be affected by dislocation charge [88].

1.7 Role of V-pits in GaN and InGaN/GaN structures

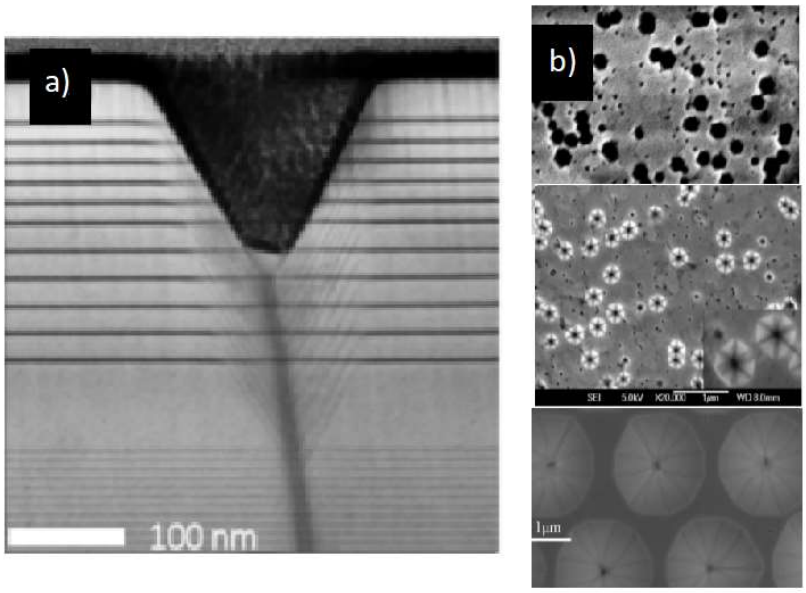

Figure 5: a) TEM image of V-pit in InGaN/GaN structure [103]*, b) SEM images of different orientation of V-pit sidewalls: top {11-22}* [104]*, middle {10-11}, bottom combination of {11-22} and {10-11}* [105].

Performance of scintillator is also affected by light extraction which is influenced by a surface morphology. Growth of InGaN/GaN region is usually performed under conditions which are far from optimal *c* oriented GaN growth. The main requirement for In incorporation into the structure is the low growth temperature of InGaN QW and GaN barrier. Therefore, structural defects are commonly observed. Very extended studies were performed on defect called V-pits since their first observations [106,107]. Typical observation on TEM of surface V-pit is shown in fig. 5a. It was established that V-pits are formed on a threading dislocations with screw component [106,108]. The sidewalls of the V-pits are formed by {10-11} planes [106,109], although planes {11-22} can be achieved [104]. Sometimes V-pits are formed by 12 sidewalls combining these two groups of planes [105]. All these possibilities are shown in fig. 5b) as scanning electron microscopy (SEM) images.

Theoretical model explaining origin of V pits was introduced in [110]. It is based on Franks' model [111] for balancing elastic strain energy of dislocation with free surface energy. However, Franks' model predicts opening of V-pits but does not predict its enlarging with further layer growth which is contradictory to the observations (for example fig. 6a)). The problem is validity of Franks' model which is limited for equilibrium processes, while MOVPE growth is only locally equilibristic process [110]. This means that the system can be described by the same macroscopic entropy function with the same variables, but their local values are in thermodynamical equilibrium only for limited mass element of a medium. According to this theory, V-pit opening is caused by inability to keep the same local equilibrium for edge and spiral centre of a dislocation line. The local equilibrium and consequently the

V-pit size is affected by elastic energy of dislocation, free surface energy and kinetic processes which can be influenced by the growth conditions.

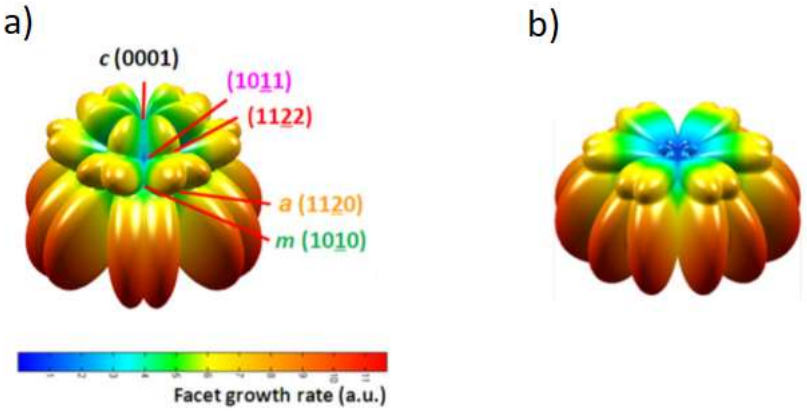

Figure 6: relative growth rates for a) low V/III condition and b) high V/III condition [112].

The growth rate on semipolar planes {10-11} and {11-22} is reduced in comparison to (0001) [112]. The fig. 6 shows the relative growth rates in the form of kinetic Wullfs plot, from which a crystal shape can be derived. The growth rates are obtained experimentally by growing GaN crystals on patterned GaN templates with different orientations [112]. For growth of active InGaN/GaN region, high V/III ratio is typical (Wullf plot in fig. 6b)). It is clearly seen that from nonpolar or semipolar planes, the {11-22} and {10-11} have the largest growth rates. Hence, their formation is the most probable when the deviation from c-plane occurs.

Consequence of the lower growth rate on V-pit sidewalls are thinner InGaN QWs on the facets. It means that energy levels in these InGaN QWs are shifted to higher energies. Therefore, these QWs act as potential barriers for the carriers and separate the carriers from dislocation core [38]. This feature helps to increase InGaN/GaN efficiency as the dislocation are considered to act as non-radiative centres [113] (but the consensus is not achieved, see discussion in section 1.6).

The attempts to find the ideal V pit size were made. Our group suggested optimal diameter of V-pits in range 200 – 300 nm [49]. Exceeding this diameter results in lowering PL efficiency because large ratio of surface is covered by V-pits and therefore small portion of flat surface (where the PL dominantly comes from) is left.

The ideal V-pit diameter around 200 – 250 nm was found in [103]. However, their explanation was different: when growing more InGaN QWs (and consequently enlarging the V-pit), the growth rate on semipolar planes increases while the In incorporation gets worse. On that account, the potential barrier formed by V pit QWs decreases and blocking carriers from dislocation core is worse when increasing V-pit size.

In electroluminescence measurements, V-pits can serve as efficient carrier transport paths, which can be beneficial in LEDs with higher number of QWs [114,115].

2 Experimental

2.1 MOVPE reactor and QWs growth

A term “epitaxy” was first used in 1928 by French mineralogist Louis Royer [116] and it comes from Greek epi (meaning above) and taxis (meaning an ordered manner). It is one of the methods for crystal growth with well-defined orientation. MOVPE is a type of epitaxy growth technique history of which is dated back to the 1960s [117]. Nowadays, it is one of the most wide-spread technique for semiconductor material growth both in science and industry [117].

During the MOVPE growth, precursors are transported to the reactor chamber where they are (usually thermally) dissociated to simpler molecules which are adsorbed on the sample surface. Next, the required atoms are released from these molecules and they can either diffuse on the surface, desorb or be incorporated into the crystal lattice of the material [118]. A schema of the MOVPE process is shown in Fig. 7.

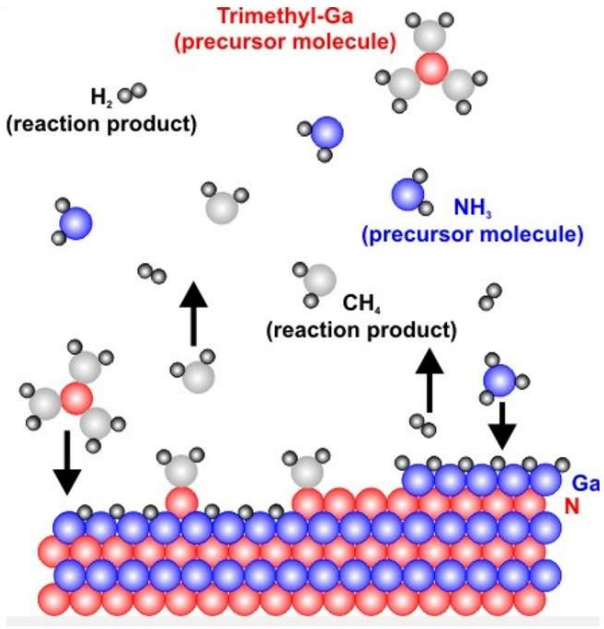

Figure 7: Schema of the MOVPE process. From [119].

Aside from the growth conditions like temperature, pressure, precursor type and flow etc., critical parameter for MOVPE growth is a difference between substrate lattice parameter alongside with its thermal expansion coefficient and the grown layer. Since there is still lack of commercially available bulk GaN substrates which could be used for homoepitaxy, heteroepitaxy usually takes place. Table 2.2 shows the most common substrates used for GaN growth.

Property	Sapphire	SiC	Si	GaN
Lattice mismatch vs GaN	-16%	3.5%	-17%	None
Thermal mismatch vs GaN	-25%	33%	116%	None
Cost [euro/cm^2] (year 2012)	1	10	0.1	100

Tab. 2: Properties of common substrates for epitaxial GaN growth [120].

Nowadays, structures grown on SiC and sapphire substrates possess comparable quality. The large lattice mismatch in the case of sapphire is solved by so-called buffer layer. This technique is based on low temperature (480°C – 600°C) buffer layer followed by high-temperature annealing. After this procedure, the high-quality GaN epilayer can be grown [121]. Still, the dislocation density in the GaN layers on sapphire without any additional improvements usually stays in order 10^9 cm^{-2}.

The InGaN layers growth requires significantly lower temperatures than GaN layers and higher In precursor flow rates than source of Ga because of the higher vapour pressure of indium compared to gallium [122]. For the scintillator application, a high number of InGaN QWs is needed so the active area is as "thick" as possible since the penetration depth of high-energy radiation can be in order of hundreds of micrometres or even millimetres. For example, penetration depth of 511 keV gamma radiation is 12 mm in conventional LYSO scintillator [123]. In the case of InGaN/GaN, "thick" means thickness in order of micrometres because of the growth limitations.

On the other hand, the p-type doped material is not necessary contrary to LEDs, so difficult task of p-type doping is irrelevant for this application.

All the samples referred in this work were grown on the Aixtron 3 × 2 CCS MOVPE system equipped with LayTec EpiCurveTT apparatus for in situ measurement of reflectivity, curvature and true wafer temperature. Sapphire substrates with *c*-plane orientation were used for most growths, only a few samples were grown on thick GaN substrates, GaN templates on sapphire substrates, patterned substrates or sapphire substrates with different orientations. If the substrate is different from *c*-plane sapphire, it will be clear from the text. Buffer layers were grown with trimethylgallium (TMGa) and ammonia (NH_3) precursors with a hydrogen carrier gas. The active region precursors were NH_3, triethylgallium and trimethylindium as sources for N, Ga and In respectively.

First, the low-temperature GaN layer was grown at 550 °C followed by 3 µm-thick GaN epilayers. Before the growth of active region, a GaN layer doped with silicon was added (target doping 10^{18} cm^{-3}). Growth parameters of the InGaN QWs differ among the samples and they are mentioned in the text, if necessary. Generally, typical InGaN QW thickness is below 2 nm and In content is between 5 – 10 %. After each stack of five QWs and QBs, 25 nm-thick GaN separation layer with the same growth temperature as for QB was grown. The whole structure was capped with a GaN layer to prevent the

active region being affected by the surface states. Thicknesses of cap layers among the samples are different, too.

2.2 Photoluminescence measurements

Samples were characterized by two standard PL emission spectra measurements. The first setup consists of 375 nm laser with spot 0.5 mm in diameter and maximal excitation density 10 Wcm^{-2} (resonant excitation of QWs and defect states below GaN bandgap), SDL-1 double-grating monochromator and GaAs photomultiplier tube for measurements in the visible region. The setup uses a Lock-in detection with chopping at frequency of 35 Hz. The measurement step was 1 nm for most of the measurements. The samples were excited from the active region side (front side) under the angle 30° from surface normal and the luminescence was collected from the front side by elliptic mirror.

Energy resolution δE is given by monochromator slits widths d_s with an approximate relationship $\delta E = 1.6 \cdot 10^{-6} d_s$, which means resolution 1.6 nm at slits widths 1 mm. Typical slits width range for measurements was 0.05 – 2.5 mm. The slit was set independently for each measurement to get maximal signal. As a consequence, at low emission intensities, the energy resolution gets worse and some luminescence features may disappear (like Fabry-Perot oscillations). Measured spectra were multiplied by λ^2 to obtain intensity dependence on energy rather than wavelength [124]. Wavelength 375 nm (= 3.3 eV) can excite only InGaN QWs and defect states in GaN bandgap as the energy is below the GaN bandgap. It enables to excite the whole active region even at high number of QWs because of the low absorption on QWs.

The second PL setup uses confocal microscope LabRAM HR Evolution, He-Cd laser (wavelength 325 nm) with maximal used excitation density 0.5 Wcm^{-2}, objective 74CG, spot diameter 2 μm and CCD detector Synapse with UV enhanced sensitivity. Both excitation and emission light were passed through objective and reflected laser light was filtered by in-build edge filter. Wavelength 325 nm (= 3.8 eV) enables excitation over GaN bandgap and the characteristic penetration depth is about 100 nm [125]. The maximal achievable resolution of the system is < 1 cm^{-1} at wavelength 837 nm.

Time resolved spectra were collected with 339 nm pulse laser diode excitation, single-grating monochromator and GaAs photomultiplier. Time resolution is dependent on time range used, the best obtainable resolution is around 300 ps. For the decay time of interest, time resolution was around 9 ns. Time resolved emission spectra were obtained by measuring time decays at a given wavelength range with 5 nm step. Next, integration of intensity was performed in given time windows and the average time value was selected as a representation of the time window.

2.3 Cathodoluminescence measurements

Sample characterization by means of electron microscopy were performed in Philips XL30 ESEM with home-build cathodoluminescence setup including Avaspec ULS-TEC spectrometer with resolution about 10 nm. Spectrometer was cooled down to 5°C to increase signal/noise ratio. Monochromatic images were obtained with usage of one-grating monochromator and photomultiplier Hamamtsu H7711-13. Spatial resolution of CL images was limited by spot size necessary to obtain sufficient luminescence signal. Monochromator slits were set on maximum values giving resolution around 10 nm. The electron current in SEM is tuneable in range 1 pA – 1 µA and acceleration voltages in range 0.2 – 30 keV.

2.4 Positron annihilation spectroscopy (PAS)

Positron annihilation lifetime spectroscopy is based on the measurement of temporal difference between the creation of positron and its annihilation in the material with (valence) electrons. The annihilation is detected through the 511 keV photon which is created during the annihilation event [126]. The lifetime of the positron is increased in the case that positron is trapped in open volume in the material. These include surface, dislocations or vacancies.

Metal Organic Vapour Phase Epitaxy (MOVPE) grown samples are only few µm thick which means that conventional ^{22}Na source cannot be used due to the high penetration depth of the positrons with maximum in order of hundreds on µm. The penetration depth can be approximated by [127]

$$z = \frac{A}{\rho} E^b \tag{11}$$

where A = 4 µg/cm^2, ρ = 6.15 g/cm^3, and b = 1.6 for GaN.

To overcome this problem, different source of positrons is needed. The synchrotron or linear accelerator with pulsed beam can be used. The generated positrons can be moderated and accelerated to the required energy (and therefore, penetration depth) = variable energy positron annihilation spectroscopy (VEPAS).

Positron source for the presented measurements was linear accelerator in ELBE facility [128] at Helmholtz-Zentrum Dresden-Rossendor. To moderate the positrons, tungsten plate was used. The FWHM of the resolution function was 230 ps and the energy was varied between 0.5 and 12 keV.

3 Results and Discussion

3.1 Motivation

Purpose of the research presented in this thesis is to understand the role of various defects affecting the performance of the scintillator. The most important effect of point defects from the scintillator perspective is the introduction of luminescence centres with long decay time and/or non-radiative centres which decrease the efficiency of the scintillator.

First of all, the GaN buffer layer beneath the active InGaN/GaN region must be optimized since highly energetic radiation penetrates through the whole structure. For example, according to paper [129], the deposited energy of 40 keV X-ray radiation in InGaN/GaN active region 1.8 µm thick (a thickness limit achieved by our group) was only about 3.6 % of the incoming beam (paper gives value 2.3 % but it does not account for different light yield of InGaN/GaN scintillator and LYSO etalon). Therefore, most of the incoming energy of such radiation is deposited in the GaN buffer layer and substrate. Any luminescence channels with slow components presented there would therefore deteriorate the scintillation response of the whole structure. The main "slow" luminescence channel in this case is YB originating from C_N defect, as described in the section 1.5.1. Paper 1 deals with this topic.

Next, optimization of InGaN/GaN active region is needed. We found out that the most abundant impurity in our InGaN layers is Zn (described in section 1.3.2) which produces broad luminescence band with slow decay time. The most important characteristics of this band can be found in paper 2 and paper 3.

Beside the impurities present in the scintillator structures, Ga vacancies and their complexes with hydrogen were studied. Paper 4 describes role of vacancies in GaN grown at different growth conditions and provides unique insight to physical processes affecting the vacancy formation and behaviour. Paper 5 presents a search for a dominant non-radiative centrum in InGaN layers which is known to be captured in the first few InGaN monolayers grown atop GaN buffer layer.

Lastly, the paper 6 describes a problem of growing thick InGaN/GaN active region. The main topic is effect of surface defects (V-pits) and their influence on In incorporation in their vicinity. Understanding the V pit behaviour is a fundamental necessity for spatial homogeneity on both nano- and micro-scale as well as the scintillation response in the sense of spectral peak positions and luminescence decays.

3.2 Introduction to models used in paper 1 and paper 3

Recombination mechanism involving deep acceptors like C_N or Zn_{Ga} in GaN can be either donor-acceptor pair (DAP) or electron-acceptor (e-A) recombination. Since we have used both types of recombination to model measured dependencies obtained in papers 1 and 3, a short introduction is provided here. Please note that in papers 1 and 3 there was not enough space to describe the model in detail. Moreover, a plotting error has occurred in paper 1 giving a wrong form of rate equation. The correct form is present at the end of this section.

Theoretical model for time dependence of DAP recombination was introduced in 1965 [130]. Assuming that hole function localized at acceptor site has spatial variation (r being the distance from an acceptor):

$$\psi_h(r) \sim r^m \exp(-\frac{r}{a}), \tag{12}$$

the probability of recombination $W(r)$ is in the form

$$W(r) = W_{max} \exp\left(-\frac{2r}{R_d}\right), \tag{13}$$

where W_{max} is the maximal probability of recombination of infinitesimally close DAP, a is a constant describing hole wave function exponential decrease and R_d is the Bohr radius of a donor [130].

We can assume that probability of recombination is inversely proportional to recombination time τ_{DAP}

$$W(r) = \frac{1}{\tau_{DAP}}. \tag{14}$$

To obtain mean value for a large distribution of DAPs, DAP distribution $G(r)$ is needed. In paper 1, distribution of donors and acceptors in relatively thick 1 µm layer is studied. Moreover, the growth was performed at high temperature. Therefore, it was assumed, that DAP distribution is the uniform one $G(r) = \frac{1}{c-d}$, where c and d are the boundaries of the interval from which the R values can be taken. We choose the interval as $r \in \left[0, 2 \cdot \frac{1}{\frac{4\pi N_D^0}{3}}\right]$, N_D^0 being the concentration of neutral donors.

Under this assumption, the average distance between donor and acceptor is $\langle r \rangle = \int_a^b G(r) r \cdot dr = \left(\frac{3}{4\pi N_D^0}\right)^{\frac{1}{3}}$, which gives us

$$\frac{1}{\langle \tau_{DAP} \rangle} = \langle W(R) \rangle = W_{max} \cdot e^{-\frac{2}{a_D}\left(\frac{3}{4\pi N_D^0}\right)^{\frac{1}{3}}} \tag{15}$$

Paper 1 shows the dependence of the mean decay time on doping concentration. However, decay curves can be also analysed. Instead of complicated calculations in [130] which are valid only at certain experimental conditions, more simplistic approach is advised here. Intensity dependence of isolated DAP can be described as:

$$I_r(t) = A \cdot \exp\left(\frac{-t}{\tau_{DAP}(r)}\right) = W(r)\exp\left(\frac{-t}{\tau_{DAP}(r)}\right) \tag{16}$$

However, we have to deal with distribution of acceptors and donors situated in InGaN quantum wells (in paper 3). In this case, the depth distribution of donors and acceptors was obtained by secondary ion mass spectroscopy (SIMS). Next, to obtain lateral distribution, simulation was performed in which acceptors were placed into the InGaN layers and with a given probability distribution, donors were situated. Subsequently, shortest distances of DAPs were calculated and these were used in the recombination probability calculation.

Unfortunately, SIMS measurements are not available for all studied samples. Therefore, comparison of DAP distribution obtained by different methods was performed. Theoretical distribution of DAPs was calculated in [131] for the limiting cases when concentration of donors and acceptors are almost equal or the concentration of the impurities is high that their distribution is considered completely chaotic or the case when one of the species is greatly abundant. The expression obtained for the first case is [131,132]

$$G(r) = C_1 4\pi r^2 N_A \exp(-\tfrac{4}{3}\pi r^3 N_A), \tag{17}$$

N_A being the concentration of acceptors and C_1 a normalization constant. The expression can be easily modified to the 2D case when the dopants are inside of QW whose lateral dimensions are much larger than the perpendicular one. The distribution than looks like

$$G(r) = C_2 2\pi r N_A \exp(-\pi r^2 N_A^{\frac{2}{3}}), \tag{18}$$

C_2being again a normalization constant. In the second case, the distribution depends on growth temperate T_G and permittivity ε of the material which limits the interaction of ionized atoms during the growth through Coulomb interaction [131,132]

$$G(r) = C_3 r^2 \exp(\tfrac{e^2}{kT_G \varepsilon r})\exp(-\tfrac{4}{3}\pi r^3 N_A), \tag{19}$$

where C_3 is a normalization constant. Please be advised that paper [131] provides equations 17)-19) without normalization constants, leaving the $G(r)$ non-dimensionless. Comparison of these four

distributions are shown in Fig. 8 with parameters used for sample P3 in paper 3. Concentration N_A was used as an average of SIMS-measured concentration Zn for the 5 bottom QWs. It shows that 3D uncorrelated distribution approximates the SIMS-based distribution very well.

With a DAP distance distribution, time dependent energy shift of DAP recombination can be derived. The shift happens because the closer the pair are, the higher probability of recombination they have (and therefore, a shorter lifetime) and at the same time, their recombination energy is higher because of the Coulombic term depending on their distance. Intensity measured from the whole ensemble of DAPs can be described as

$$I(t) = \sum_r I_r(t) \cdot G(r) \tag{20}$$

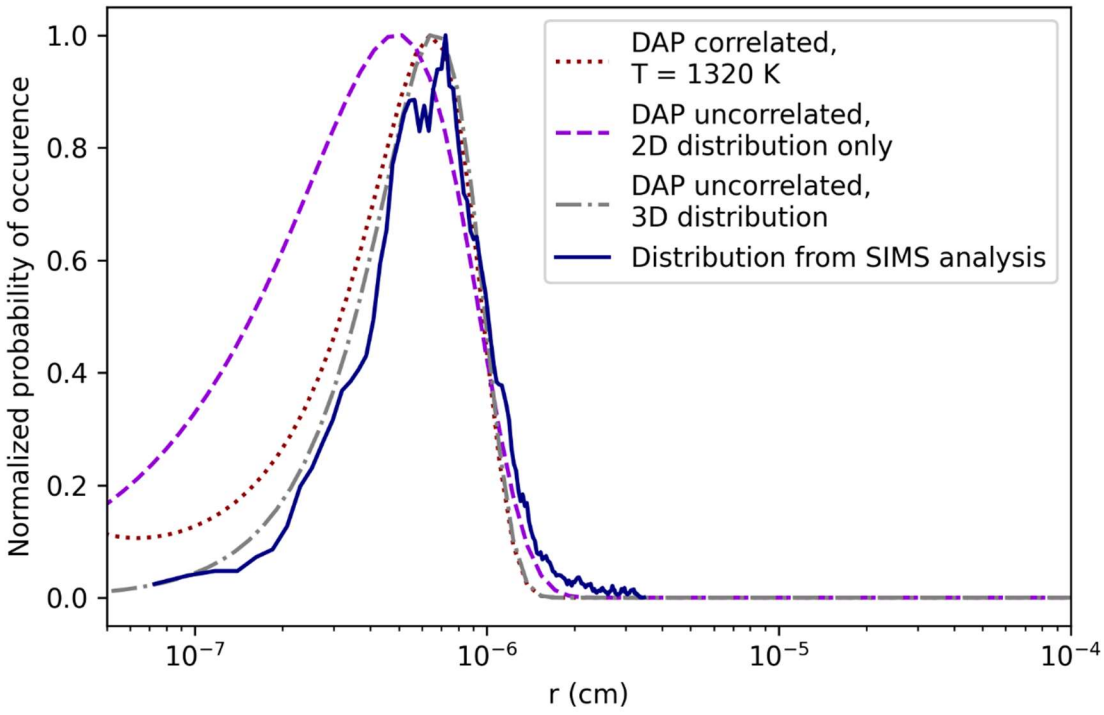

Figure 8 : Distribution of DAP distances for sample P3 from paper 3. Uncorrelated 3D distribution mimics the SIMS distribution very well.

The Coulombic term is approximated as

$$E_R = k_e \frac{e^2}{\varepsilon r}, \tag{21}$$

where *e* is the elementary charge and ε is the static permittivity of the material (ε_r = 10 was assumed for GaN [133]) and k_e is the Coulomb constant. To obtain the mean energy shift of the whole DAP system at given time *t*, one has to sum the energies weighted by the respective intensities $I_r(t)$

$$E(t) = \frac{\sum_r E_r \cdot I_r(t) \cdot G(r)}{\sum_r I_r(t) \cdot G(r)} \tag{22}$$

This approach was used in paper 3 to analyse the shifts and the decay curves (eq. 22 and 20, respectively).

Paper 1 uses relation from for e-A recombination model which is based on rate equations describing the recombination process. Please note that due to the plotting error of the journal, the rate equations (3) in paper 1 are not easily understandable. The correct form should be

$$\frac{dn}{dt} = -B \cdot n \cdot p - C_{nD} n \cdot (N_D - N_D^0) - C_{nA} n \cdot N_A^0 - C_{nS} n \cdot \left(N_S - N_S^0\right) \tag{23}$$

$$\frac{dN_D^0}{dt} = C_{nD} n \cdot (N_D - N_D^0) - C_{DA} \cdot \left(N_D^0 \cdot N_A^0\right)$$

$$\frac{dN_A^0}{dt} = C_{pA} p \cdot \left(N_A - N_A^0\right) - C_{DA} \cdot \left(N_D^0 \cdot N_A^0\right) - C_{nA} n \cdot N_A^0$$

$$\frac{dN_S^0}{dt} = C_{nS} n \cdot \left(N_s - N_S^0\right) - C_{pS} p \cdot N_S^0,$$

where $n = n_0 + \Delta n$ is the electron concentration consisting of the equilibrium concentration n_0 and concentration of excited electrons Δn. $p = \Delta p$ is the hole concentration which is equal to the nonequilibrium one in the n-type widegap semiconductor at room temperature. N_D, N_A, and N_s are concentrations of donors, acceptors, and non-radiative traps, respectively, and superscript 0 indicate their charge-neutral state. Coefficients C_{nD}, C_{nS} describe a process when the electron is captured by donor and non-radiative center, respectively. Similarly, C_{pA} and C_{pS} are coefficients of hole capture by acceptor and non-radiative center. Finally, C_{DA} is the coefficient of radiative donor-acceptor pair recombination and C_{nA} describes radiative recombination by e-A transition.

3.3 Paper 1 Summary

Paper 1 focuses on the acceleration of YB luminescence decay using a doping of GaN layers by the n-type dopants, Si and Ge. SIMS analysis is used to precisely determine the dopant concentration and Hall alongside with C-V measurements are performed to obtain the free-electron concentrations and mobilities in the GaN layers. Paper 1 shows, that YB can be caused either by DAP or e-A recombination mechanisms, both of them are influenced by Si and Ge doping. A suitable model is suggested for both types of recombination mechanism and tested against experimental data. An excellent agreement between our results and previously determined coefficients of maximum DAP recombination rate W_{max} and electron capture coefficient C_{nA}, respectively, are obtained. The mean decay time is shortened from the ms range in the case of undoped sample to hundred-of-ns range in the case of dopant concentration is in 10^{19} cm^{-3} order.

The most important result is that although we can hardly eliminate YB from the spectra because of omnipresent carbon impurity during MOVPE growth, we can accelerate its decay time to the range where it is not harmful for most of the intended application.

However, several issues remain unresolved. First of all, high doping concentration leads to surface morphology deterioration which prohibits subsequent high-quality InGaN/GaN active region growth. Next, the paper 1 presents thermally stimulated luminescence (TSL) measurements which reveal several traps (of unknown origin). However, their signal is too weak to perform any deeper analysis. Nevertheless, these traps must be eliminated in the future since they can provide carriers for a luminescence centrum with expected time delay in a range of milliseconds. Unfortunately, TSL signal increases with doping concentration.

In addition, the surface roughness was investigated by electron microscopy and white light interferometry techniques. These revealed increasing roughness with higher dopant concentration, more pronounced in the case of Si doping. Since the GaN buffer layer will be overgrown in the intended application by InGaN/GaN active region, the surface should be kept as smooth as possible. This makes Ge doping more favourable than Si one.

It should be noted that paper 1 describes behaviour of GaN grown at high-temperature (1052°C). In this high-temperature regime, it is easy to achieve high electron densities by Si doping but practically impossible to achieve it by Ge doping. Only recently [134], we found out that Ge incorporation is highly temperature dependent and growth at lower temperature (< 900°C) might enhance Ge incorporation by orders of magnitude. This might pave a way for future studies of highly conductive GaN buffer layers

used beneath the scintillator active region. Since Ge atom incorporated on Ga site should produce much smaller stress than Si on the same site because of similarity of Ga and Ge atomic radii, Ge doping in high concentration should not deteriorate the surface morphology as Si doping does.

3.4 Paper 2 Summary

Paper 2 studies the Zn depth distribution in the InGaN/GaN QWs structure which is grown as two stacks, each containing 5 QWs. Zinc is unintentionally present impurity and it was never introduced into the growth apparatus on purpose. The depth profiles obtained by SIMS show that Zn is preferentially incorporated into InGaN layers. The reason for this is discussed in paper 5. Moreover, the highest concentration of Zn is always found in the bottom QW of the particular stack and decreasing in the next 4 QWs. Paper 2 suggests that the trend can be explained by difference of Zn formation energies among the QWs which are caused by band structure modification by Si doping alongside with the internal polarization fields.

The paper was published in 2021 when the source of Zn was unknown. The model for Zn incorporation proposed in paper 2 suggested that Zn comes from a precursor used for GaN barrier layer growth (or from carrier gas) and TEGa precursor was tentatively nominated as the most probable Zn contaminated source. However, future investigations revealed that the main Zn contaminant has probably different origin: neoprene gloves used for sample manipulation in glovebox. Inspection of the gloves in SEM revealed that their surface is porous (Fig. 9 left) and that particles with typical diameter 20 – 50 µm and characteristic composition (Fig. 9 right) are released from the gloves. Therefore, before the whole growth process starts, Zn-containing particles are most probably present on the susceptor surface.

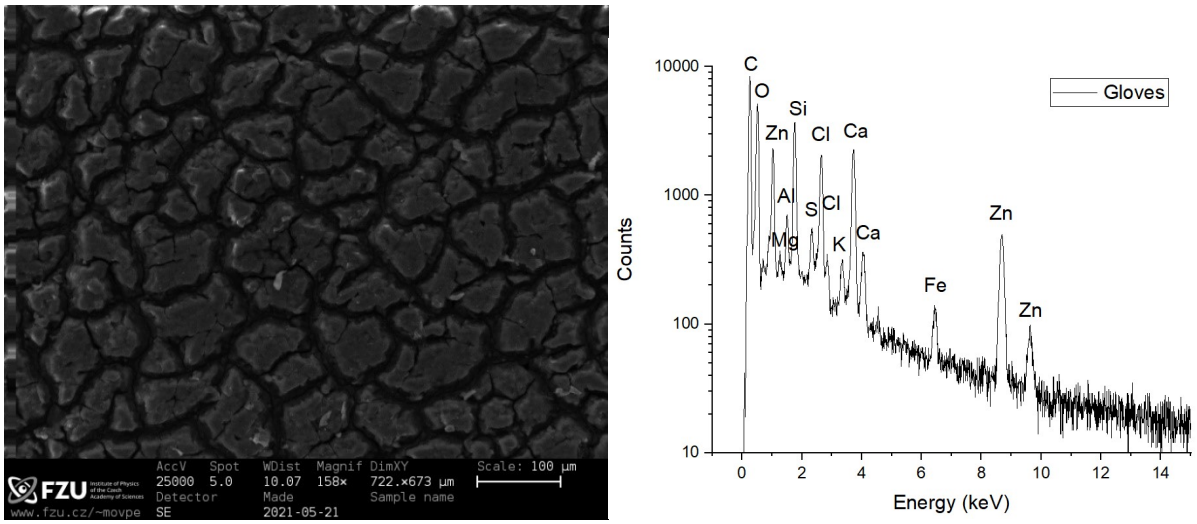

Figure 9: left - surface morphology of the gloves, right - characteristic EDX spectrum of the glove particle.

The change of the gloves for zinc-free (hypalone) ones decreased the Zn-related band in the PL spectra drastically, suggesting lowering the Zn concentration in the samples.

The model for Zn incorporation from paper 2 suggested that the Zn containing precursor must be present also during the separation layer between the two stacks of 5 QWs. This result is consistent with the new finding concerning the Zn origin: the Zn-containing particles on susceptor will decompose

during the pre-growth high-temperature annealing (1060°C) and given the low value of Zn boiling temperature (907°C at atmospheric pressure), zinc will evaporate and subsequently condensate on showerhead, which is water-cooled. During the growth, precursors flowing through the showerhead can probably react with Zn and deliver it to the GaN surface, where it serves as surfactant and only when the InGaN growth is launched, Zn will incorporate to the structure. The incorporation is not mediated by the low growth temperature of InGaN only, as was confirmed also in paper 4.

Unfortunately, soon after the Zn source was found and gloves changed, the growth apparatus was put out of operation due to a building reconstruction so several questions remain unanswered. For example, it is possible that the gloves are significant Zn contaminators, but maybe, these are not the only ones. This would be supported by the fact that while samples doped with Si grown after the gloves change still show small Zn-related PL band, similar sample doped with Ge did not (black line Fig. 10).

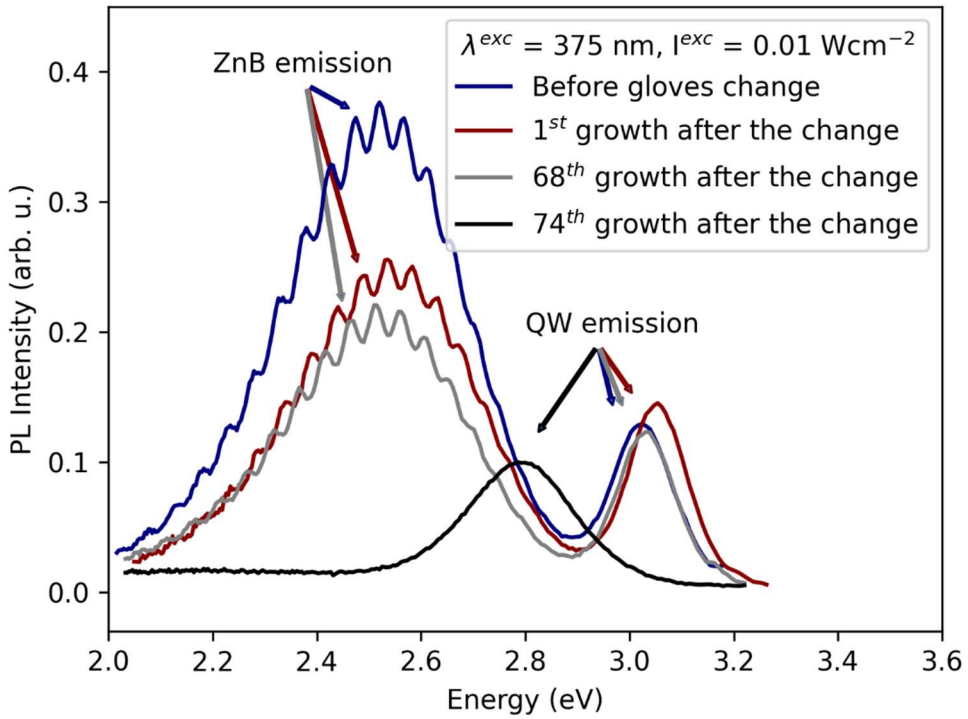

Figure 10: Comparison of PL spectra of samples grown before and after the gloves change. All samples are doped by Si except the 74th growth after the change (black line) which is doped by Ge.

3.5 Paper 3 Summary

In paper 3, large spectral shifts of Zn-related luminescence band (ZnB), which are observed in time-resolved and excitation intensity-dependent spectra, are investigated and modelled. It is suggested that the recombination mechanism can be viewed as DAP mechanism between Si donors and Zn acceptors in InGaN QWs. The explanation is provided using model introduced in the beginning of the section 3.2. The reason for the shift is stronger Coulombic interaction between DAPs when more DAPs are excited – situation oncoming either at the higher excitation intensity or shorter time after the pulse.

It is also suggested that the binding energy for electrons at donors sites increases dramatically due to the quantum confinement in InGaN QWs. This enables observation of DAP recombination even at room temperature.

The spectral shift of ZnB is important from the scintillator perspective: at low excitation intensity, the energy separation between QW recombination peak and ZnB is around 400 meV (sample dependent). Therefore, one can suggest that in the scintillator design, a suitable choice of PMT spectrally sensitive only in spectral region of QW recombination peak can be used to eliminate the slow luminescence of ZnB from the time characteristics of the scintillator. However, as described in paper 3, shortly after the excitation pulse the ZnB is shifted towards higher energies by magnitude sufficient to efficiently overlap ZnB with QW emission, making the suggested solution unfeasible. Please note that the suggested solution can be hardly used also in the case of elimination of YB – in the sandwiched scintillators (mentioned in section 1.4), the PMT must be sensitive for both scintillators used. Unfortunately, the YB emission overlaps with emission of many scintillators like YAG:Ce or GaGG:Ce. The spectral sensitivity limitation would eliminate these scintillators as potential candidates for energy-resolution-ensuring scintillator.

Similarly to the discussion in the case of paper 2, the putting growth apparatus out of operation prevented us from further experiments involving the ZnB shift. One of them would be doping InGaN QWs by Ge which should lead to more pronounced shifting of ZnB. However, there is a question whether Ge doping would not deteriorate the decay characteristics of the QW emission since introduction of a new energy level might lead to releasing and re-trapping carriers which would elongate the decay times.

3.6 Paper 4 Summary

In paper 4, the GaN layers grown at different growth conditions are studied by SIMS, VEPAS, PL and other techniques. The research is unique due to the VEPAS measurements performed on MOVPE grown samples which were not studied before due to the thickness limitation of the GaN layers and high penetration of conventionally generated positrons, as mentioned in section 2.4. Ga vacancy concentration in 10^{16} cm^{-3} range was found in all samples except those prepared at highest temperature of 1100°C. In these samples, the dominant open-volume defects were established to be complexes $2V_{Ga}$-$2V_N$.

An unexpected anticorrelation between V_{Ga} concentration an PL intensity of GaN near-band-edge luminescence was found. It was explained as a competition of V_{Ga} defects and an unknown defect, which acts as more efficient non-radiative centrum than bare V_{Ga}. No correlation between V_{Ga} concentration and defect luminescence was found (for as-grown samples).

Trends of Ga vacancy concentration on growth conditions are rather complicated. One of the messages of the paper 4 is that first-principle calculation used to predict vacancy formation in GaN provide results which are far from experimental findings. In theory, the V_{Ga} concentration should be increasing exponentially with temperature. Our findings show that the V_{Ga} concentration increase only for samples prepared from TMGa precursor, while for TEGa precursor the concentration is decreasing (in N_2 atmosphere) or is constant (H_2 atmosphere). There are also great differences in the V_{Ga} concentrations between the samples grown from TEGa and TMGa precursor at otherwise identical growth conditions. Therefore, V_{Ga} creation cannot be viewed as a thermodynamically driven process, but reaction kinetics should be considered in future theoretical investigations. For samples grown from TMGa, an anticorrelation between Ga vacancy and carbon concentration is observed.

The limitation of the research provided in paper 4 is that V_{Ga} concentration from VEPAS data was calculated for bare Ga monovacancies in 2- charge state. Future work should be focused on temperature dependent PAS measurements to reveal the true charge state of vacancies. Moreover, one of the drawbacks of VEPAS technique is inability to detect vacancies which are complexed with hydrogen atoms. Samples annealed in different atmospheres should be therefore studied to prove or disprove existence of such complexes. Preliminary results of electron beam annealing suggest that the hydrogen-related complexes play a major role in luminescence properties of the samples (not published yet). Please note that the observed anticorrelation between GaN near-band-edge luminescence intensity and the Ga vacancy concentration can be (at least partly) caused by presence of hydrogen which decorates the vacancies forming this way a very efficient non-radiative centrum

and that actual Ga vacancy concentration as well as luminescence intensity will be affected by hydrogen removal through annealing.

From the scintillator perspective, the important result is that YB intensity is not correlated with the Ga vacancy concentration. Therefore, in the scintillator design, more attention must be paid to suppress the carbon concentration. SIMS measurements on the studied samples suggest that lowest carbon concentration can be achieved by growth from TEGa precursor at moderately high temperature (~900°C) or by growth from TMGa precursor at very high temperature (~1100°C). However, for practical purposes the latter case can be performed in H_2 atmosphere only because of the surface deterioration in N_2 atmosphere. Moreover, the very high temperature cannot be applied for GaN barrier layer growth due to the InGaN QW layer decomposition [135]. Therefore, the GaN layers grown from TEGa at ~900°C seems promising as GaN buffer and barrier layers for scintillators. Temperature around ~900°C should be also suitable for Ge incorporation [134] if we want to apply doping advantage studied in paper 1.

3.7 Paper 5 Summary

As mentioned in paper 4, Ga vacancy complexes with hydrogen cannot be detected by VEPAS due to the small open volume of such complexes. In paper 5, we suggest that SIMS analysis of hydrogen can provide a way to overcome this problem.

The motivation for paper 5 was an observation of macroscopic luminescence intensity inhomogeneity of samples prepared by Aixtron 3 × 2 CCS MOVPE reactor. The second motivation was to explain a function of so-called InGaN underlayer (UL), a technique commonly adopted in InGaN/GaN LED growth. The InGaN UL is used because of the well-known problem of high non-radiative recombination rate in the bottom InGaN quantum wells (which are of course very similar to those present in our scintillator structures) [136]. However, there are still controversies about the exact mechanism which enhances the luminescence efficiency when the UL is used.

SIMS analysis revealed that places with lower luminescence intensity contain higher concentration of hydrogen and that depth profile of Zn and hydrogen impurities are anticorrelated. Zn was incorporated in the bottom QWs and hydrogen was found in QWs atop of them. Based on large palette of results presented in paper 5, it was suggested that the problem of high non-radiative recombination is as follows: Ga (and/or In) vacancies are formed or captured in InGaN layers to relieve high tensile strain. Zn will occupy the empty Ga (or In) sites – although Zn has similar atomic radius as Ga in metallic form (134 and 135 pm, respectively [137]), the acceptor nature of Zn_{Ga} in GaN results in shrinkage of its effective atomic radius as one electron is missing, similar to other doped semiconductors [138], leading to strain reduction in the InGaN layer. When the Zn concentration on the growing surface is in not high enough to fill the empty Ga sites, complexes of Ga vacancies and hydrogen are formed (V_{Ga}-3H has much smaller formation energy than the Ga monovacancy as mentioned in the section 1.5.3). These complexes are responsible for non-radiative recombination in the QWs. Since Zn is impurity which is not common to all nitride growth apparatuses across the world, in its absence the V_{Ga}-3H complexes will be formed in the bottom QWs eventually, causing the above mentioned high non-radiative recombination rate.

The fundamental reason for spatial macroscopic inhomogeneity of hydrogen (and therefore vacancy) distribution is not clear yet but is connected to construction of showerhead reactor and the gas flow during the growth.

For scintillators, the paper 5 brings rather unfortunate information: bottom QWs will contain either V_{Ga}-3H acting as non-radiative centres or Zn_{Ga} acting like radiative centres with long decay times unless the vacancy formation in these InGaN layers is suppressed.

3.8 Paper 6 Summary

V-pits greatly affect the scintillator performance. Paper 6 explores the influence of V-pits on subsequent InGaN QWs growth by means of TEM, SEM, SIMS and PL measurements. It is found that In and Ga atoms adsorbed on V-pit sidewalls are not fully incorporated on these (semi-polar) walls but migrate towards nearest *c*-oriented plane where they form region with higher thickness. This results in large redshift of the QW luminescence due less pronounced quantum confined effect. Quite surprisingly, In atom concentration in top QWs is decreasing with increasing the number of QWs, as observed by SIMS. This behavior is common for samples grown on both sapphire and GaN substrates used in this work. Since the dislocation density (and therefore, V-pit density) for sample grown on GaN substrate is at least two orders of magnitude lower than in the sapphire substrate case, the lower In concentration cannot be directly connected to V-pits.

For a scintillator, V-pits have multiple roles. First of all, they lower the volume of scintillator and therefore, its stopping power. On the other hand, V-pits effectively shield carriers from dislocations. As mentioned in our previous research, an optimum size of V-pit was found to be around 200 nm [49].

Moreover, in application which require light extraction in the *c* direction, V-pits might be beneficial because they disturb the wave-guide effect, otherwise present because of the high refractive index difference between GaN and air. It should be emphasized that the waveguide effect is actually disturbed also by the GaN-sapphire interface where the nucleation layer with low quality is grown.

Paper 6 together with paper [49] presents the importance of V-pit size control by growth parameters. As mentioned in discussion of paper 4, optimal conditions from perspective of point defects can be found. However, to control the V-size, growth at different parameters like higher temperature will be probably required. Therefore, the compromise between crystal and surface quality must be sought. One of the solution for the future will be probably growth of quantum wells and barriers at optimal conditions from point-defect perspective while the growth of thicker separation layers between the quintet of QWs and barriers will be grown at conditions used to control V-pit size.

4 Conclusion and outlook

In order to develop a new, fast scintillator based on InGaN/GaN quantum heterostructure, point- and extended defects and their influence on luminescence properties were studied and optimization of the particular layers in the structure was suggested.

Beneath the InGaN/GaN active region, a GaN buffer layer is always present when a growth on foreign substrate like sapphire takes place. In the intended application, the buffer layer is excited by the highly energetic radiation, thus affecting the overall scintillator performance. Therefore, in the first step, the defect (carbon related) yellow luminescence band coming from the buffer layer was investigated. It was shown in paper 1, that the time decay of yellow band can be accelerated from the order of milliseconds up to order of hundreds of nanoseconds with increasing the Si or Ge dopants concentration. A model for both DAP and e-A recombination was applied to fit the experimental results. It was shown that above Mott transition, e-A recombination mechanism dominates but DAP recombination mechanism takes place below this transition. Moreover, the value of electron capture coefficient 1.8×10^{-13} cm^3s^{-1} and $W_{max} = 3 \times 10^6$ s^{-1} coefficient (determining the maximal recombination rate of a given luminescence centrum) obtained from the models are in perfect agreement with previously reported values. Thermally stimulated luminescence measurements revealed presence of several charge carrier traps. Unfortunately, the signal was too low to determine the physical properties of the particular traps. In addition, surface roughness increase was observed by SEM images and white light interferometry techniques affecting the light extraction efficiency. However, the Ge doping leads to smoother morphology which predetermines Ge doping as a more suitable dopant for intended the application.

In the active region, the important recombination channel at low excitation intensities is represented by Zn impurity giving rise to highly efficient luminescence band. Paper 2 describes a model which is suggested to reveal the main source of the Zn contamination in the InGaN layers. Model based on different formation energies caused by intentional Si doping and polarization field points to a precursor which is present in the reactor chamber during the GaN barrier growth as the most probable source of Zn impurity (TEGa is tentatively proposed to be contaminated by Zn). However, later analysis reveals that the primary source of Zn are probably glovebox gloves. After the gloves change, the Zn contamination is greatly reduced. However, the model proposed in paper 2 is not in contradiction with this explanation of Zn origin.

Paper 3 is dedicated to large spectral shifts of Zn luminescence band with excitation intensity. Time resolved spectra show different time evolution of spectral shift after the excitation pulse for three samples. Red shifts up to almost 200 meV are observed in time resolved spectra with increasing delay

time after the excitation pulse. Model based on DAP recombination is introduced and experimental data of the decay times and spectral shifts are fitted with the model providing information about donor binding energy, maximal recombination rate coefficient and limit peak position after infinite time decay after the pulse. Donor binding energy is found to increase in InGaN QWs compared to bulk GaN which explains the high efficiency of the DAP recombination at room temperature. The results provided in the paper can be also used to explain the historical failure of InGaN:(Zn, Si) based structures in white light LED application. There, the large spectral shifts of the low-energy component of the spectra with increasing power resulted in colour change of the LED from white to blue.

Native defects in GaN layers are studied in paper 4. Twelve GaN layers grown on sapphire substrate at different growth conditions (different temperature, carrier gas and Ga precursor gas combinations) are examined by VEPAS, SIMS, PL and other techniques. Ga vacancy are found in concentration in order of 10^{16} cm^{-3} in all studied samples except the two grown at the highest temperature. These two samples contain complexes $2V_{Ga}$-$2V_N$. Quite surprisingly, the luminescence intensity of GaN near-band-edge emission is increased with higher Ga vacancy concentration. No correlation between yellow luminescence and vacancy concentration is found. From the VEPAS and luminescence results, GaN layer grown from TEGa precursor at temperature around 900°C can be suggested as the most promising candidate for GaN buffer growth. The experimental results are also important for the future theoretical calculations: the basic thermodynamical calculations are not sufficient to predict vacancy concentration in MOVPE-grown GaN and the kinetics of the growth must be taken into account.

Non-radiative recombination is inspected also in paper 5. Based on the SIMS and luminescence measurements, complexes of Ga (or In) vacancy with hydrogen interstitials are nominated as the most abundant non-radiative centres in the bottom InGaN QWs. These complexes cannot be revealed by VEPAS measurements since presence of hydrogen near the vacancy reduces the open volume of the defect, thus leading to decrease of the lifetime of trapped positron at such site to a value comparable with the lifetime of positron in ideal crystal. From the SIMS analysis it seems probable that incorporation of Zn fills the Ga vacancy, thus the competition between non-radiative V_{Ga}-$3H_i$ complex and Zn_{Ga} radiative defect takes place. The lateral distribution of the hydrogen concentration in the samples grown prepared by the Aixtron 3 × 2 CCS MOVPE reactor is also found to be strongly inhomogeneous. However, the source of the inhomogeneity was not found yet. Moreover, the formation of V_{Ga}-$3H_i$ complexes is also a new mechanism explaining the low efficiency of the bottom InGaN QWs in LED structures and the LED efficiency improvement when the InGaN underlayer in the structure is used.

Paper 6 provides insight into complexity of scintillator development. Based on the papers 1-5, optimized structure can be suggested. However, the optimized growth conditions from point defect perspective lead to deteriorated morphology of samples with high number of InGaN QWs. Paper 6 studies influence of 3D defects called V-pits on In incorporation (and therefore, the luminescence wavelength, time decay etc.). It shows that In adsorbed on V-pit semi-polar planes is not incorporated there to the structure but diffuses to the polar *c*-plane surrounding the V-pits. This causes redshift of the luminescence wavelength from regions in the vicinity of V-pits and larger full width at half maximum of the luminescence peak integrated from a macroscopic area. Comparison of the samples grown on sapphire substrate (high density of V-pits $\sim 10^8$ cm^{-2}) and GaN substrate (2 orders of magnitude lower V pit density) shows also a redshift of the luminescence in the case of samples grown on sapphire which is more pronounced with increasing number of quantum wells. This shift is caused by incorporation of the comparable In amount on a smaller surface area which is reduced by V-pits.

From the presented results, the following outlook can be made: the growth conditions must be chosen as a compromise between the luminescence efficiency perspective and the morphology perspective. The region of InGaN QWs and GaN barriers should be grown under the optimal growth conditions from the luminescence efficiency perspective but the separation layer between certain number of the QW/barrier pairs should be incorporated to control the morphology. Since the growth apparatus has been out of order since February 2021, the optimal growth conditions have not been implemented in one structure, yet. The suggested optimized growth conditions might have the form as in Fig 11. In our long-term experience, the stacks of 5 QW/barrier pairs are beneficial for luminescence intensity.

The GaN buffer layer should be grown from TEGa at relatively high temperature (900°C) in N_2 atmosphere to minimize the carbon contamination (results from paper 4). Moreover, Ge doping can be used to accelerate yellow luminescence from residual carbon defects (results from paper 1). Since the main source of Zn contamination was found and removed, the bottom QWs should not contain Zn_{Ga} defects (results of paper 2 and 3). Hopefully, Ga vacancies are not generated in large amount in GaN buffer layer (results from paper 4 and 5) resulting in lower concentration of V_{Ga}-mH$_i$ complexes in the bottom QWs grown on the top of GaN buffer layer. The GaN barriers should be grown also from TEGa in N_2 atmosphere and optionally doped with Ge which might accelerate the luminescence of (defect) bands if still presented in the luminescence spectra (results from paper 1). GaN separation layer should be designed to control V-pit size. It means the high temperature growth is needed and H_2 atmosphere also reduces the surface roughness (combined results of paper 1 and 6).

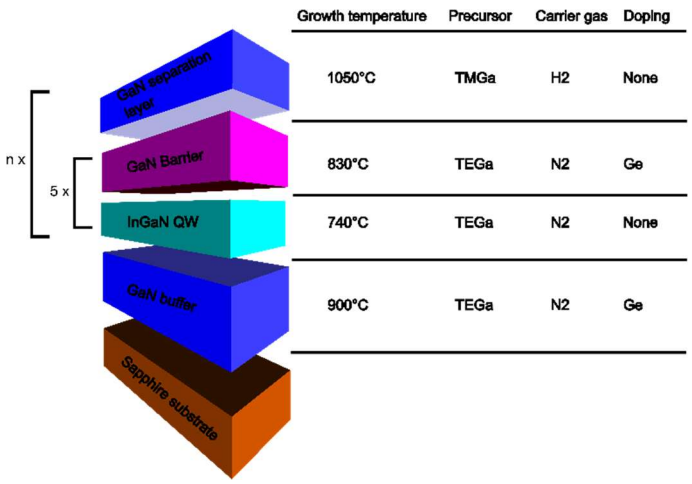

Figure 11: Proposal of the optimized structure growth conditions. n should be at least 10 to achieve sufficiently thick active region.

5 References

[1] J.I. Pankove, Luminescence in GaN, J. Lumin. 7 (1973) 114–126. https://doi.org/10.1016/0022-2313(73)90062-8.

[2] J.I. Pankove, E.A. Miller, J.E. Berkeyheiser, GaN blue light-emitting diodes, J. Lumin. 5 (1972) 84–86. https://doi.org/10.1016/0022-2313(72)90038-5.

[3] J.I. Pankove, J.A. Hutchby, Photoluminescence of ion-implanted GaN, J. Appl. Phys. 47 (1976) 5387. https://doi.org/10.1063/1.322566.

[4] H.P. Maruska, W.C. Rhines, D.A. Stevenson, Preparation of Mg-doped GaN diodes exhibiting violet electroluminescence, Mater. Res. Bull. 7 (1972) 777–781. https://doi.org/10.1016/0025-5408(72)90127-4.

[5] J. Duboz, J. Garcia, GaN or the history of a scientific explosion driven by applications and markets, in: Low-Dimensional Nitride Semicond., 2002.

[6] S. Nakamura, Nobel Lecture: Background story of the invention of efficient blue InGaN light emitting diodes, Rev. Mod. Phys. 87 (2015) 1139. https://doi.org/10.1103/REVMODPHYS.87.1139/FIGURES/17/MEDIUM.

[7] J.K. Sheu, C.J. Pan, G.C. Chi, C.H. Kuo, L.W. Wu, C.H. Chen, S.J. Chang, Y.K. Su, White-light emission from InGaN-GaN multiquantum-well light-emitting diodes with Si and Zn codoped active well layer, IEEE Photonics Technol. Lett. 14 (2002) 450–452. https://doi.org/10.1109/68.992574.

[8] S. Nakamura, High-power InGaN/AlGaN double-heterostructure blue-light-emitting diodes, Tech. Dig. - Int. Electron Devices Meet. (1994) 567–570. https://doi.org/10.1109/IEDM.1994.383328.

[9] Y. Narukawa, I. Niki, K. Izuno, M. Yamada, Y. Murazaki, T. Mukai, Phosphor-conversion white light emitting diode using InGaN near-ultraviolet chip, Japanese J. Appl. Physics, Part 2 Lett. 41 (2002) L371. https://doi.org/10.1143/JJAP.41.L371/XML.

[10] J. Hye Oh, J. Rok Oh, H. Keun Park, Y.-G. Sung, Y. Rag Do, J.Y. Tsao, M.E. Coltrin, M.H. Crawford, J.A. Simmons, J.K. Park, C.H. Kim, S.H. Park, H.D. Park, S.Y. Choi, New paradigm of multi-chip white LEDs: combination of an InGaN blue LED and full down-converted phosphor-converted LEDs, Opt. Express, Vol. 19, Issue S3, Pp. A270-A279. 19 (2011) A270–A279. https://doi.org/10.1364/OE.19.00A270.

[11] B. Damilano, N. Grandjean, C. Pernot, J. Massies, Monolithic white light emitting diodes based on InGaN/GaN multiple-quantum wells, Japanese J. Appl. Physics, Part 2 Lett. 40 (2001) L918. https://doi.org/10.1143/JJAP.40.L918/XML.

[12] M. Yamada, Y. Narukawa, T. Mukai, Phosphor free high-luminous-efficiency white light-emitting diodes composed of InGaN multi-quantum well, Japanese J. Appl. Physics, Part 2 Lett. 41 (2002) L246. https://doi.org/10.1143/JJAP.41.L246/XML.

[13] R.T. Ley, J.M. Smith, M.S. Wong, T. Margalith, S. Nakamura, S.P. Denbaars, M.J. Gordon, Revealing the importance of light extraction efficiency in InGaN/GaN microLEDs via chemical treatment and dielectric passivation, Appl. Phys. Lett. 116 (2020) 251104. https://doi.org/10.1063/5.0011651.

[14] T. Ma, J. Chen, Z. Chen, L. Liang, J. Hu, W. Shen, Z. Li, H. Zeng, Progress in Color Conversion Technology for Micro-LED, Adv. Mater. Technol. (2022) 2200632. https://doi.org/10.1002/ADMT.202200632.

[15] G. Meneghesso, M. Meneghini, E. Zanoni, Breakdown mechanisms in AlGaN/GaN HEMTs: An overview, (2014). https://doi.org/10.7567/JJAP.53.100211.

[16] Z. Bougrioua, I. Moerman, L. Nistor, B. Van Daele, E. Monroy, T. Palacios, F. Calle, M. Leroux, Engineering of-an insulating buffer and use of AlN interlayers: Two optimisations for AlGaN-GaN HEMT-like structures, Phys. Status Solidi Appl. Res. 195 (2003) 93–100. https://doi.org/10.1002/PSSA.200306305.

[17] GaN Semiconductor Devices Market to Touch USD 4.3 Billion by 2025, (n.d.). https://www.everythingrf.com/news/details/5319-GaN-Semiconductor-Devices-Market-to-Touch-USD-4-3-Billion-by-2025 (accessed October 3, 2022).

[18] K. Wang, C. Sheng, Application of GaN in 5G Technology, J. Phys. Conf. Ser. 1699 (2020). https://doi.org/10.1088/1742-6596/1699/1/012004.

[19] S. Nakajima, GaN HEMTs for 5G Base Station Applications, Tech. Dig. - Int. Electron Devices Meet. IEDM. 2018-December (2019) 14.2.1-14.2.4. https://doi.org/10.1109/IEDM.2018.8614588.

[20] Y.Z. Chiou, Y.K. Su, S.J. Chang, J. Gong, Y.C. Lin, S.H. Liu, C.S. Chang, High detectivity InGaN-GaN multiquantum well p-n junction photodiodes, IEEE J. Quantum Electron. 39 (2003) 681–685. https://doi.org/10.1109/JQE.2003.810262.

[21] L. Sang, M. Liao, Y. Koide, M. Sumiya, High-temperature ultraviolet detection based on InGaN Schottky photodiodes, Appl. Phys. Lett. 99 (2011) 031115. https://doi.org/10.1063/1.3615291.

[22] T. Wang, Y.H. Liu, Y.B. Lee, Y. Izumi, J.P. Ao, J. Bai, H.D. Li, S. Sakai, Fabrication of high performance of AlGaN/GaN-based UV light-emitting diodes, J. Cryst. Growth. 235 (2002) 177–182. https://doi.org/10.1016/S0022-0248(01)01918-2.

[23] R. Hovden, Z. Mi, W.J. Shin, A. Pandey, J. Gim, High-efficiency AlGaN/GaN/AlGaN tunnel junction ultraviolet light-emitting diodes, Photonics Res. Vol. 8, Issue 3, Pp. 331-337. 8 (2020) 331–337. https://doi.org/10.1364/PRJ.383652.

[24] S. Cuesta-Arcos, Q.-M. Thai, Y. Curé, F. Donatini, E. Bellet-Amalric, C. Bougerol, G. Nogues, S.T. Purcell, L.S. Dang, E. Monroy, Development of AlGaN/GaN heterostructures for e-beam pumped UV lasers, Https://Doi.Org/10.1117/12.2578370. 11686 (2021) 55–63. https://doi.org/10.1117/12.2578370.

[25] C.J. Neufeld, N.G. Toledo, S.C. Cruz, M. Iza, S.P. DenBaars, U.K. Mishra, High quantum efficiency InGaN/GaN solar cells with 2.95 eV band gap, Appl. Phys. Lett. 93 (2008) 143502. https://doi.org/10.1063/1.2988894.

[26] E. Matioli, C. Neufeld, M. Iza, S.C. Cruz, A.A. Al-Heji, X. Chen, R.M. Farrell, S. Keller, S. DenBaars, U. Mishra, S. Nakamura, J. Speck, C. Weisbuch, High internal and external quantum efficiency InGaN/GaN solar cells, Appl. Phys. Lett. 98 (2011) 021102. https://doi.org/10.1063/1.3540501.

[27] P. Pittet, G.N. Lu, J.M. Galvan, J.M. Bluet, I. Anas, J.Y. Giraud, J. Balosso, PL characterization of GaN scintillator for radioluminescence-based dosimetry, Opt. Mater. (Amst). 31 (2009) 1421–1424. https://doi.org/10.1016/J.OPTMAT.2008.09.012.

[28] A. Hospodková, M. Nikl, O. Pacherová, J. Oswald, P. Brůža, D. Pánek, B. Foltynski, E. Hulicius, A. Beitlerová, M. Heuken, InGaN/GaN multiple quantum well for fast scintillation application: radioluminescence and photoluminescence study, Nanotechnology. 25 (2014) 455501. https://doi.org/10.1088/0957-4484/25/45/455501.

[29] A.G. Melton, E. Burgett, T. Xu, N. Hertel, I.T. Ferguson, Comparison of neutron conversion layers for GaN-based scintillators, Phys. Status Solidi C. 9 (2012) 957–959. https://doi.org/10.1002/PSSC.201100432.

[30] A. Trampert, O. Brandt, K.H. Ploog, Chapter 7 Crystal Structure of Group III Nitrides, Elsevier, 1997. https://doi.org/10.1016/S0080-8784(08)63088-4.

[31] H. Okumura, K. Ohta, K. Ando, W.W. Rühle, T. Nagatomo, S. Yoshida, Bandgap energy of cubic GaN, Solid. State. Electron. 41 (1997) 201–204. https://doi.org/10.1016/S0038-1101(96)00166-9.

[32] B. Daudin, G. Feuillet, J. Hübner, Y. Samson, F. Widmann, A. Philippe, C. Bru-Chevallier, G. Guillot, E. Bustarret, G. Bentoumi, A. Deneuville, How to grow cubic GaN with low hexagonal phase content on (001) SiC by molecular beam epitaxy, J. Appl. Phys. 84 (1998) 2295. https://doi.org/10.1063/1.368296.

[33] B. Sarkar, S. Washiyama, M.H. Breckenridge, A. Klump, J.N. Baker, P. Reddy, J. Tweedie, S. Mita, R. Kirste, D.L. Irving, R. Collazo, Z. Sitar, N- and P- type Doping in Al-rich AlGaN and AlN, ECS Trans. 86 (2018) 25–30. https://doi.org/10.1149/08612.0025ECST/XML.

[34] H. Morkoç, Handbook of Nitride Semiconductors and Devices, Handb. Nitride Semicond. Devices. 1 (2009) 1–1255. https://doi.org/10.1002/9783527628438.

[35] J. Wu, W. Walukiewicz, Band gaps of InN and group III nitride alloys, Superlattices Microstruct. 34 (2003) 63–75. https://doi.org/10.1016/J.SPMI.2004.03.069.

[36] O. Ambacher, J. Majewski, C. Miskys, A. Link, M. Hermann, M. Eickhoff, M. Stutzmann, F. Bernardini, V. Fiorentini, V. Tilak, B. Schaff, L.F. Eastman, Pyroelectric properties ofAl(In)GaN/GaN hetero- and quantum well structures, J. Phys. Condens. Matter. 14 (2002) 3399. https://doi.org/10.1088/0953-8984/14/13/302.

[37] K.M. Kelchner, S.P. DenBaars, J.S. Speck, GaN Laser Diodes on Nonpolar and Semipolar Planes, Semicond. Semimetals. 86 (2012) 149–182. https://doi.org/10.1016/B978-0-12-391066-0.00004-6.

[38] A. Hangleiter, F. Hitzel, C. Netzel, D. Fuhrmann, U. Rossow, G. Ade, P. Hinze, Suppression of nonradiative recombination by V-shaped pits in GaInN/GaN quantum wells produces a large increase in the light emission efficiency, Phys. Rev. Lett. 95 (2005) 127402. https://doi.org/10.1103/PHYSREVLETT.95.127402/FIGURES/4/MEDIUM.

[39] N.K. Van Der Laak, R.A. Oliver, M.J. Kappers, C.J. Humphreys, Role of gross well-width fluctuations in bright, green-emitting single InGaN/GaN quantum well structures, Appl. Phys. Lett. 90 (2007) 121911. https://doi.org/10.1063/1.2715166.

[40] S. Chichibu, T. Azuhata, T. Sota, S. Nakamura, Spontaneous emission of localized excitons in InGaN single and multiquantum well structures, Appl. Phys. Lett. 69 (1998) 4188. https://doi.org/10.1063/1.116981.

[41] A. David, Long-Range Carrier Diffusion in (In,Ga)N Quantum Wells and Implications from Fundamentals to Devices, Phys. Rev. Appl. 10 (2021) 54015. https://doi.org/10.1103/PhysRevApplied.15.054015.

[42] A. Morel, P. Lefebvre, T. Taliercio, T. Bretagnon, B. Gil, N. Grandjean, B. Damilano, J. Massies, Two-dimensional “pseudo-donor–acceptor-pairs” model of recombination dynamics in InGaN/GaN quantum wells, Phys. E Low-Dimensional Syst. Nanostructures. 17 (2003) 64–67. https://doi.org/10.1016/S1386-9477(02)00762-2.

[43] Y. Xing, L. Wang, D. Yang, Z. Wang, Z. Hao, C. Sun, B. Xiong, Y. Luo, Y. Han, J. Wang, H. Li, A novel model on time-resolved photoluminescence measurements of polar InGaN/GaN multi-quantum-well structures, Sci. Reports 2017 71. 7 (2017) 1–9. https://doi.org/10.1038/srep45082.

[44] P. (Paul) Harrison, A. Valavanis, Quantum wells, wires and dots : theoretical and computational physics of semiconductor nanostructures, (n.d.).

[45] M. Nikl, Measurement Science and Technology Scintillation detectors for x-rays Scintillation detectors for x-rays, Meas. Sci. Technol. 17 (2006) 37–54. https://doi.org/10.1088/0957-0233/17/4/R01.

[46] I.E. Titkov, D.A. Sannikov, Y.M. Park, J.K. Son, Blue light emitting diode internal and injection efficiency, AIP Adv. 2 (2012) 032117. https://doi.org/10.1063/1.4739409.

[47] A.K. Viswanath, J.I. Lee, D. Kim, C.R. Lee, J.Y. Leem, Exciton-phonon interactions, exciton binding energy, and their importance in the realization of room-temperature semiconductor lasers based on GaN, Phys. Rev. B. 58 (1998) 16333. https://doi.org/10.1103/PhysRevB.58.16333.

[48] V. Sudarsan, Materials for Hostile Chemical Environments, in: Mater. Under Extrem. Cond. Recent Trends Futur. Prospect., Elsevier, 2017: pp. 129–158. https://doi.org/10.1016/B978-0-12-801300-7.00004-8.

[49] T. Hubáček, A. Hospodková, K. Kuldová, J. Oswald, J. Pangrác, V. Jarý, F. Dominec, M. Slavická Zíková, F. Hájek, E. Hulicius, A. Vetushka, G. Ledoux, C. Dujardin, M. Nikl, Advancement toward ultra-thick and bright InGaN/GaN structures with a high number of QWs, CrystEngComm. 21 (2019) 356–362. https://doi.org/10.1039/C8CE01830H.

[50] P. Lecoq, Pushing the Limits in Time-of-Flight PET Imaging, IEEE Trans. Radiat. Plasma Med. Sci. 1 (2017) 473–485. https://doi.org/10.1109/TRPMS.2017.2756674.

[51] R.M. Turtos, S. Gundacker, S. Omelkov, B. Mahler, A.H. Khan, J. Saaring, Z. Meng, A. Vasil'ev, C. Dujardin, M. Kirm, I. Moreels, E. Auffray, P. Lecoq, On the use of CdSe scintillating nanoplatelets as time taggers for high-energy gamma detection, Npj 2D Mater. Appl. 2019 31. 3 (2019) 1–10. https://doi.org/10.1038/s41699-019-0120-8.

[52] P. Lecoq, C. Morel, J.O. Prior, D. Visvikis, S. Gundacker, E. Auffray, P. Križan, R.M. Turtos, D. Thers, E. Charbon, J. Varela, C. De La Taille, A. Rivetti, D. Breton, J.F. Pratte, J. Nuyts, S. Surti, S. Vandenberghe, P. Marsden, K. Parodi, J.M. Benlloch, M. Benoit, Roadmap toward the 10 ps time-of-flight PET challenge, Phys. Med. Biol. 65 (2020) 21RM01. https://doi.org/10.1088/1361-6560/AB9500.

[53] J.L. Lyons, C.G. Van De Walle, Computationally predicted energies and properties of defects in GaN, Npj Comput. Mater. 2017 31. 3 (2017) 1–10. https://doi.org/10.1038/s41524-017-0014-2.

[54] E. Kioupakis, D. Steiauf, P. Rinke, K.T. Delaney, C.G. Van De Walle, First-principles calculations of indirect Auger recombination in nitride semiconductors, Phys. Rev. B - Condens. Matter Mater. Phys. 92 (2015) 035207. https://doi.org/10.1103/PHYSREVB.92.035207/FIGURES/17/MEDIUM.

[55] J.L. Lyons, E.R. Glaser, M.E. Zvanut, S. Paudel, M. Iwinska, T. Sochacki, M. Bockowski, Carbon complexes in highly C-doped GaN, Phys. Rev. B. 104 (2021) 075201. https://doi.org/10.1103/PHYSREVB.104.075201/FIGURES/7/MEDIUM.

[56] Z. Ye, S. Nitta, Y. Honda, M. Pristovsek, H. Amano, Analysis of trimethylgallium decomposition

by high-resolution mass spectrometry, Jpn. J. Appl. Phys. 59 (2020) 025511. https://doi.org/10.35848/1347-4065/AB6FB0.

[57] J.A. Mccaulley, R.J. Shul, V.M. Donnelly, Kinetics of thermal decomposition of triethylgallium, trimethylgallium, and trimethylindium adsorbed on GaAs(100) ARTICLES YOU MAY BE INTERESTED IN, J. Vac. Sci. Technol. A. 9 (1991) 2872. https://doi.org/10.1116/1.577146.

[58] S. Wu, X. Yang, H. Zhang, L. Shi, Q. Zhang, Q. Shang, Z. Qi, Y. Xu, J. Zhang, N. Tang, X. Wang, W. Ge, K. Xu, B. Shen, Unambiguous Identification of Carbon Location on the N Site in Semi-insulating GaN, Phys. Rev. Lett. 121 (2018). https://doi.org/10.1103/PhysRevLett.121.145505.

[59] K. Irmscher, I. Gamov, E. Nowak, G. Gärtner, F. Zimmermann, F.C. Beyer, E. Richter, M. Weyers, G. Tränkle, Tri-carbon defects in carbon doped GaN, Appl. Phys. Lett. 113 (2018) 262101. https://doi.org/10.1063/1.5064432.

[60] T. Zhu, R.A. Oliver, Unintentional doping in GaN, Phys. Chem. Chem. Phys. 14 (2012) 9558–9573. https://doi.org/10.1039/C2CP40998D.

[61] B. Rackauskas, M.J. Uren, S. Stoffels, M. Zhao, S. Decoutere, M. Kuball, Determination of the self-compensation ratio of carbon in AlGaN for HEMTs, IEEE Trans. Electron Devices. 65 (2018) 1838–1842. https://doi.org/10.1109/TED.2018.2813542.

[62] S. Fischer, C. Wetzel, E.E. Haller, B.K. Meyer, On p-type doping in GaN - acceptor binding energies, Appl. Phys. Lett. 67 (1995) 1298. https://doi.org/10.1063/1.114403.

[63] M.A. Reshchikov, J.D. McNamara, F. Zhang, M. Monavarian, A. Usikov, H. Helava, Y. Makarov, H. Morkoç, Zero-phonon line and fine structure of the yellow luminescence band in GaN, Phys. Rev. B. 94 (2016) 035201. https://doi.org/10.1103/PHYSREVB.94.035201/FIGURES/7/MEDIUM.

[64] M.A. Reshchikov, J.D. McNamara, H. Helava, A. Usikov, Y. Makarov, Two yellow luminescence bands in undoped GaN, Sci. Reports 2018 81. 8 (2018) 1–11. https://doi.org/10.1038/s41598-018-26354-z.

[65] M.A. Reshchikov, M. Vorobiov, D.O. Demchenko, Ozgur, H. Morkoç, A. Lesnik, M.P. Hoffmann, F. Hörich, A. Dadgar, A. Strittmatter, Two charge states of the C N acceptor in GaN: Evidence from photoluminescence, Phys. Rev. B. 98 (2018) 125207. https://doi.org/10.1103/PHYSREVB.98.125207/FIGURES/17/MEDIUM.

[66] T. Ogino, M. Aoki, Mechanism of yellow luminescence in GaN, Jpn. J. Appl. Phys. 19 (1980) 2395–2405. https://doi.org/10.1143/JJAP.19.2395/XML.

[67] J.L. Lyons, A. Janotti, C.G. Van De Walle, Carbon impurities and the yellow luminescence in GaN, Appl. Phys. Lett. 97 (2010) 152108. https://doi.org/10.1063/1.3492841.

[68] M.A. Reshchikov, Measurement and analysis of photoluminescence in GaN, J. Appl. Phys. 129 (2021) 121101. https://doi.org/10.1063/5.0041608.

[69] M.A. Reshchikov, Fine Structure of the Carbon-Related Blue Luminescence Band in GaN, Solids 2022, Vol. 3, Pages 231-236. 3 (2022) 231–236. https://doi.org/10.3390/SOLIDS3020016.

[70] J. Yang, D.G. Zhao, D.S. Jiang, P. Chen, Z.S. Liu, J.J. Zhu, X.J. Li, X.G. He, J.P. Liu, L.Q. Zhang, H. Yang, Y.T. Zhang, G.T. Du, Q.H. Mao, J.L. Liu, X.M. Wu, J.L. Zhang, C.B. Xiong, C.L. Mo, M. Zhang, F. Jiang, L.C. Le, Y. Lei, Z.Q. Liu, M. He, X.Y. Yi, J.X. Wang, J.M. Li, S.W. Zheng, S.T. Li, G. He, S.M. Zhang, H. Wang, A. Brostowski, U.W. Pohl, D. Bimberg, E. Hahn, J.K. Kim, E.F. Schubert, D.D. Koleske, M.H. Crawford, S.R. Lee, A.J. Fischer, G. Thaler, M.A. Banas, Emission efficiency enhanced by reducing the concentration of residual carbon impurities in

InGaN/GaN multiple quantum well light emitting diodes, Opt. Express, Vol. 24, Issue 13, Pp. 13824-13831. 24 (2016) 13824–13831. https://doi.org/10.1364/OE.24.013824.

[71] J.I. Pankove, J.E. Berkeyheiser, E.A. Miller, Properties of Zn-doped GaN. I. Photoluminescence, J. Appl. Phys. 45 (2003) 1280. https://doi.org/10.1063/1.1663402.

[72] D.O. Demchenko, M.A. Reshchikov, Blue luminescence and Zn acceptor in GaN, Phys. Rev. B. 88 (2013) 115204. https://doi.org/10.1103/PhysRevB.88.115204.

[73] M.A. Reshchikov, H. Morkǫ, Luminescence properties of defects in GaN, J. Appl. Phys. 97 (2005). https://doi.org/10.1063/1.1868059.

[74] J. Neugebauer, C.G. Van de Walle, Native defects and impurities in GaN, (1996) 25–44. https://doi.org/10.1007/BFB0107538.

[75] J. Oila, V. Ranki, J. Kivioja, K. Saarinen, P. Hautojärvi, J. Likonen, J.M. Baranowski, K. Pakula, T. Suski, M. Leszczynski, I. Grzegory, Influence of dopants and substrate material on the formation of Ga vacancies in epitaxial GaN layers, Phys. Rev. B. 63 (2001) 045205. https://doi.org/10.1103/PhysRevB.63.045205.

[76] F. Tuomisto, K. Saarinen, B. Lucznik, I. Grzegory, H. Teisseyre, T. Suski, S. Porowski, P.R. Hageman, J. Likonen, Effect of growth polarity on vacancy defect and impurity incorporation in dislocation-free GaN, Appl. Phys. Lett. 86 (2005) 031915. https://doi.org/10.1063/1.1854745.

[77] K. Saarinen, T. Laine, S. Kuisma, J. Nissila, P. Hautojarvi, L. Dobrzynski, J.M. Baranowski, K. Pakula, R. Stepniewski, M. Wojdak, A. Wysmolek, T. Suski, M. Leszczynski, I. Grzegory, S. Porowski, Observation Of Native Ga Vacancies In Gan By Positron Annihilation, MRS Online Proc. Libr. 482 (1997) 757–762. https://doi.org/10.1557/PROC-482-757.

[78] C.E. Dreyer, A. Alkauskas, J.L. Lyons, J.S. Speck, C.G. Van De Walle, Gallium vacancy complexes as a cause of Shockley-Read-Hall recombination in III-nitride light emitters, Appl. Phys. Lett. 108 (2016) 141101. https://doi.org/10.1063/1.4942674.

[79] S. Hautakangas, I. Makkonen, V. Ranki, M.J. Puska, K. Saarinen, X. Xu, D.C. Look, Direct evidence of impurity decoration of Ga vacancies in GaN from positron annihilation spectroscopy, Phys. Rev. B - Condens. Matter Mater. Phys. 73 (2006) 193301. https://doi.org/10.1103/PHYSREVB.73.193301/FIGURES/4/MEDIUM.

[80] S. Suihkonen, S. Pimputkar, J.S. Speck, S. Nakamura, Infrared absorption of hydrogen-related defects in ammonothermal GaN, Appl. Phys. Lett. 108 (2016) 202105. https://doi.org/10.1063/1.4952388.

[81] J. Neugebauer, C.G. Van de Walle, Gallium vacancies and the yellow luminescence in GaN, Appl. Phys. Lett. 69 (1998) 503. https://doi.org/10.1063/1.117767.

[82] J.L. Lyons, A. Alkauskas, A. Janotti, C.G. Van de Walle, First-principles theory of acceptors in nitride semiconductors, Phys. Status Solidi. 252 (2015) 900–908. https://doi.org/10.1002/PSSB.201552062.

[83] F. Wu, Y. Da Lin, A. Chakraborty, H. Ohta, S.P. Denbaars, S. Nakamura, J.S. Speck, Stacking fault formation in the long wavelength InGaN/GaN multiple quantum wells grown on m-plane GaN, Appl. Phys. Lett. 96 (2010) 231912. https://doi.org/10.1063/1.3447940.

[84] M.B. McLaurin, A. Hirai, E. Young, F. Wu, J.S. Speck, Basal plane stacking-fault related anisotropy in X-ray rocking curve widths of m-plane GaN, Jpn. J. Appl. Phys. 47 (2008) 5429–5431. https://doi.org/10.1143/JJAP.47.5429/XML.

[85] B. Ding, M. Frentrup, S.M. Fairclough, M.J. Kappers, M. Jain, A. Kovács, D.J. Wallis, R.A. Oliver, Alloy segregation at stacking faults in zincblende GaN heterostructures, J. Appl. Phys. 128 (2020) 145703. https://doi.org/10.1063/5.0015157.

[86] S.A. Church, S. Hammersley, P.W. Mitchell, M.J. Kappers, L.Y. Lee, F. Massabuau, S.L. Sahonta, M. Frentrup, L.J. Shaw, D.J. Wallis, C.J. Humphreys, R.A. Oliver, D.J. Binks, P. Dawson, Effect of stacking faults on the photoluminescence spectrum of zincblende GaN, J. Appl. Phys. 123 (2018) 185705. https://doi.org/10.1063/1.5026267.

[87] P.M.F.J. Costa, R. Datta, M.J. Kappers, M.E. Vickers, C.J. Humphreys, D.M. Graham, P. Dawson, M.J. Godfrey, E.J. Thrush, J.T. Mullins, Misfit dislocations in In-rich InGaN/GaN quantum well structures, Phys. Status Solidi. 203 (2006) 1729–1732. https://doi.org/10.1002/PSSA.200565219.

[88] S.E. Bennett, Dislocations and their reduction in GaN, Mater. Sci. Technol. 26 (2010) 1017–1028. https://doi.org/10.1179/026708310X12668415533685.

[89] X.J. Ning, F.R. Chien, P. Pirouz, J.W. Yang, M. Asif Khan, Growth defects in GaN films on sapphire: The probable origin of threading dislocations, J. Mater. Res. 11 (1996) 580–592. https://doi.org/10.1557/JMR.1996.0071.

[90] X.H. Wu, P. Fini, E.J. Tarsa, B. Heying, S. Keller, U.K. Mishra, S.P. DenBaars, J.S. Speck, Dislocation generation in GaN heteroepitaxy, J. Cryst. Growth. 189–190 (1998) 231–243. https://doi.org/10.1016/S0022-0248(98)00240-1.

[91] V. Narayanan, K. Lorenz, W. Kim, S. Mahajan, Origins of threading dislocations in GaN epitaxial layers grown on sapphire by metalorganic chemical vapor deposition, Appl. Phys. Lett. 78 (2001) 1544. https://doi.org/10.1063/1.1352699.

[92] B. Heying, X.H. Wu, S. Keller, Role of threading dislocation structure on the x-ray diffraction peak widths in epitaxial GaN films ARTICLES YOU MAY BE INTERESTED IN, Appl. Phys. Lett. 68 (1996) 643. https://doi.org/10.1063/1.116495.

[93] P. Gay, P.B. Hirsch, A. Kelly, The estimation of dislocation densities in metals from X-ray data, Acta Metall. 1 (1953) 315–319. https://doi.org/10.1016/0001-6160(53)90106-0.

[94] V. Ivantsov, A. Volkova, A Comparative Study of Dislocations in HVPE GaN Layers by High-Resolution X-Ray Diffraction and Selective Wet Etching, ISRN Condens. Matter Phys. 2012 (2012) 1–6. https://doi.org/10.5402/2012/184023.

[95] S.R. Lee, A.M. West, A.A. Allerman, K.E. Waldrip, D.M. Follstaedt, P.P. Provencio, D.D. Koleske, C.R. Abernathy, Effect of threading dislocations on the Bragg peakwidths of GaN, AlGaN, and AlN heterolayers, Appl. Phys. Lett. 86 (2005) 241904. https://doi.org/10.1063/1.1947367.

[96] V.M. Kaganer, O. Brandt, A. Trampert, K.H. Ploog, X-ray diffraction peak profiles from threading dislocations in GaN epitaxial films, Phys. Rev. B. 72 (2005) 045423. https://doi.org/10.1103/PhysRevB.72.045423.

[97] V.S. Kopp, V.M. Kaganer, M. V. Baidakova, W. V. Lundin, A.E. Nikolaev, E. V. Verkhovtceva, M.A. Yagovkina, N. Cherkashin, X-ray determination of threading dislocation densities in GaN/Al2O3(0001) films grown by metalorganic vapor phase epitaxy, J. Appl. Phys. 115 (2014) 073507. https://doi.org/10.1063/1.4865502.

[98] M. Barchuk, V. Holý, B. Miljević, B. Krause, T. Baumbach, J. Hertkorn, F. Scholz, X-ray diffuse scattering from threading dislocations in epitaxial GaN layers, J. Appl. Phys. 108 (2010) 043521. https://doi.org/10.1063/1.3460803.

[99] T. Sugahara, H. Sato, M. Hao, Y. Naoi, S. Kurai, S. Tottori, K. Yamashita, K. Nishino, L.T. Romano, S. Sakai, Direct evidence that dislocations are non-radiative recombination centers in GaN, Jpn. J. Appl. Phys. 37 (1998) L398–L400. https://doi.org/10.1143/JJAP.37.L398/XML.

[100] D. Cherns, S.J. Henley, F.A. Ponce, Edge and screw dislocations as nonradiative centers in InGaN/GaN quantum well luminescence, Appl. Phys. Lett. 78 (2001) 2691. https://doi.org/10.1063/1.1369610.

[101] D. Cherns, C.G. Jiao, Electron Holography Studies of the Charge on Dislocations in GaN, Phys. Rev. Lett. 87 (2001) 205504. https://doi.org/10.1103/PhysRevLett.87.205504.

[102] H.M. Ng, D. Doppalapudi, T.D. Moustakas, N.G. Weimann, L.F. Eastman, The role of dislocation scattering in n-type GaN films, Appl. Phys. Lett. 73 (1998) 821. https://doi.org/10.1063/1.122012.

[103] C.Y. Chang, H. Li, Y.T. Shih, T.C. Lu, Manipulation of nanoscale V-pits to optimize internal quantum efficiency of InGaN multiple quantum wells, Appl. Phys. Lett. 106 (2015) 091104. https://doi.org/10.1063/1.4914116.

[104] F. Lin, N. Xiang, P. Chen, S.Y. Chow, S.J. Chua, Investigation of the V-pit related morphological and optical properties of InGaN⁄GaN multiple quantum wells, J. Appl. Phys. 103 (2008) 043508. https://doi.org/10.1063/1.2884534.

[105] L. Wang, J. Jin, Z. Hao, Y. Luo, C. Sun, Y. Han, B. Xiong, J. Wang, H. Li, V-shaped semipolar InGaN/GaN multi-quantum-well light-emitting diodes directly grown on c-plane patterned sapphire substrates, Phys. Status Solidi. 214 (2017) 1600810. https://doi.org/10.1002/PSSA.201600810.

[106] I.H. Kim, H.S. Park, Y.J. Park, T. Kim, Formation of V-shaped pits in InGaN/GaN multiquantum wells and bulk InGaN films, Appl. Phys. Lett. 73 (1998) 1634. https://doi.org/10.1063/1.122229.

[107] F. Scholz, A. Sohmer, J. Off, V. Syganow, A. Dörnen, J.S. Im, A. Hangleiter, H. Lakner, In incorporation efficiency and composition fluctuations in MOVPE grown GaInN/GaN hetero structures and quantum wells, Mater. Sci. Eng. B. 50 (1997) 238–244. https://doi.org/10.1016/S0921-5107(97)00184-0.

[108] I.A. Ajia, P.R. Edwards, Y. Pak, E. Belekov, M.A. Roldan, N. Wei, Z. Liu, R.W. Martin, I.S. Roqan, Generated Carrier Dynamics in V-Pit-Enhanced InGaN/GaN Light-Emitting Diode, ACS Photonics. 5 (2018) 820–826. https://doi.org/10.1021/ACSPHOTONICS.7B00944/ASSET/IMAGES/LARGE/PH-2017-00944J_0006.JPEG.

[109] R. Bouveyron, M. Mrad, M. Charles, V-pit pinning at the interface of high and low-temperature gallium nitride growth, Jpn. J. Appl. Phys. 58 (2019) SC1035. https://doi.org/10.7567/1347-4065/AB09D8.

[110] Z.-Y. Gao, 高志远, X.-W. Xue, 薛晓玮, J.-J. Li, 李江江, X. Wang, 王勋, Y.-H. Xing, 邢艳辉, B.-F. Cui, 崔碧峰, D.-S. Zou, 邹德恕, Understanding of surface pit formation mechanism of GaN grown in MOCVD based on local thermodynamic equilibrium assumption*, Chinese Phys. B. 25 (2016) 066105. https://doi.org/10.1088/1674-1056/25/6/066105.

[111] F.C. Frank, Capillary equilibria of dislocated crystals, Acta Crystallogr. 4 (1951) 497–501. https://doi.org/10.1107/S0365110X51001690.

[112] Q. Sun, C.D. Yerino, B. Leung, J. Han, M.E. Coltrin, Understanding and controlling

heteroepitaxy with the kinetic Wulff plot: A case study with GaN, J. Appl. Phys. 110 (2011) 053517. https://doi.org/10.1063/1.3632073.

[113] H.M. Ng, D. Doppalapudi, T.D. Moustakas, N.G. Weimann, L.F. Eastman, The role of dislocation scattering in n-type GaN films, Appl. Phys. Lett. 73 (1998) 821. https://doi.org/10.1063/1.122012.

[114] X. Wu, J. Liu, F. Jiang, Hole injection from the sidewall of V-shaped pits into c-plane multiple quantum wells in InGaN light emitting diodes, J. Appl. Phys. 118 (2015) 164504. https://doi.org/10.1063/1.4934503.

[115] Y. Li, F. Yun, X. Su, S. Liu, W. Ding, X. Hou, Deep hole injection assisted by large V-shape pits in InGaN/GaN multiple-quantum-wells blue light-emitting diodes, J. Appl. Phys. 116 (2014) 123101. https://doi.org/10.1063/1.4896362.

[116] L. Royer, Recherches expérimentales sur l'épitaxie ou orientation mutuelle de cristaux d'espèces différentes, Bull. Minéralogie. 51 (1928) 7–159. https://doi.org/10.3406/BULMI.1928.4034.

[117] C.A. Wang, Early history of MOVPE reactor development, J. Cryst. Growth. 506 (2019) 190–200. https://doi.org/10.1016/J.JCRYSGRO.2018.10.004.

[118] G.B. Stringfellow, A critical appraisal of growth mechanisms in MOVPE, J. Cryst. Growth. 68 (1984) 111–122. https://doi.org/10.1016/0022-0248(84)90405-6.

[119] KIT IPS - Methods & Facilities - SCATTERING Cluster, (n.d.). https://www.ips.kit.edu/5880.php (accessed January 6, 2023).

[120] N. Kaminski, … O.H.-7th I.C. on I., undefined 2012, SiC and GaN devices-competition or coexistence?, Ieeexplore.Ieee.Org. (n.d.). https://ieeexplore.ieee.org/abstract/document/6170654/?casa_token=Nq_1JBQcEnEAAAAA:FBqwtS7nA2mO5erdyXSKAzOCt2amwOiQZr2qf3i-B7mBntpE0QJ7nGc5cLEFOUb849LRi7-uPbU (accessed November 8, 2022).

[121] M. Slomski, L. Liu, J.F. Muth, T. Paskova, Growth Technology for GaN and AlN Bulk Substrates and Templates, Handb. GaN Semicond. Mater. Devices. (2017) 143–167. https://doi.org/10.1201/9781315152011-5/GROWTH-TECHNOLOGY-GAN-ALN-BULK-SUBSTRATES-TEMPLATES-MICHAEL-SLOMSKI-LIANGHONG-LIU-JOHN-MUTH-TANIA-PASKOVA.

[122] D.D. Koleske, III-Nitride Metalorganic Vapor-Phase Epitaxy, Handb. GaN Semicond. Mater. Devices. (2017) 169–242. https://doi.org/10.1201/9781315152011-6.

[123] E. Lórincz, G. Erdei, I. Péczeli, C. Steinbach, F. Ujhelyi, T. Bükki, Modeling and optimization of scintillator arrays for PET detectors, IEEE Trans. Nucl. Sci. 57 (2010) 48–54. https://doi.org/10.1109/TNS.2009.2038215.

[124] I. Pelant, J. Valenta, Luminescence spectroscopy of semiconductors, OUP Oxford, 2012.

[125] J.F. Muth, J.D. Brown, M.A.L. Johnson, Y.U. Zhonghai, R.M. Kolbas, J.W. Cook, J.F. Schetzina, Absorption Coefficient and Refractive Index of GaN, AIN and AlGaN Alloys, Undefined. 537 (1998). https://doi.org/10.1557/PROC-537-G5.2.

[126] R. Krause-Rehberg, H.S. Leipner, Positron Annihilation in Semiconductors, 127 (1999). https://doi.org/10.1007/978-3-662-03893-2.

[127] M.J. Puska, R.M. Nieminen, Theory of positrons in solids and on solid surfaces, Rev. Mod. Phys. 66 (1994) 841. https://doi.org/10.1103/RevModPhys.66.841.

[128] F. Gabriel, P. Gippner, E. Grosse, D. Janssen, P. Michel, H. Prade, A. Schamlott, W. Seidel, A. Wolf, R. Wünsch, The Rossendorf radiation source ELBE and its FEL projects, Nucl. Instruments Methods Phys. Res. Sect. B Beam Interact. with Mater. Atoms. 161–163 (2000) 1143–1147. https://doi.org/10.1016/S0168-583X(99)00909-X.

[129] R.M. Turtos, S. Gundacker, S. Omelkov, E. Auffray, P. Lecoq, Light yield of scintillating nanocrystals under X-ray and electron excitation, J. Lumin. 215 (2019) 116613. https://doi.org/10.1016/J.JLUMIN.2019.116613.

[130] D.G. Thomas, J.J. Hopfield, W.M. Augustyniak, Kinetics of Radiative Recombination at Randomly Distributed Donors and Acceptors, Phys. Rev. 140 (1965) A202. https://doi.org/10.1103/PhysRev.140.A202.

[131] H. Reiss, C.S. Fuller, F.J. Morin, Chemical Interactions Among Defects in Germanium and Silicon, Bell Syst. Tech. J. 35 (1956) 535–636. https://doi.org/10.1002/J.1538-7305.1956.TB02393.X.

[132] R. Bindemann, K. Unger, On the Spectral Intensity Distribution of Donor–Acceptor Pair Recombination in GaP, Phys. Status Solidi. 66 (1974) 133–143. https://doi.org/10.1002/PSSB.2220660114.

[133] Y. Lei, 雷勇, H. Shi, 石宏彪, H. Lu, 陆海, D. Chen, 陈敦军, R. Zhang, 张荣, Y. Zheng, 郑有炓, Field plate engineering for GaN-based Schottky barrier diodes, J. Semicond. 34 (2013) 054007. https://doi.org/10.1088/1674-4926/34/5/054007.

[134] T. Hubáček, K. Kuldová, Z. Gedeonová, F. Hájek, T. Košutová, S. Banerjee, P. Hubík, J. Pangrác, T. Vaněk, A. Hospodková, Impact of Ge doping on MOVPE grown InGaN layers, J. Cryst. Growth. 604 (2023) 127043. https://doi.org/10.1016/J.JCRYSGRO.2022.127043.

[135] M. Grabowski, E. Grzanka, S. Grzanka, A. Lachowski, J. Smalc-Koziorowska, R. Czernecki, R. Hrytsak, J. Moneta, G. Gawlik, A. Turos, M. Leszczyński, The impact of point defects in n-type GaN layers on thermal decomposition of InGaN/GaN QWs, Sci. Reports 2021 111. 11 (2021) 1–11. https://doi.org/10.1038/s41598-021-81017-w.

[136] C. Haller, J.F. Carlin, G. Jacopin, W. Liu, D. Martin, R. Butté, N. Grandjean, GaN surface as the source of non-radiative defects in InGaN/GaN quantum wells, Appl. Phys. Lett. 113 (2018) 111106. https://doi.org/10.1063/1.5048010.

[137] J.C. Slater, Atomic Radii in Crystals, J. Chem. Phys. 41 (2004) 3199. https://doi.org/10.1063/1.1725697.

[138] J. Zhu, F. Liu, G.B. Stringfellow, S.H. Wei, Strain-enhanced doping in semiconductors: Effects of dopant size and charge state, Phys. Rev. Lett. 105 (2010) 195503. https://doi.org/10.1103/PHYSREVLETT.105.195503/FIGURES/3/MEDIUM.

6 Papers

Journal of Alloys and Compounds 914 (2022) 165255

Contents lists available at ScienceDirect

Journal of Alloys and Compounds

journal homepage: www.elsevier.com/locate/jalcom

Acceleration of the yellow band luminescence in GaN layers via Si and Ge doping

Tomáš Vaněk[a,b,*], Vítězslav Jarý[a], Tomáš Hubáček[a], František Hájek[a,c], Karla Kuldová[a], Zuzana Gedeonová[a], Vladimír Babin[a], Zdeněk Remeš[a], Maksym Buryi[a]

[a] Institute of Physics CAS, v.v.i., Cukrovarnická 10, 16200 Prague 6, Czech Republic
[b] Technical University of Liberec, Studentská 2, 46117 Liberec, Czech Republic
[c] Faculty of Nuclear Sciences and Physical Engineering, Czech Technical University in Prague, Břehová 7, 11519 Praha 1, Czech Republic

ARTICLE INFO

Article history:
Received 29 December 2021
Received in revised form 26 April 2022
Accepted 27 April 2022
Available online 30 April 2022

Keywords:
A. Semiconductors
A. Nitride materials
B. Vapor deposition
C. Optical properties
D. Luminescence

ABSTRACT

A huge acceleration of the yellow band defect luminescence (YB) with increasing Si and Ge doping concentration in GaN layers has been observed and studied. The donor doping concentrations in the n-type GaN varied from 5×10^{16} cm^{-3} to 1.5×10^{19} cm^{-3} for undoped, Si-doped, and Ge-doped samples. Consequently, the fastest component of the photoluminescence (PL) decay time curve accelerated from 0.9 ms to 40.3 ns, and the mean decay time from 20 ms to 260 ns with increasing doping concentration. We have proposed an explanation based on a theoretical model of donor-acceptor pair transition (DAP) and electron-acceptor (e-A^0) recombination at higher dopant concentrations, which is supported by several measurement techniques as room-temperature radioluminescence (RL), PL measurements or thermally stimulated luminescence (TSL). Last but not least, we have shown a change in the morphology of samples with the increasing dopant concentration, especially 3D columns formation with the high level of Si-doping and its influence on the light extraction from the GaN layer. The paper shows an uncommon way of dealing with slow unwanted YB, which detriment the GaN luminescence properties.

1. Introduction

Nitride semiconductor heterostructures have been widely studied since the first efficient blue LEDs were discovered in the early 90th by Nakamura [1]. Their huge spread to the luminescent, high-frequency, solar-cell and other applications [2–6] has been caused by its suitable physical properties such as high exciton binding energy, relatively wide direct bandgap (3.4 eV at room temperature), and radiation and chemical stability. Furthermore, the possibility of creating alloys (replacing Ga atoms with Al and In) and consequently heterostructures gave them an advantage compared to concurrent semiconductors like SiC. The advantage is, for example, in producing structures with two-dimensional electron gas (AlGaN HEMTs for high-frequency applications) or highly luminescently efficient InGaN/GaN MQW structures [7–9].

For the successful invention of blue LEDs, it was necessary to grow n-doped GaN layers with sufficient quality. Silicon or germanium are usually used as n-type dopants, and we can easily control free electron concentration with the level of Si or Ge doping [10,11]. Si- or Ge-doped GaN layers can be grown with Metal-Organic Vapour Phase Epitaxy (MOVPE). Both atoms act as shallow donors with similar donor ionization energy [12]. The intensity of the excitonic band increases with Si and Ge doping level [11,13]. On the other hand, the increase of Si or Ge doping level is also connected with a rise in YB intensity, which is usually observed in luminescence spectra of MOVPE grown n-doped GaN layers [14,15]. It can be detrimental for some applications, where fast decay time without any slow components is necessary because YB decay time can be in the μs scale [16]. Typical examples are applications of higher energy radiation detection where the particle has enough energy to excite the whole structure, and the YB forms a substantial part of outcoming luminescence. Thus, a vast scientific effort has been made to get rid of or at least suppress the YB [17]. In this paper, we show another possible way for dealing with the YB by accelerating its decay.

The main goal of this article is a better understanding of the luminescence processes in differently doped GaN layers grown by MOVPE technology. Therefore, we show the influence of Si and Ge doping in the concentration range of free electrons from 1.33×10^{18} cm^{-3} to 1.64×10^{19} cm^{-3} at room temperature (RT) on the luminescence and morphological properties of GaN layers.

* Corresponding author at: Institute of Physics CAS, v.v.i., Cukrovarnická 10, 16200 Prague 6, Czech Republic.
E-mail address: vanekt@fzu.cz (T. Vaněk).

https://doi.org/10.1016/j.jallcom.2022.165255
0925-8388/

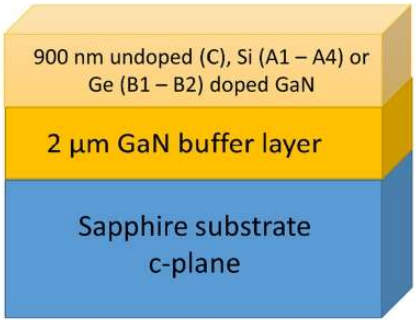

Fig. 1. The schematic picture of investigated samples. The upper 900 nm thick part of the structure was changed.

2. Experimental

AIXTRON 3 × 2″ CCS MOVPE apparatus was used for the growth of all samples. Samples were prepared on c-plane sapphire substrates. LT GaN nucleation layer with high-temperature coalescence GaN growth was used for all samples (thickness around 2 µm) followed with 900 nm thick n-doped GaN layer. The schematic picture of the structures is shown in Fig. 1. Trimethylgallium and NH_3 were used as precursors with H_2 carrier gas. SiH_4 or GeH_4 precursors were used for n-type doping. Growth parameters were kept constant during the growth of both GaN layers and only differed in the flow of SiH_4 or GeH_4. N-doped layers were grown at 150 mbar reactor pressure, 1800 sccm NH_3 flow, 25 sccm TMGa flow, and with 1447 V/III ratio. One undoped, four Si-doped, and two Ge-doped samples were grown and studied in this article. A description of all samples is given in Table 1.

Room-temperature Hall concentrations were measured using the van der Pauw method. Samples of square shape (approx. 10 mm × 10 mm) were provided with soldered indium contacts in the corners. A Keithley 6221 model was used as a current source and a Keithley 2182 A model as a nanovoltmeter. Alternating current polarities were applied to compensate for possible thermoelectric effects. A magnetic field of ± 0.2 T was applied during the Hall effect measurement. The concentration of free electrons in sample C could not be determined by Hall measurement because of the parasitic channel formed at the sapphire/GaN interface with conductivity higher than in the undoped layer [18]. Therefore, the concentration was obtained by the C-V method with a Hg probe.

Room-temperature RL and PL spectra connected with PL decay curves were measured by a custom-made spectrofluorometer 5000 M (Horiba Jobin Yvon, Wildwood, MA, USA) using Mo X-ray tube (40 kV, 15 mA, Seifert) and microsecond xenon pulsed flash lamp (slow decays measured by multichannel scaling technique, Edinburgh Instruments) or nanosecond nanoLED pulsed light sources (fast prompt decay curves measured by time-correlated single-photon counting technique, Hamamatsu) as the excitation sources, respectively. The detection part of the setup involved a single-grating monochromator and a photon-counting detector TBX-04 (Hamamatsu). Measured spectra were corrected for the spectral dependence of detection sensitivity for both RL and PL. The convolution procedure was applied to the photoluminescence decay curves to determine true decay times (SpectraSolve software package, Ames Photonics). The thermally stimulated luminescence (TSL) glow curves were also measured using the Horiba Jobin-Yvon 5000 M spectrometer with liquid nitrogen cryostat (Oxford Instruments) and TBX-04 photomultiplier operating in the 200–800 nm spectral range (also analyzed). The samples were irradiated by a Seifert X-ray tube with a tungsten target operated at 40 kV. The TSL was recorded during linear heating of the sample holder.

The white light interferometer (WLI) Zygo NewView 7200 with nanometric accuracy in the *z*-direction was used for the surface characterization. Figures were taken by objectives with magnification 5x and 50x, which makes the effective lateral pixel dimensions 2.19 µm and 220 nm, respectively. Finally, the environmental scanning electron microscope (SEM) Philips XL30 ESEM was used additionally to the WLI figures.

SIMS measurements were performed in EAG laboratories on a commercial base. The samples used for SIMS measurement were two multi-layered samples containing all of the doped layers corresponding to the samples in Table 1.

Table 1
The list of prepared samples.

Sample	Doping	Donor concentration [cm^{-3}]	RT Hall concentration [cm^{-3}]	Mean decay time [s]
A1	Si doped	1.1×10^{18}	1.3×10^{18}	8.7×10^{-5}
A2	Si doped	2.2×10^{18}	2.3×10^{18}	2.6×10^{-5}
A3	Si doped	1.1×10^{19}	1.1×10^{19}	2.6×10^{-7}
A4	Si doped	1.5×10^{19}	1.6×10^{19}	6.3×10^{-7}
B1	Ge doped	7.5×10^{17}	9.4×10^{17}	5.7×10^{-5}
B2	Ge doped	4.3×10^{18}	4.7×10^{18}	1.2×10^{-6}
C	Undoped	5×10^{16}	$< 5 \times 10^{16}$	2.4×10^{-2}

3. Results and discussion

Photoluminescence (PL) decay measurement is a basic characterization method telling us about radiative and non-radiative centers inside the crystal structure. Fig. 2 shows the room temperature PL decay curves connected to the YB (λ_{ex} = 330–340 nm, λ_{em} = 550 nm) for undoped, Si, and Ge-doped samples. The decay curves highly deviating from single exponential curves were approximated by the sum of three exponentials in the following form:

$$I(t) = \sum_{i=1}^{3} A_i e^{-\frac{t}{\tau_i}} + \text{background}, \quad (1)$$

convolved with the instrumental response function, where $I(t)$, A_i, and τ_i stand for intensity as a function of time t (expressed as the number of photons detected in the time interval), the amplitude of i_{th} component, and decay time of an i_{th} component, respectively. Surprisingly, we have observed the rapid (ranging from 0.9 ms to 40.3 ns for the fastest component) decrease of PL decay times of YB luminescence with increasing concentration of dopants either for Si or Ge doping. To describe the influence of effects occurring at room-temperature, such as reemitting charge carriers from donor or acceptor levels back to conduction and valence bands, we have also performed the low-temperature decay measurements (see Table 1S in supplementary materials). The mean decay times were similar to the room-temperature ones, the largest difference being 19.4 µs at 300 K and 85.5 µs at 9 K for sample A1. Since the observed differences were small and the potential application requires the room temperature characterization of the samples to mimic the real operating conditions, we focus on the room temperature measurements in the following discussion.

The origin of the YB luminescence in GaN layers grown by MOVPE technique with usual growth parameters (TMGa precursor, temperature around 1030 °C, H_2 carrier gas, 150 mbar growth pressure) is usually connected with unintentional contamination with carbon. The carbon-related defects such as C_N or complex $C_N - O_N$ act as deep acceptors in the bandgap of GaN, causing a radiative transition of an electron from the conduction band to the acceptor level (e-A^0 transition) or from a shallow donor to the acceptor level (DAP transition) [19,20].

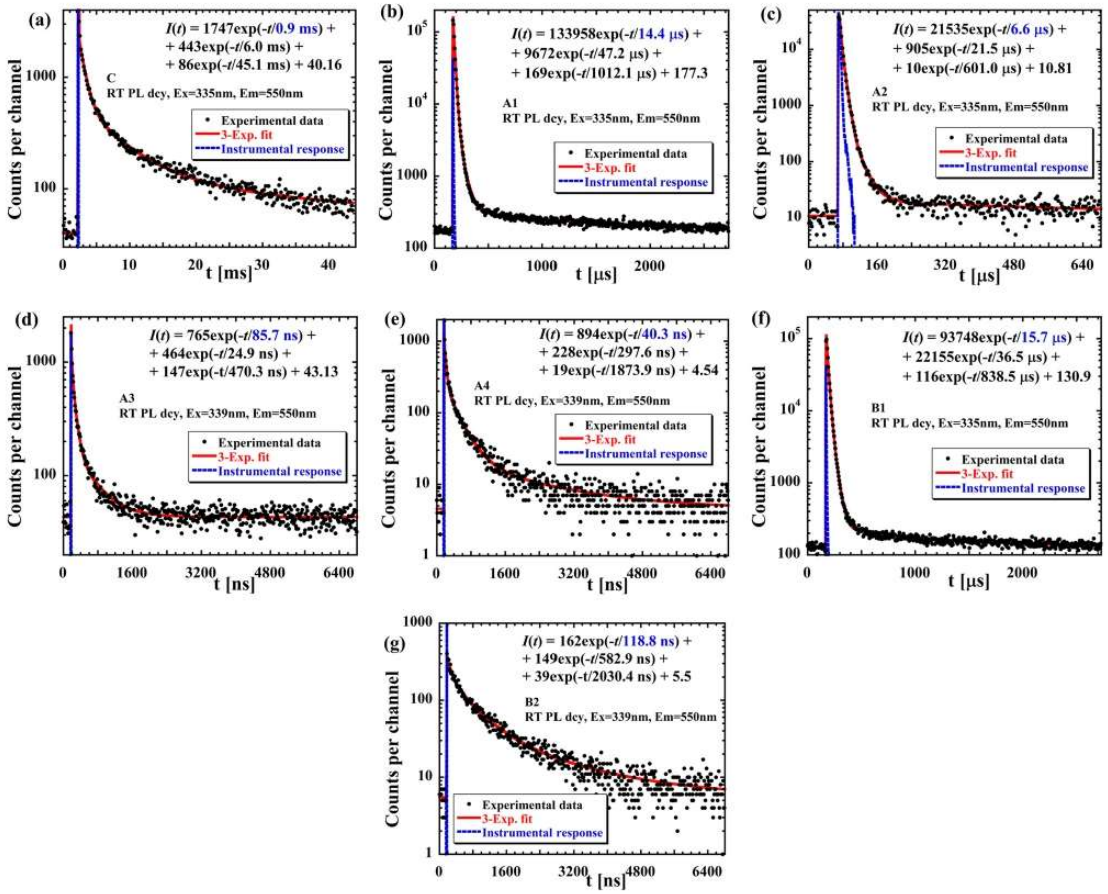

Fig. 2. RT PL decays of YB luminescence (λ_{ex} = 335 nm, λ_{em} = 550 nm) of samples with different Si and Ge doping concentration, (a) C, (b) A1, (c) A2, (d) A3, (e) A4, (f) B1, (g) B2, see Table 1.

In the case of DAP recombination, non-exponential decay is expected since donors at a greater distance from the acceptor have longer decay times. The non-exponential decay time in samples considered degenerated (A3, A4, B2) could be explained by potential fluctuations caused by large ionized donor concentration or/and by competition of two radiative channels with different dependence of luminescence intensity on carrier concentration (free electron-hole vs e-A^0 recombination). It should be noted that free carrier concentration is equal to or even greater than the concentration of Si and Ge donors (see Table 1), suggesting all donors are ionized at room temperature. In non-degenerated samples, these donors can therefore capture non-equilibrium excitons. The oxygen concentration, which also acts as a shallow donor, is about 2×10^{16} cm^{-3} in the samples under study (measured by SIMS). Carbon concentration was even lower (1.1×10^{16} cm^{-3}), suggesting negligible compensation occurs via this deep acceptor. A slightly higher concentration of free electrons than donors can be explained by a small concentration of nitrogen vacancies that probably act as shallow donors but can be hardly identified by any experimental technique or by contribution from conductivity of parasitic channel formed at the sapphire-GaN interface [18].

To ensure that YB is not composed of different luminescence centers, decay curves were measured for different wavelengths 500, 550, and 600 nm, see Fig. 3. All fits of the multi-exponential decay curves have similar decay components, which suggests there is no other luminescence center in the wavelength range of YB at the higher or lower energy side. Therefore, we use the mean decay time, calculated as $MDT = \sum_{i=1}^{3} \tau_i LS_i$, $LS_i = \frac{A_i \tau_i}{\sum_{i=1}^{3} A_i \tau_i}$, see Table 1 at 550 nm for further description of the transition mechanism.

The main task of the paper is to explain observed changes in the decay times with different doping concentrations. Generally, several possible mechanisms can accelerate luminescence. To differentiate the dominant one responsible for the massive shortening of decay time in our samples, we focused on the e-A^0 mechanism with different free electron concentrations and the DAP mechanism with different donor concentrations. Generally, the non-radiative recombination mechanism can also be responsible for decay acceleration, but it influences mainly band to band or exciton emission, which is not the case of the YB luminescence.

However, the evaluation of the amount or origin of non-radiative centers is a crucial application parameter because it directly influences the light yield of the structure, which usually has the great importance in the application as well as the luminescence decay. To study the influence of non-radiative recombination in the samples, the RL spectra at very low excitation density were measured (Fig. 4a and 4b). The RL spectra of Si- and Ge-doped samples contain three clear luminescence bands in the measured spectral range. At the

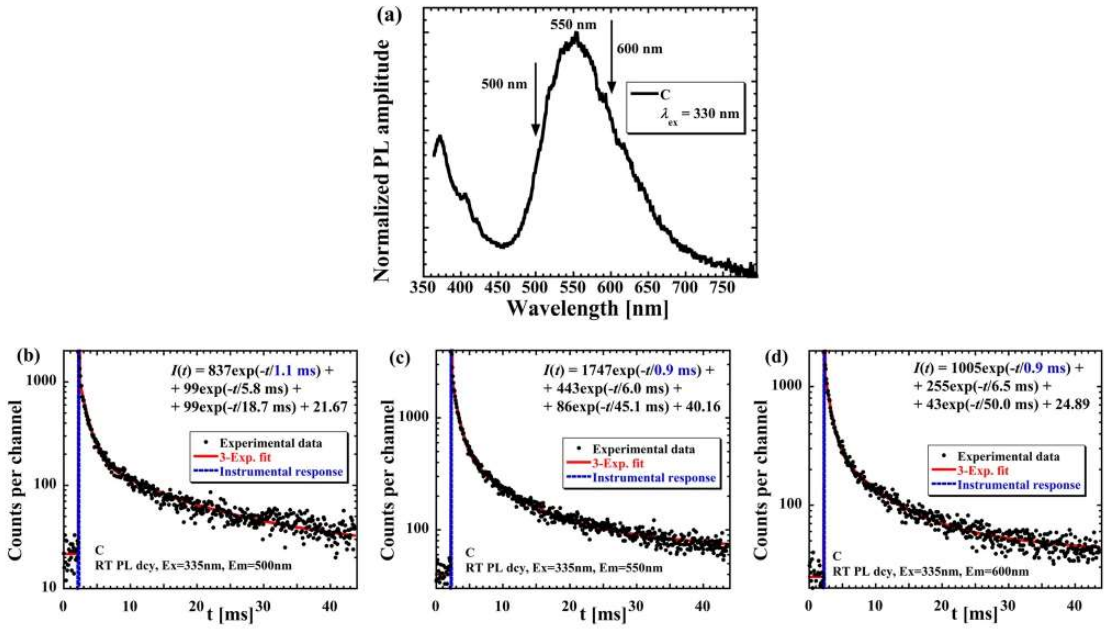

Fig. 3. Comparison of RT PL decays under the 335 nm excitation measured at the different parts of the YB. Emission wavelength set on (a) 500 nm, (b) 550 nm, and (c) 600 nm.

lowest energy side, a sharp peak at 693 nm is present, and it is assigned to the well-known radiative transition $^2E \rightarrow {}^4A_2$ in Cr^{3+} ions in the octahedral crystal field of the substrate (*c*-oriented sapphire Al_2O_3) [21]. At the high energy side, band-edge luminescence of GaN is visible [11], and it can be stated that with increasing Si or Ge doping level, its intensity is conclusively increasing. The opposite trend has been observed for the broad YB peak at around 560 nm, except for the highest Si concentration, as will be discussed later. In Fig. 4c is an evident decreasing trend of integral RL intensity with higher dopant concentration for both dopants (see the blue squares).

The explanation for the decrease can be understood from the TSL measurements that provide us information about trap centers forming in the structure. Fig. 5 shows the TSL glow curves of all samples and bare sapphire substrate. All curves were experimentally obtained under the same conditions. The samples were irradiated by the X-ray source at 77 K. Afterwards, they were heated in the 77–500 K range with the heating rate 0.1 K/s with luminescence signal being simultaneously recorded. Several conclusions can be made here. Firstly, the sapphire substrate does not participate in the processes of TSL within the GaN layers. Secondly, the TSL curves seem to be a superposition of many different TSL peaks, and they look rather similar independently of doping. Therefore, it can be stated that the thermoluminescence processes responsible for the TSL glow curves are of the same origin for undoped and doped samples.

Moreover, their increasing intensity with rising doping concentration indicates forming of a higher concentration of trap centers in strongly doped samples. These traps capture free carriers and can be a source of non-radiative recombination or even very long decay components (usually called after-glow). In both cases, the traped carriers would not contribute to RL spectra because the time of exposure is shorter than the after-glow. The origin of the TSL peak at 380 K for the A2 sample remains unclear for now. The fact that the TSL glow curves are almost identical corresponds very well with the results obtained by EPR (not shown here), in which no clear differences were evidenced among undoped, Si-doped, and Ge-doped samples.

As the suppression of potential after-glow is usually necessary in applications, we have decided to investigate more about the origin of the traps by determining the order of trapping kinetics. The samples were exposed to two different doses of X-ray irradiation (0.1 kGy and 1 kGy) [22]. Since no changes except for the intensity to the TSL glow curves occurred (the glow peak positions remained unchanged), the order of the trapping kinetics has been assumed to be first order. Therefore a number of traps with close values of their depths contributing to the TSL signal can be expected [23].

To deeply investigate the trap filling process, the light excitation (LED at 380 nm = 3.26 eV is within the GaN bandgap (~3.4 eV)) in TSL has been applied. The obtained glow curves had the same shapes as those in Fig. 5. Moreover, their intensities followed the same trend as shown in Fig. 5. This indicates that the traps are quite deep and definitely found lower than 0.14 eV in the bandgap. However, the TSL glow curves are unfortunately not intense enough to do some advanced analysis for the trap depths and frequency factors determination [22]. On the other hand, the low intensity suggests that the potential afterglow will not affect the intended scintillation application.

Finally, as we have pointed out, sample A4 has a much stronger luminescence intensity in RL and TSL figures than others. It is caused by enhanced light extraction due to the higher roughness of surface morphology [24]. After exceeding a critical Si doping concentration, GaN prefers to grow in 3D morphology. The origin of this change in the growth mode seems to be still under discussion as different authors attribute it to the introduction of tensile strain by smaller Si atoms, the change in surface free energy, or even the interaction of point defects with dislocations [25–30]. WLI and SEM measurements in Fig. 6 compare surface morphologies of samples A4 and A3 with the highest Si concentrations (1.5×10^{19} cm^{-3}, 1.1×10^{19} cm^{-3}). We can see that whereas the A3 sample (Fig. 6c,e) still has a relatively smooth character, the surface of the A4 sample (Fig. 6a,b,d) is formed by 3D microcolumns with small V-pits opened inside them. In the case of WLI figures, it is necessary to point out the different scale bars of the "z" axis. The height range for sample A3 is in tens of nanometers (from −71 to 22 nm), whereas for the sample A4, it is at micrometers (from - 1342–600 nm), which makes it approximately

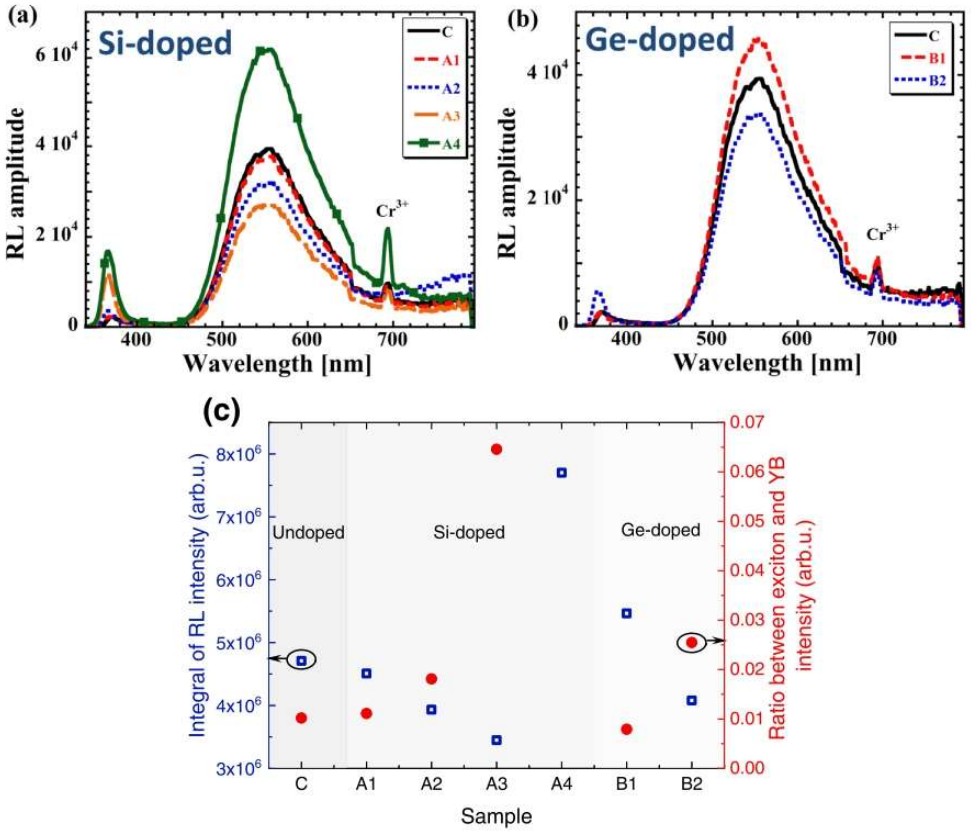

Fig. 4. Room-temperature RL spectra (40 kV, 15 mA) of (a) Si-doped samples and (b) Ge-doped samples. (c) the integrals of RL intensities over the whole spectrum and exciton/YB ratios.

20 times rougher. In the case of Ge doping, we confirmed the previously published results [27,28] that even for a high concentration of Ge, it is possible to obtain a smooth surface. We could not try to grow samples with higher Ge concentration (in the order of 10^{20} cm^{-3}) due to technological issues connected with the Ge incorporation rate, which is almost two orders of magnitude lower than Si at the high temperature used for high-quality GaN growth [11]. Nevertheless, we confirm maintaining of the smooth surface of the Ge-doped sample B2 with the dopant concentration 4.3×10^{18} cm^{-3}, see Fig. 6f. Interestingly, V-pits are larger here than on the A3 sample with the higher Si doping concentration, and their density is lower (note the different scales of the pictures as well). Since the smooth surface is beneficial for subsequent growth of InGaN/GaN MQWs used as the active region of LEDs or scintillators and also for applications requiring the wave-guiding layer, the Ge doping might be a superior n-type dopant.

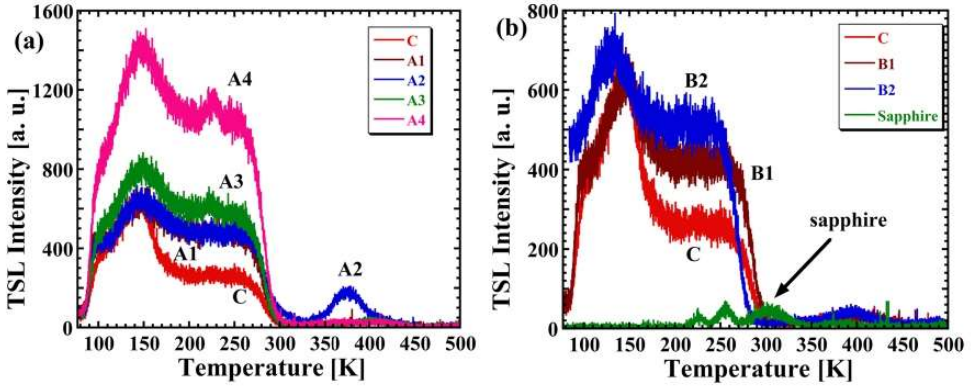

Fig. 5. TSL glow curves of (a) undoped GaN and Si-doped GaN samples, (b) Ge-doped GaN samples and sapphire substrate after the X-ray irradiation at 77 K.

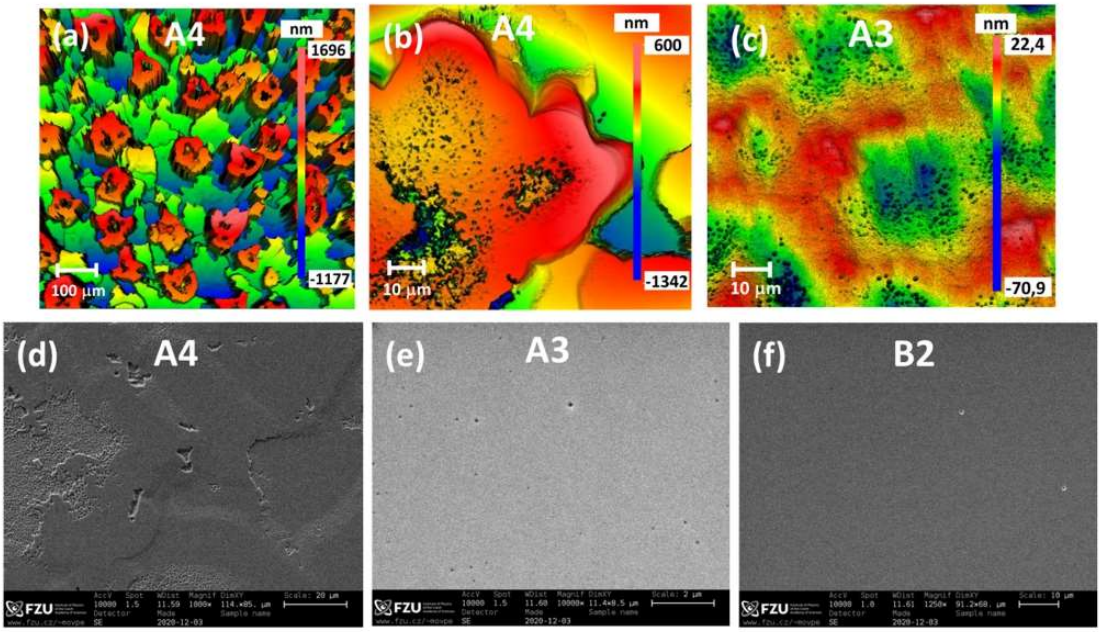

Fig. 6. Comparison of surface morphologies of Si-doped samples A4 and A3 with Ge-doped sample B2 by WLI (a - c) and SEM (d - f). Dopant concentrations 1.5×10^{19} cm^{-3}, 1.1×10^{19} cm^{-3}, and 4.3×10^{18} cm^{-3} respectively.

To describe recombination mechanisms in semiconductors, rate equations are often used [31,32], sometimes simplified to the ABC model [33,34]. Rate equations in the case of n-type GaN at time $t = 0$ after pulse generation can be written as:

$$\begin{aligned}\frac{dn}{dt} &= -B\,n\,p - C_{nD} n\,(N_D - N_D^0) - C_{nA} n\,N_A^0 - C_{nS} n\,(N_S - N_S^0)\frac{dN_D^0}{dt} \\ &= C_{nD} n\,(N_D - N_D^0) - C_{DA}\,(N_D^0\,N_A^0)\frac{dN_A^0}{dt} \\ &= C_{pA} p\,(N_A - N_A^0) - C_{DA}\,(N_D^0\,N_A^0) - C_{nA} n\,N_A^0\frac{dN_S^0}{dt} \\ &= C_{nS} n\,(N_s - N_S^0) - C_{pS} p\,N_S^0,\end{aligned} \tag{3}$$

where $n = n_0 + \Delta n$ is the electron concentration consisting of the equilibrium concentration n_0 and concentration of excited electrons Δn. $p = \Delta p$ is the hole concentration which is equal to the non-equilibrium one in the n-type widegap semiconductor at room temperature. N_D, N_A, and N_s are concentrations of donors, acceptors, and non-radiative traps, respectively, and superscript 0 indicate their charge-neutral state. Coefficients C_{nD}, C_{nS} describe a process when the electron is captured by donor and non-radiative center, respectively. Similarly, C_{pA} and C_{pS} are coefficients of hole capture by acceptor and non-radiative center. Finally, C_{DA} is the coefficient of radiative donor-acceptor pair recombination and C_{nA} describes radiative recombination by e-A^0 transition. Charge neutrality condition must also be fulfilled:

$$n + (N_A - N_A^0) = p + (N_s - N_S^0) + (N_D - N_D^0) \tag{4}$$

The increasing intensity ratio between exciton and yellow bands (Fig. 4c) can be understood by the above equations. Since acceptor concentration responsible for the YB is limited in the samples, an increase of n_0 will not lead to enhanced recombination via this channel. On the other hand, the density of exciton or electron and hole states is large, and the recombination probability is increased with larger n_0. Fitting of time-resolved luminescence is possible by solving the system (3) and (4) numerically when initial concentrations at time $t = 0$ are known. However, the large number of free parameters decreases the reliability of the fits. Therefore, the mean decay time obtained from the three-exponential fit is used in further discussion.

In the low-excitation density regime, which is relevant for our experiments given the excitation power of 1 pJ in 1 ns pulse, equilibrium electron concentration is much larger than the non-equilibrium one ($n_0 \gg \Delta n$) which leads to simple dependence of e-A^0 recombination lifetime on n_0 [19]:

$$\tau_{eA} = \frac{1}{C_{nA}\,n_0} \Rightarrow n_0 = \frac{1}{C_{nA}\,\tau_{eA}}, \tag{5}$$

For donor-acceptor recombination, recombination probability depends on mutual distance between donors and acceptors [27]. Therefore, the term $C_{DA}\,(N_D^0\,N_A^0)$ does not properly describe the DAP mechanism, although it is sometimes used [31]. Si or Ge atoms are mostly incorporated into the crystal lattice of GaN as shallow substitutional donors on the Ga site [35] with ionization energies around 30 meV for both Si_{Ga} and Ge_{Ga} [12]. Radiative recombination rate $W(R)$ of an electron bound to a donor and hole caught up in an acceptor (probably C_N related defect in our case) depends exponentially on their mutual distance R by the equation [36]:

$$W(R) = W_{max}\,e^{-\frac{2R}{a_D}}. \tag{6}$$

The a_D is the Bohr radius of the weakly bound particle, which is the electron. Bohr radiuses calculated as:

$$a_{D,A} = \frac{\hbar}{\sqrt{2m^*\,E_A}}, \tag{7}$$

are listed in Table 2 together with the activation energies of related defects. The m^* is the effective mass of the electron or hole (m_e = 0.22 m_0 or m_h = 0.8 m_0, m_0 being the free-electron mass) [37,38], and the E_A is the donor or acceptor activation energy, respectively.

The W_{max} is the maximum recombination rate of DAP transition in the mass approximation when $R \to 0$. Its value for YB in GaN was found to be $1.6 \cdot 10^6$ s^{-1} [39], $2.5 \cdot 10^7$ s^{-1} [40] but also much larger

Table 2
Activation energy and Bohr radius of incorporated dopants.

Defect	E_a [meV]	a_D, a_A [Å]
Si_{Ga}	30.8	28.7
Ge_{Ga}	31.1	28.6

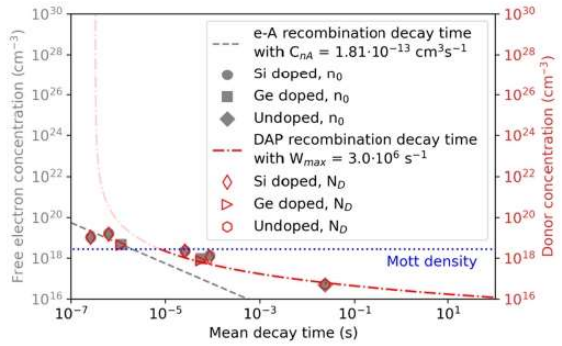

Fig. 7. Inverse dependence of mean decay time on donor concentration or free electron concentration. The dashed line was calculated by Eq. (5) and dashed-dotted one with Eq. (9) with parameters $C_{nA} = 1.81\,10^{-13}$ cm^{3}s^{-1} and $W_{max} = 3\,10^6$ s^{-1}.

value was reported [41]. The radiative recombination rate W determines basically the bound hole lifetime by dependence $W = \tau^{-1}$ [19], which is also the luminescence decay time in the n-type semiconductor. If we assume the dependence of the average distance between donor and acceptor on the concentration of neutral donors N_D^0 as:

$$\frac{4}{3}\pi R_{DAP}^3 = V = \frac{1}{N_D^0}, \tag{8}$$

we can obtain an expression for the average decay time of donor-acceptor recombination:

$$\frac{1}{\tau_{DAP}} = W(R) = W_{max}\, e^{-\frac{2}{a_D}\left(\frac{3}{4\pi N_D^0}\right)^{\frac{1}{3}}} \Rightarrow N_D^0 = \frac{3}{4\pi\left[\frac{a_D}{2}\ln(W_{max}\tau_{DAP})\right]^3}. \tag{9}$$

Fig. 7 shows the inverse dependence of the mean lifetime of the samples under study (see also Table 1) on the concentration of donors obtained from SIMS measurement and free electron concentration obtained by transport measurement (Table 1). Dashed and dotted lines are calculated using Eqs. (5) and (9), respectively, with parameters $C_{nA} = 1.8\,10^{-13}$ cm^{3}s^{-1} and $W_{max} = 3\,10^6$ s^{-1}. Note that the value of W_{max} fits the one in [39] and C_{nA} corresponds very well to the value obtained by Reshchikov for center responsible for YB [32]. Ionization energies for both Si and Ge donors were taken the same $E_A = 30$ meV.

The dependencies in Fig. 7. suggest that DAP recombination dominates for samples with low Si or Ge concentration. However, the shallow donor level widens with the increasing donor concentration, and the gap between donor level and conduction band becomes smeared. It leads to the replacement of DAP recombination with the e-A^0 mechanism because above Mott densities ($2.8\,10^{18}$ cm^{-3} [42]), the DAP recombination cannot be the dominant recombination mechanism, which is indicated by the transparent line.

4. Conclusion

We have investigated the luminescence and morphological properties of Si and Ge doped GaN layers. Based on our discussion, the DAP transition at low and mid-levels of donor concentration and e-A^0 at higher donor concentration explain the astonishing acceleration of the PL decay times with the increasing dopant concentration from *ms* order of magnitude to the *ns* range. Moreover, we have confirmed by TSL measurement the similar origin of the luminescence transition even for the undoped sample, in which an unintentional shallow donor (probably Si) causes the DAP transition. We also observed an increased probability of non-radiative recombination with higher donor concentration from RL spectra.

The sample A4 had a significantly higher luminescence intensity in both RL and TSL spectra compared to other samples. We explained this phenomenon by a rough surface morphology created after exceeding the critical Si-doping concentration. The formed 3D structure, observed by SEM and WLI methods, causes enhanced light extraction from the GaN layer. Technologically controlled acceleration of YB luminescence brings an unconventional solution for the traditional problem of slow GaN YB luminescence, which has a promising potential in future GaN-based applications.

CRediT authorship contribution statement

Tomáš Vaněk: Conceptualization, Investigation, Data curation, Writing – original draft. **František Hájek**: Conceptualization, Investigation, Data curation, Writing – review & editing. **Vítězslav Jarý**: Conceptualization, Investigation, Writing – review & editing. **Tomáš Hubáček**: Investigation, Writing – review & editing. **Karla Kuldová**: Investigation, Writing – review & editing. **Zuzana Gedeonová**: Investigation, Writing – review & editing. **Zdeněk Remeš**: Investigation, Writing – review & editing. **Vladimír Babin**: Investigation, Writing – review & editing. **Maksym Buryi**: Conceptualization, Writing – review & editing, Supervision.

Declaration of Competing Interest

The authors declare that they have no known competing financial interests or personal relationships that could have appeared to influence the work reported in this paper.

Acknowledgment

This work was supported by the Czech Science Foundation by project No. 20-05497Y, the Ministry of Education, Youth and Sports of Czech Republic under project No. SOLID21 CZ.02.1.01/0.0/0.0/16_019/0000760.

Appendix A. Supporting information

Supplementary data associated with this article can be found in the online version at doi:10.1016/j.jallcom.2022.165255.

References

[1] S. Nakamura, M. Senoh, T. Mukai, P-GaN/N-InGaN/N-GaN double-heterostructure blue-light-emitting diodes, Jpn. J. Appl. Phys. 32 (1993) L8.
[2] S. Nakamura, S. Pearton, G. Fasol, The Blue Laser Diode, Springer Berlin Heidelberg, Berlin, Heidelberg, 2000.
[3] F. Roccaforte, P. Fiorenza, G. Greco, R.L. Nigro, F. Giannazzo, A. Patti, M. Saggio, Challenges for energy efficient wide band gap semiconductor power devices, Phys. Status Solidi A 211 (2014) 2063–2071.
[4] O. Jani, I. Ferguson, C. Honsberg, S. Kurtz, Design and characterization of GaN/InGaN solar cells, Appl. Phys. Lett. 91 (2007) 132117.
[5] Y. Ren, Z. He, B. Dong, C. Wang, Z. Zeng, Q. Li, Z. Chen, L. Li, N. Liu, Analysis of electrical properties in Ni/GaN schottky contacts on nonpolar/semipolar GaN free-standing substrates, J. Alloy. Compd. (2021) 162817.
[6] A. Dash, A. Sharma, S.K. Jain, B.S.K. Patra, A. Gundimeda, S. Mallik, G. Gupta, Influence of current conduction paths and native defects on gas sensing properties of polar and non-polar GaN, J. Alloy. Compd. (2021) 162808.
[7] F. Roccaforte, P. Fiorenza, G. Greco, R. Lo Nigro, F. Giannazzo, F. Iucolano, M. Saggio, Emerging trends in wide band gap semiconductors (SiC and GaN) technology for power devices, Microelectron. Eng. 187–188 (2018) 66–77.
[8] T. Hubáček, A. Hospodková, K. Kuldová, J. Oswald, J. Pangrác, V. Jarý, F. Dominec, M.S. Zíková, F. Hájek, E. Hulicius, A. Vetushka, G. Ledoux, C. Dujardin, M. Nikl, Advancement toward ultra-thick and bright InGaN/GaN structures with a high number of QWs, CrystEngComm 21 (2019) 356–362.

[9] D.-Y. Shin, T. Kim, O. Akyuz, H.V. Demir, I.-H. Lee, Ag@SiO2-embedded InGaN/GaN nanorod array white light-emitting diode with perovskite nanocrystal films, J. Alloy. Compd. (2021) 162974.

[10] N. Koide, H. Kato, M. Sassa, S. Yamasaki, K. Manabe, M. Hashimoto, H. Amano, K. Hiramatsu, I. Akasaki, Doping of GaN with Si and properties of blue m/i/n/n+ GaN LED with Si-doped n+-layer by MOVPE, J. Cryst. Growth 115 (1991) 639–642.

[11] S. Nakamura, T.M.T. Mukai, M.S.M. Senoh, Si- and Ge-doped GaN films grown with GaN buffer layers, Jpn. J. Appl. Phys. 31 (1992) 2883.

[12] H. Wang, A.-B. Chen, Calculation of shallow donor levels in GaN, J. Appl. Phys. 87 (2000) 7859–7863.

[13] P. Pittet, G.-N. Lu, J.-M. Galvan, J.-M. Bluet, I. Anas, J.-Y. Giraud, J. Balosso, PL characterization of GaN scintillator for radioluminescence-based dosimetry, Opt. Mater. 31 (2009) 1421–1424.

[14] U. Kaufmann, M. Kunzer, H. Obloh, M. Maier, C. Manz, A. Ramakrishnan, B. Santic, Origin of defect-related photoluminescence bands in doped and nominally undoped GaN, Phys. Rev. B. 59 (1999) 5561–5567.

[15] S.T. Liu, J. Yang, D.G. Zhao, D.S. Jiang, F. Liang, P. Chen, J.J. Zhu, Z.S. Liu, W. Liu, Y. Xing, L.Q. Zhang, M. Li, The compensation role of deep defects in the electric properties of lightly Si-doped GaN, J. Alloy. Compd. 773 (2019) 1182–1186.

[16] A. Hospodková, M. Nikl, O. Pacherová, J. Oswald, P. Brůža, D. Pánek, B. Foltynski, E. Hulicius, A. Beitlerová, M. Heuken, InGaN/GaN multiple quantum well for fast scintillation application: radioluminescence and photoluminescence study, Nanotechnology 25 (2014) 455501.

[17] T. Hubáček, A. Hospodková, K. Kuldová, M. Slavická Zíková, J. Pangrác, J. Čížek, M.O. Liedke, M. Butterilng, A. Wagner, P. Hubík, E. Hulicius, Improvement of luminescence properties of n-GaN using TEGa precursor, J. Cryst. Growth 531 (2020) 125383.

[18] D.C. Look, R.J. Molnar, Degenerate layer at GaN/sapphire interface: influence on Hall-effect measurements, Appl. Phys. Lett. 70 (1997) 3377–3379.

[19] M.A. Reshchikov, H. Morkoç, Luminescence properties of defects in GaN, J. Appl. Phys. 97 (2005) 61301.

[20] F. Liang, D. Zhao, D. Jiang, Z. Liu, J. Zhu, P. Chen, J. Yang, S. Liu, Y. Xing, L. Zhang, Role of Si and C impurities in yellow and blue luminescence of unintentionally and Si-doped GaN, Nanomaterials 8 (2018).

[21] H.H. Kusuma, B. Astuti, Z. Ibrahim, Absorption and emission properties of ruby (Cr:Al2O3) single crystal, J. Phys. Conf. Ser. 1170 (2019) 12054.

[22] S.W.S. McKeever, Thermoluminescence of Solids, first ed, Cambridge University Press, 1985.

[23] R. Czernecki, E. Grzanka, R. Jakiela, S. Grzanka, C. Skierbiszewski, H. Turski, P. Perlin, T. Suski, K. Donimirski, M. Leszczynski, Hydrogen diffusion in GaN:Mg and GaN:Si, J. Alloy. Compd. 747 (2018) 354–358.

[24] T. Vaněk, T. Hubáček, F. Hájek, F. Dominec, J. Pangrác, K. Kuldová, J. Oswald, A. Hospodková, Nanostructured layer enhancing light extraction from GaN-based scintillator using MOVPE, 2020, pp. 12–17.

[25] J. Xie, S. Mita, A. Rice, J. Tweedie, L. Hussey, R. Collazo, Z. Sitar, Strain in Si doped GaN and the Fermi level effect, Appl. Phys. Lett. 98 (2011) 202101.

[26] S. Tanaka, S. Iwai, Y. Aoyagi, Self-assembling GaN quantum dots on $Al_xGa_{1-x}N$ surfaces using a surfactant, Appl. Phys. Lett. 69 (1996) 4096–4098.

[27] H. Lahrèche, P. Vennéguès, B. Beaumont, P. Gibart, Growth of high-quality GaN by low-pressure metal-organic vapour phase epitaxy (LP-MOVPE) from 3D islands and lateral overgrowth, J. Cryst. Growth 205 (1999) 245–252.

[28] A. Hospodková, M.S. Zíková, T. Hubáček, J. Pangrác, K. Kuldová, F. Hájek, F. Dominec, A. Vetushka, S. Hasenöhrl, Improvement of GaN crystalline quality by SiNx layer grown by MOVPE, Lith. J. Phys. 59 (2019).

[29] K. Forghani, L. Schade, U.T. Schwarz, F. Lipski, O. Klein, U. Kaiser, F. Scholz, Strain and defects in Si-doped (Al)GaN epitaxial layers, J. Appl. Phys. 112 (2012) 93102.

[30] P. Chauhan, R. Mohamad, InAl(Ga)N: MOCVD thermodynamics and strain distribution, J. Alloy. Compd. 892 (2022) 162123.

[31] C. Spindler, T. Galvani, L. Wirtz, G. Rey, S. Siebentritt, Excitation-intensity dependence of shallow and deep-level photoluminescence transitions in semiconductors, J. Appl. Phys. 126 (2019) 175703.

[32] M.A. Reshchikov, Measurement and analysis of photoluminescence in GaN, J. Appl. Phys. 129 (2021) 121101.

[33] A. Kiligaridis, P.A. Frantsuzov, A. Yangui, S. Seth, J. Li, Q. An, Y. Vaynzof, I.G. Scheblykin, Are Shockley-Read-Hall and ABC models valid for lead halide perovskites? Nat. Commun. 12 (2021) 1–13.

[34] M.A. Hopkins, D.W.E. Allsopp, M.J. Kappers, R.A. Oliver, C.J. Humphreys, The ABC model of recombination reinterpreted: Impact on understanding carrier transport and efficiency droop in InGaN/GaN light emitting diodes, J. Appl. Phys. 122 (2017) 234505.

[35] M. Matsubara, E. Bellotti, A first-principles study of carbon-related energy levels in GaN. II. Complexes formed by carbon and hydrogen, silicon or oxygen, J. Appl. Phys. 121 (2017) 195702.

[36] D.G. Thomas, J.J. Hopfield, W.M. Augustyniak, Kinetics of radiative recombination at randomly distributed donors and acceptors, Phys. Rev. 140 (1965) A202–A220.

[37] W.J. Moore, J.A. Freitas, S.K. Lee, S.S. Park, J.Y. Han, Magneto-optical studies of free-standing hydride-vapor-phase epitaxial GaN, Phys. Rev. B. 65 (2002) 81201.

[38] J.I. Pankove, S. Bloom, G. Harbeke, Optical properties of GaN, RCA Rev. 36 (1975) 163.

[39] R.Y. Korotkov, M.A. Reshchikov, B.W. Wessels, Transient photoluminescence of defects in undoped GaN prepared by metal organic vapor phase epitaxy, Phys. B Condens. Matter 273–274 (1999) 80–83.

[40] D.M. Hofmann, D. Kovalev, G. Steude, B.K. Meyer, A. Hoffmann, L. Eckey, R. Heitz, T. Detchprom, H. Amano, I. Akasaki, Properties of the yellow luminescence in undoped GaN epitaxial layers, Phys. Rev. B. 52 (1995) 16702–16706.

[41] M.A. Reshchikov, H. Morkoç, S.S. Park, K.Y. Lee, Transient photoluminescence of defect transitions in freestanding GaN, Appl. Phys. Lett. 78 (2001) 2882–2884.

[42] F. Binet, J.Y. Duboz, J. Off, F. Scholz, High-excitation photoluminescence in GaN: hot-carrier effects and the Mott transition, Phys. Rev. B 60 (1999) 4715–4722.

Journal of Luminescence 236 (2021) 118127

Contents lists available at ScienceDirect

Journal of Luminescence

journal homepage: http://www.elsevier.com/locate/jlumin

Full Length Article

Depth profile of acceptor concentration in InGaN/GaN multiple quantum wells

F. Hájek [a,b,*], A. Hospodková [a], T. Hubáček [a], J. Oswald [a], J. Pangrác [a], F. Dominec [a], R. Horešovský [a,b], K. Kuldová [a]

[a] Institute of Physics CAS, v.v.i., Cukrovarnická 10, CZ-16200, Prague 6, Czech Republic
[b] Faculty of Faculty of Nuclear Sciences and Physical Engineering, Czech Technical University in Prague, Břehová 7, CZ-11519 ,Praha 1, Czech Republic

ARTICLE INFO

Keywords:
Nitrides
Impurity
SIMS
InGaN/GaN

ABSTRACT

Zn contamination of InGaN/GaN multiple quantum well (MQW) structure from unknown source is found. A model describing concentration profile of Zn acceptor impurity in InGaN/GaN MQW structure is introduced and compared to measured values. The model is based on difference among the formation energies of acceptors in the InGaN quantum wells. A nice correlation of the model and experimental data helps to reveal origin of Zn impurity in InGaN quantum wells. Proposed methodology can be applied to different acceptor-like defects and shine light the upon enigma of high defect concentration in the bottom quantum wells grown atop the n-type buffer layer.

1. Introduction

InGaN/GaN heterostructures are commonly used for highly efficient light emitting diodes (LEDs) or lasers. However, the development of these structures has been accompanied by several tricks which were necessary to obtain internal quantum efficiency as high as 80% at room temperature (RT) [1].

Point defects are usually presented in conventional *c*-plane InGaN QWs. These can act as defect luminescence centers or non-radiative centers. For LED application, n-type doping of buffer layers is usually performed which favors acceptor-like defects formation in QWs. From the photoluminescence (PL) results, it was found that luminescence intensity of defect bands is reduced in the top QWs (QWs close to p-side of the LED structure) or QWs upon InGaN/GaN superlattices [2,3] compared to the bottom QWs. If the impurity concentration is not high enough to quench luminescence, monotonic increase in defect luminescence intensity can be expected with higher defect concentration.

One of the best documented (both theoretically and experimentally) deep acceptors in GaN is Zn_{Ga} [4–7]. It is a common impurity presented in GaN films with typical luminescence band around 2.9 eV at room temperature [4,5]. Concentration quenching of the blue luminescence band related to Zn acceptor in GaN was reported at concentration about 9×10^{18} cm^{-3} [8]. Zn doped InGaN QWs were studied as promising candidates for active region in white LEDs [9,10].

In this paper, high Zn impurity concentration in the first InGaN QW is discussed in terms of acceptor formation energy. Concentration depth profile of Zn impurity is studied by Secondary Ion Mass Spectroscopy (SIMS) and model is developed to explain measured data. The model can be applied to different acceptor-like defects and help to understand the impurity distribution in the structures.

2. Experimental

All the samples referred in this work were grown on the Aixtron 3×2 CCS MOVPE system equipped with LayTec EpiCurveTT apparatus for in situ measurement of reflectivity, curvature and true wafer temperature. Sapphire substrates with *c*-plane orientation were used for the growths. Buffer layers were grown with trimethylgallium (TMGa) and ammonia (NH_3) precursors with a hydrogen carrier gas. Top 200 nm of GaN buffer layers were doped with silicon (concentration 3×10^{18} cm^{-3}). Additional details can be found elsewhere [11]. The precursors during active region growth were NH_3, triethylgallium (TEGa) and trimethylindium (TMIn) as sources for N, Ga and In respectively. Nitrogen carrier gas was used for active region growth. Studied structures contain stack of 5 QWs and barriers, GaN separation layer and second stack of 5 QWs and barriers. The structure is capped with GaN layer. Schematic diagram is

* Corresponding author. Faculty of Faculty of Nuclear Sciences and Physical Engineering, Czech Technical University in Prague, Břehová 7, CZ-11519 Praha 1, Czech Republic.
E-mail address: hajek@fzu.cz (F. Hájek).

https://doi.org/10.1016/j.jlumin.2021.118127
Received 22 February 2021; Received in revised form 29 March 2021; Accepted 10 April 2021
Available online 12 April 2021

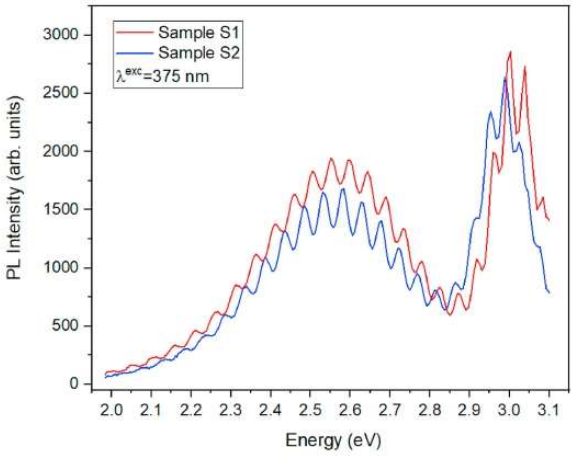

Fig. 1. PL spectra of samples S1 and S2. Peak around 410 nm is assigned to recombination of excitons and trapped carriers in QWs states and the low-energy peak to electrons in QWs and Zn acceptor recombination.

shown in Fig. 2a.

Room-temperature photoluminescence (PL) measurements were performed with $\lambda^{exc} = 375$ nm laser diode excitation with maximal intensity 10 Wcm^{-2}. Luminescence was gathered by elliptical mirror and focused on the entrance slit of double-grating monochromator SDL-1. GaAs photomultiplier was used and the measurements were carried out in lock-in setup. Because of the below GaN-bandgap excitation energy, only a small portion of excitation light was absorbed in the sample (mainly in QWs).

SIMS measurements were carried out in EAG laboratories. Measured elements included Ga, N, In, Si, C, O and Zn. Simulations of the band structure were carried out in Nextnano^{++} software by solving 1D Schrödinger and Poisson equations self-consistently [12].

3. Results and discussion

PL spectra of sample S1 and S2 are shown in Fig. 1. Peak centered around 3.05 eV is assigned to recombination of exciton and trapped carriers in QWs (QW peak) [13]. The low energy peak is caused by recombination of electron in QW confined state and hole bound at Zn acceptor [9,10]. Further proofs of assigning the origin of the low energy peak to transition connected with Zn acceptor can be found in Supplementary materials, section 1. Oscillations superimposed on the two peaks are caused by interference (GaN and InGaN layers sandwiched between the sapphire substrate and air shows resonator-like behavior). If spectra are properly transformed to wavevector domain, the interference pattern can be easily eliminated by means of Fourier transform.

Because in many applications (like LEDs or scintillators) the luminesce peaks except the main QW peak are considered parasitic, the sources of defects responsible for the parasitic luminescence peak are of great interest. Since unintentionally doped GaN is n-type semiconductor, luminescence centers (including Zn) are usually of acceptor nature. Model introduced in the next paragraphs helps to reveal the source of the impurity and can be applied to different acceptor-like defects.

SIMS profile of a sample with 10 QWs is shown in Fig. 2b. Indium signal serves as QW marker, high Si signal indicates the n-type region grown from TMGa. Carbon concentration (not shown here) is around 3 $\times 10^{16}$ cm^{-3} in the active region, so the main acceptor in our samples is assumed to be Zn_{Ga} in the active region. Samples S1 and S2 are identical except the thickness of the GaN capping layer and purity of TMIn source (sample S2 has thinner GaN cap and is grown from high-purity TMIn). From SIMS results, the highest Zn concentration is inside the first QW (i.e. QW close to n-GaN buffer layer) and decreases in the next four QWs of the first stack. At the beginning of the next QWs stack, the situation is similar but with lower starting Zn concentration. The Zn signal in the top QWs is disturbed by the surface contamination of V-pits penetrating through upper QW region in sample S2 with thin GaN capping, as is commonly observed (for example in Ref. [14]). Transmission electron microscope image of sample S1 is shown in Supplementary materials, section 2 (Fig. 3S). It can be seen that final V pits penetrate to the region above the second QWs stack. Therefore, the SIMS measurement on sample S1 is disturbed by impurity adsorption of V pit surface only in the GaN capping region, but not in the QWs themselves. Effect of V pits on luminescence properties of the samples is discussed in detail in Ref. [13].

Zn distribution in QWs is very unusual (especially interesting is the increase of Zn concentration in the sixth QW). To understand it, the model based on formation energy dependence was developed. Very important factor is the n-type doping due to Si donors under the active area, widely used during LEDs growth. Si doping shifts the Fermi level towards the conduction band of heterostructure and lowers the formation energy E_{for} of acceptor impurity, such as Zn_{Ga}. The concentration of defects C_{def} can be theoretically estimated as [15]:

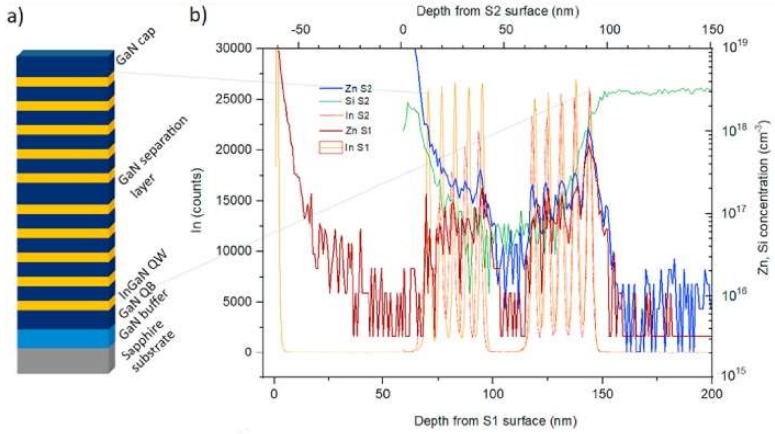

Fig. 2. a) Schematic diagram of the structure, b) SIMS profile of sample S1 and S2. Indium signal serves as the QWs marker. Drop in Si signal represents the border between region grown from TMGa and TEGa. Zn impurity concentration profile is unusual and can be seen for both samples S1 and S2.

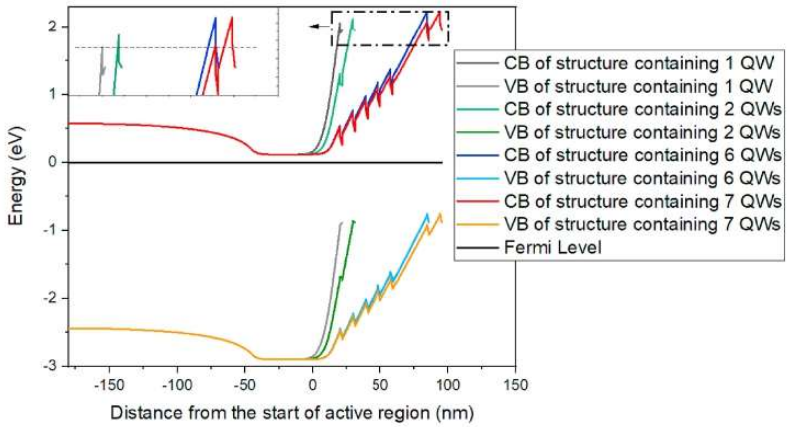

Fig. 3. Band profiles (VB = valence band, CB = conduction band) of the structure containing 1, 2, 6 and 7 QWs. The inset shows different poisitons of CB relative to Fermi level for these QWs in detail. The position of CB in the QW in the structure with one QW is the closest to Fermi level position so the formation energy of Zn acceptors is the smallest. The dashed line in the inset shows CB energy at start of the seventh QW growth (in structure with 7 QWs in total) to guide the eye.

$$C_{def} = N_s \exp\left(-\frac{E_{for}}{kT}\right), \tag{1}$$

where N_S is the site concentration for the defect and k is the Boltzmann constant [15]. The dependence of Zn_{Ga} formation energy on Fermi level position for GaN was taken from Ref. [4]. Because no data are available for InGaN, the E_{for} values for GaN from Ref. [4] were used and calibrated to keep the Fermi level to bandgap ratio the same according to the relationship $E_{for} = -1.194 \times E_F + 3.6$, where E_F is the Fermi level position.

In ref. [16] it is shown that surface of the sample during the growth can act as a reservoir of different defects (in this case, Zn atoms). The Zn impurity originates in some precursor or carrier gas, adsorbs on the surface, but incorporation probability into the layer is dependent on formation energy Zn_{Ga}. If the probability of Zn incorporation is low Zn atoms remain in the surface reservoir.

In the case when impurities are not available in the whole growth but there is some kind of reservoir, impurity concentration in N-th InGaN layer can be calculated as [16].

$$C_{def} = C_0 R^N, \tag{2}$$

where C_0 is the initial concentration, R is the segregation coefficient and N is the number of InGaN layers where impurities segregate [16]. If the impurity comes from reservoir which is filled during growth, the C_0 can be assumed proportional to thickness of layers grown from the gas phase containing the impurity, d_r

$$C_0 = \beta \times d_r. \tag{3}$$

β is the proportionality constant. If the reservoir is refilled during the active region growth (for example impurity comes from TEGa), the impurity concentration profile can be finally simulated by

$$C(x) = (\beta \times d_r - C_{inc}(x)) \times \delta(x - x_{QW}) \times \frac{\exp\left(-\frac{E_{for}(x)}{kT}\right)}{\exp\left(-\frac{E_{for}(a)}{kT}\right)} \times R^{N(x)}, \tag{4}$$

where a is the x position of the start of the first QW (which was considered to be 2 nm thick, simulation step is 1 nm), x_{QW} is the start position of a QW, $N(x)$ is the number of InGaN layers grown from start to x position and C_{inc} is the concentration incorporated between origin and x position, defined as

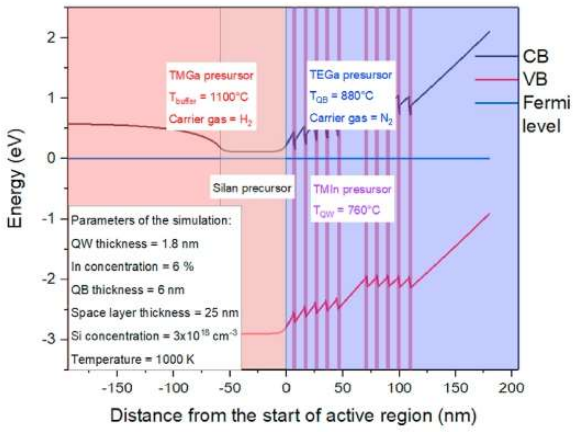

Fig. 4. Simulation of band edges of the final structure. Parameters of the simulation are indicated in the left bottom frame. Other labels indicate the growth conditions for particular regions, but they are not treated as variables for nextnano simulation except doping.

$$C_{inc}(x) = \frac{\int_0^{x-a} C(t)dt}{x-a}. \tag{5}$$

Important fact is that if the reservoir is refilled during QB growth, Zn concentration in reservoir will substantially increase while growing 25 nm thick separation layer between first five QWs and the sixth QW if the formation energies are comparable between the fifth and the sixth QW.

Band structure was simulated in steps beginning with the GaN buffer only and then at every other step one pair of barrier and QW was added, so the changes in conduction/valence band position with respect to Fermi level can be monitored for different QWs (imitation of the growth process). This procedure was done up to 10 QWs.

Band profiles of structures containing 1, 2, 6 and 7 grown QWs are shown in Fig. 3. N-type doping of the buffer layer along with the piezoelectric field is responsible for different formation energies of defects in QWs.

An important yet unknown variable is the surface potential of the sample during the growth. It affects absolute values of conduction band

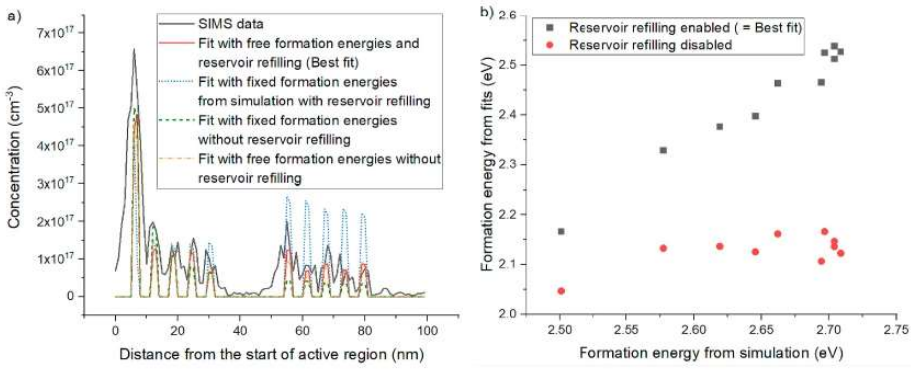

Fig. 5. a) Zn concentration from SIMS and fits according to eq. (4). SIMS data are from sample S1. The origin is set to start of TEGa growth (in contrast to Fig. 1, which has origin at the surface). b) Comparison of formation energies from nextnano simulation and fit with eq. (4) with enabled or disabled reservoir refilling.

offset from Fermi level and consequently, the formation energy. The simulations were conducted for different surface potentials. However, the obtained relative formation energies did not differ much for potential values which can be expected for n-type semiconductor with high surface defect density. The band edges of the whole structure are shown in Fig. 4.

From the formation energies obtained from combination of Nextnano^{++} simulations and Fermi level dependence from Ref. [4], the Zn concentrations were fitted by eq. (4) to SIMS values of sample S1 with fitting parameters R and β (Fig. 5a).

Up to now, simulations were performed with refilling the Zn reservoir during active region growth. To test whether refilling of the reservoir is important, attempts were made to simulate Zn concentrations in case the reservoir is not being refilled, which would happen if the source of Zn was for example TMGa. However, it was not possible to obtain the specific feature of the concentration profile - the increase of Zn concentration in the sixth QW - with the formation energies obtained from nextnano simulation. When the formation energies were used as free parameter during fitting procedure, quite good fit of SIMS data with eq. (4) could be obtained but the fitted formation energies clearly disagree with those obtained by nextnano simulation (Fig. 5b). Therefore, the assumption of not refilling the reservoir is most likely wrong.

Solution of eq. (4) was also obtained for fitting the formation energies as free parameter with reservoir refilling (marked as Best fit). Fit results are also shown in Fig. 5a. Best fit results are in nice coincidence with measured concentration profile. Fit with formation energies from Nextnano simulation provides the characteristic Zn concentration increase in the sixth QW, but the concentration is too large. The formation energies obtained from Best fit are compared to those from Nextnano simulation in Fig. 5b.

Linear dependence in Fig. 5b for Best fit energies is evident, suggesting the meaningfulness of the fitted values. The difference between absolute value of the fitted formation energies and those obtained from simulation may arise dominantly from the unknown value of surface potential or other acceptor-like defects not included in the model.

From the simulation and fitting results, it is highly probable that Zn contamination comes from the source which can refill the Zn reservoir during the growth of the active region, but also during the separation layer. TMIn can be ruled out because it is not used during the separation layer growth. Moreover, changing TMIn precursor for the high-purity one (sample S2) did not affect Zn concentration. Therefore, the most probable candidates are TEGa, N_2 or NH_3. On the other hand, it seems very unlikely that the Zn contamination originates from TMGa, SiH_4 or hydrogen which is used as the carrier gas before active area growth. The approach demonstrated above can be applied to different acceptor-like defects commonly presented in InGaN/GaN QWs and help to elucidate their origin.

4. Conclusion

To summarize, the unexpected Zn impurity profile was obtained by SIMS analysis in InGaN/GaN QWs. Model based on different formation energies in QWs was proposed to explain observed dependences. According to the simulation results, Zn contamination comes most probably from TEGa precursor (supplier claims Zn contamination of TEGa used for both samples under study to be 0.2 ppm at most). Described method can be generalized on other acceptor-like defects in InGaN QWs grown on n-type GaN buffer and can help to understand the impurity distribution in the structure.

5. Supplementary materials

See the supplementary materials for more details about Zn related luminescence band and for transmission electron microscope image of V pits in sample S1.

Declaration of competing interest

The authors declare that they have no known competing financial interests or personal relationships that could have appeared to influence the work reported in this paper.

Acknowledgments

Partial support of the Operational Programme Research, Development and Education financed by European Structural and Investment Funds and the Czech Ministry of Education, Youth and Sports (Project No. SOLID21 CZ.02.1.01/0.0/0.0/16_019/0000760) and support of TACR project FW03010298 are aknowledged.

The authors would also like show gratitude to Philomela Komninou, Aristotle University of Thessaloniki, Thessaloniki, Greece for transmission electron measurements.

Appendix A. Supplementary data

Supplementary data to this article can be found online at https://doi.org/10.1016/j.jlumin.2021.118127.

Author statement

František Hájek: Conceptualization, Methodology, Software, Writing – original draft. Alice Hospodková: Writing – review & editing,

Investigation, Funding acquisition. Tomáš Hubáček: Resources, Investigation. Jiří Oswald: Investigation, Resources. Jiří Pangrác: Resources. Filip Dominec: Software. Robert Horešovský: Software. Karla Kuldová: Resources.

7. Data availability

The data that support the findings of this study are available from the corresponding author upon reasonable request.

References

[1] Idris A. Ajia, et al., Generated carrier dynamics in V-pit-enhanced InGaN/GaN light-emitting diode, ACS Photonics 5 (3) (2017) 820–826.
[2] C. Haller, et al., Burying non-radiative defects in InGaN underlayer to increase InGaN/GaN quantum well efficiency, Appl. Phys. Lett. 111 (26) (2017) 262101.
[3] George M. Christian, et al., Room temperature PL efficiency of InGaN/GaN quantum well structures with prelayers as a function of number of quantum wells, Phys. Status Solidi 13.5-6 (2016) 248–251.
[4] D.O. Demchenko, Michael A. Reshchikov, Blue luminescence and Zn acceptor in GaN, Phys. Rev. B 88 (11) (2013) 115204.
[5] Michael A. Reshchikov, Hadis Morkoç, Luminescence properties of defects in GaN, J. Appl. Phys. 97 (6) (2005) 5–19.
[6] J.I. Pankove, J.E. Berkeyheiser, E.A. Miller, Properties of Zn-doped GaN. I. Photoluminescence, J. Appl. Phys. 45 (3) (1974) 1280–1286.
[7] Michael A. Reshchikov, Giant shifts of photoluminescence bands in GaN, J. Appl. Phys. 127 (5) (2020), 055701.
[8] Michel Boulou, et al., Recombination mechanisms in GaN: Zn, J. Lumin. 18 (1979) 767–770.
[9] Shuji Nakamura, High-power InGaN/AlGaN double-heterostructure blue-light-emitting diodes, in: Proceedings of 1994 IEEE International Electron Devices Meeting. IEEE, 1994, pp. 567–570.
[10] Jinn-Kong Sheu, et al., White-light emission from InGaN-GaN multiquantum-well light-emitting diodes with Si and Zn codoped active well layer, IEEE Photon. Technol. Lett. 14 (4) (2002) 450–452.
[11] Tomás Hubácek, et al., Improvement of luminescence properties of GaN buffer layer for fast nitride scintillator structures, J. Cryst. Growth 464 (2017) 221–225.
[12] Stefan Birner, et al., Nextnano: general purpose 3-D simulations, IEEE Trans. Electron. Dev. 54 (9) (2007) 2137–2142.
[13] Tomás Hubácek, et al., Advancement toward ultra-thick and bright InGaN/GaN structures with a high number of QWs, CrystEngComm 21 (2) (2019) 356–362.
[14] M. Tapajna, A. Vincze, P. Noga, J. Dobrovodský, A. Svagátová, S. Hasenöhr, D. Gregušova, J. Kuzmik, 12th international conference on advanced semiconductor devices and microsystems (ASDAM), IEEE 1 (2018) (2018).
[15] MATSUBARA, Masahiko; BELLOTTI, Enrico, A first-principles study of carbon-related energy levels in GaN. I. Complexes formed by substitutional/interstitial carbons and gallium/nitrogen vacancies, J. Appl. Phys. 121 (19) (2017) 195701.
[16] C. Haller, et al., GaN surface as the source of non-radiative defects in InGaN/GaN quantum wells, Appl. Phys. Lett. 113 (11) (2018) 111106.

Donor-Acceptor pairs recombination as the origin of the emission shift in InGaN/GaN scintillator heterostructures doped with Zn

František Hájek[1,2*], Vítězslav Jarý[1], Tomáš Hubáček[1], Filip Dominec[1], Alice Hospodková[1], Karla Kuldová[1], Jiří Oswald[1], Jiří Pangrác[1], Tomáš Vaněk[1], Maksym Buryi[1], Gilles Ledoux[3], Christophe Dujardin[3]

[1]Institute of Physics of the Czech Academy of Sciences, v.v.i., Cukrovarnická 10, 162 00, Prague 6, Czech Republic

[2]Czech Technical University in Prague, Faculty of Nuclear Sciences and Physical Engineering, Břehová 7, 115 19, Prague 1, Czech Republic

[3]Institut Lumière Matière, UMR55306 Université Claude Bernard, Lyon 1-CNRS, France

[*]corresponding author: hajek@fzu.cz

Abstract

We report luminescence decay characteristics of the InGaN/GaN scintillator heterostructures doped with Zn. Unusually large shifting of luminescence band caused by Zn acceptors incorporated in InGaN is observed both in time-resolved and excitation-dependent spectra. Origins of the shifts are discussed, and model based on donor-acceptor pair recombination is introduced. The results imply a shrinkage of donor Bohr radius compared to the bulk material caused by quantum confinement effect. The slow decay of Zn band points out to the necessity of Zn impurity elimination in applications requiring fast timing characteristics of a scintillator.

Introduction

A large demand for scintillators with fast response leads to investigating new materials from the perspective of high-energy radiation response. InGaN/GaN heterostructures with decay times in order of ns are one of the promising candidates in applications like Time-of-Flight Positron Emission Tomography (TOF-PET) [1–3]. However, several issues concerning InGaN/GaN scintillators must be solved: except problems arising from limited thickness of InGaN/GaN active region, the unwanted defect luminescence with long decay times is a significant obstacle hindering the widespread of nitride-based materials as scintillators. Therefore, understanding the defect nature and their recombination mechanisms is of great importance nowadays.

Zinc impurities are one of the common contaminants found in GaN and InGaN layers grown by Metal Organic Vapour Phase Epitaxy (MOVPE). Their behavior is quite well-documented since Zn doping of InGaN was studied as a potential solution for fabrication of white light-emitting diodes (LEDs) [4–6]. The Zn doping results into broad luminescence band (ZnB) shifted about 400-500 meV to lower energies than the main luminescence peak originating from InGaN band-to-band recombination. The origin of ZnB was assigned to donor-acceptor pair (DAP) recombination between Si donors and Zn acceptors [4,5]. In GaN, Zn forms a relatively deep acceptor when substituting Ga atom with the energy level around 390 meV from the valence band [7] while Si acts as a shallow donor with ionization energy of 25 meV when introduced in low concentration [8]. However, there is a lack of reports considering the luminescence decay kinetics of ZnB in literature despite the decay kinetics is important factor for scintillator development.

ZnB exhibit unusually large spectral blue-shifting with increasing excitation intensity. Several explanations of the shifts were provided by different authors. They were assigned to tunnelling

currents [9], band filling effect alongside with piezoelectric field screening [10], competition between different luminescence bands [6] and the DAP recombination mechanism. In the latter case the shift happens due to the Coulombic interaction between ionized donors and acceptors [5]. The large shifts were actually one of the reasons why the InGaN:(Zn, Si) failed on the white LED market.

In this paper, steady-state, and time-resolved Photoluminescence (PL) and Secondary ion mass spectroscopy (SIMS) measurements are applied to study the luminescence decay of ZnB and to resolve the origin of ZnB luminescence shifts. A phenomenological model is used to explain the large shifts by DAP recombination involving donor with lowered Bohr radius due to the quantum confinement in InGaN layers.

Experimental

Samples were prepared by MOVPE on a *c*-oriented sapphire substrate. First, commonly applied GaN buffer layer was deposited. More information can be found in [11]. Trimethylgallium was used as Ga precursor and NH_3 as the nitrogen one. These layers were grown in H_2 atmosphere. Then, Si-doped GaN was grown (Si doping was employed to smear the piezoelectric field inside the QWs and thus increase the electron-hole wavefunction overlap). A thin low-temperature (LT) GaN was placed between GaN buffer and InGaN/GaN active region to incorporate impurities flowing on the growth surface [12]. InGaN/GaN active region was grown from Triethylgallium precursor for Ga, Trimethylindium for In and NH_3 for nitrogen in N_2 atmosphere. More information can be found in [13]. The first 5 InGaN QWs separated by GaN barriers were grown followed by GaN separation layer and another stack of 5 QWs and barriers. The Zn doping in InGaN QWs is not intentional and varies among the samples. The samples P1, P2 and P3 studied in this work are nominally identical except the growth parameters listed in Tab. 1. InGaN QWs are also doped by Si which diffuses from the GaN:Si layer, see Fig. 2. The whole structure is capped by thin GaN layer. The structure is schematically shown in Fig. 1.

Table 1: Growth parameters of the studied samples.

Sample	GaN cap thickness (nm)	Si nominal concentration in buffer [cm^{-3}]	LT GaN thickness [nm]
P1	65	$1x10^{18}$	8
P2	12	$3x10^{18}$	60
P3	12	$1x10^{18}$	8

Results

Concentration quenching of Zn in GaN was reported at concentrations about $8 \cdot 10^{18}$ cm^{-3} [16], which is far beyond the usual unintentional doping level. The ZnB photoluminescence intensity is thus expected to be proportional to Zn concentration. To reveal relationship between Zn band in PL and Zn concentration in samples, SIMS measurements were performed on three samples P1, P2 and P3. Fig. 2 shows the SIMS profile of Zn for all samples in the vicinity of the quantum well region. Sample P1 has thicker capping layer so the SIMS profile of sample P1 is shifted by the thickness of the capping layer for clarity. The grey dash-dot line represents the In signal from sample P2 and hence, marks positions of QWs. All samples show increased Zn concentration by almost 1 order of magnitude in InGaN QWs compared to GaN barriers. SIMS signal is disturbed by the surface artefacts for the top 5 QWs in the case of sample P2. Si concentration for sample P2 is also shown in Fig. 2. Preferential incorporation of residual Si into InGaN layers is observed.

Photoluminescence spectra excited by 325 nm are shown in Fig. 3. Emission from InGaN quantum wells (QW) is observed at higher energy while the broad band at lower energy is assigned to the ZnB band. Both peaks were fitted with functions adapted to the origin of the bands. For QW recombination, the pseudo-Voigt function while the Zn bands were fitted with the model from [17], which takes into account the phonon interaction of a given luminescence centre with lattice:

$$I(h\nu) = I_{\max} \exp[-2S(\sqrt{\frac{E_0 - h\nu}{E_0 - h\nu_{\max}}} - 1)^2] \quad (1)$$

The intensity of ZnB is plotted against the averaged Zn concentration in the QWs measured by SIMS in inset of Fig. 3 (only data from the 5 QWs closer to the substrate were used because of the SIMS surface artefact of measurement). Monotonous dependence is observed suggesting that concentration quenching does not take place. So-called yellow luminescence commonly observed in GaN samples was almost more than two orders of magnitude weaker in our InGaN/GaN samples under laser 325 nm excitation conditions, so it was not included into the fitting procedure (checked

on reference sample without InGaN QWs). Oscillations modifying the PL spectra are interference fringes and their period is determined by total thickness of nitride layers.

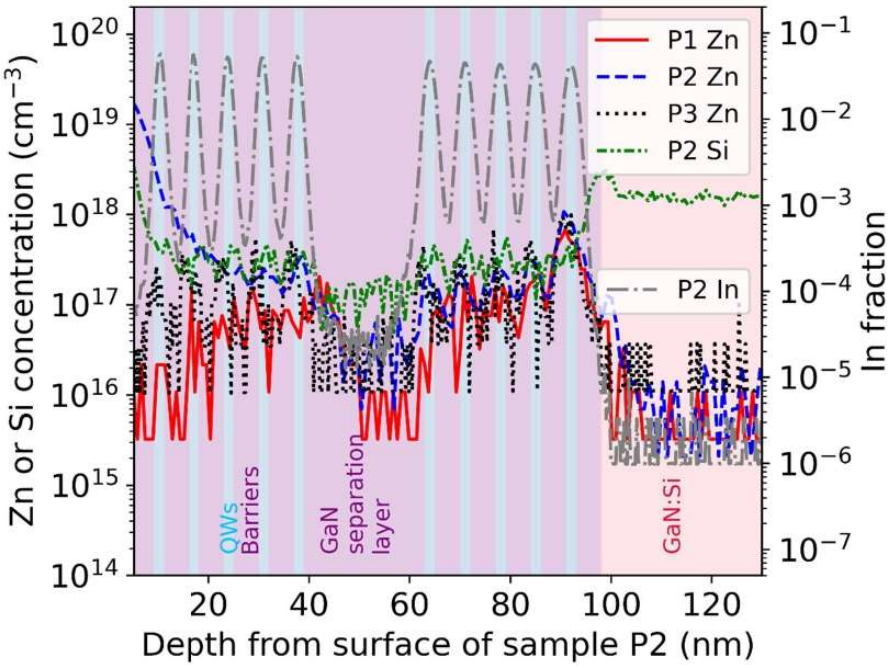

Figure 2: SIMS measurement of samples P1, P2 and P3. Signal of sample P1 is shifted because of the thicker cap layer atop the structure.

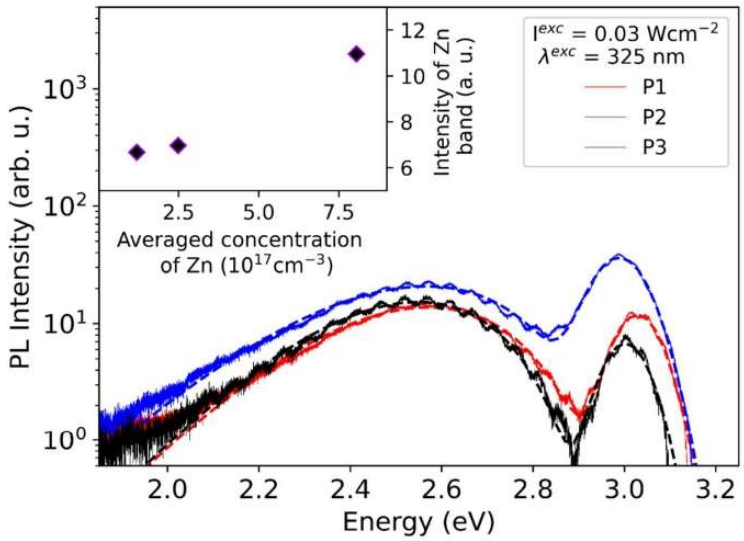

Figure 3: PL spectra of the samples P1, P2, and P3. Spectra were fitted (dashed lines) as described in the text. Inset shows the monotonic dependence of ZnB intensity on averaged Zn concentration in the InGaN layers.

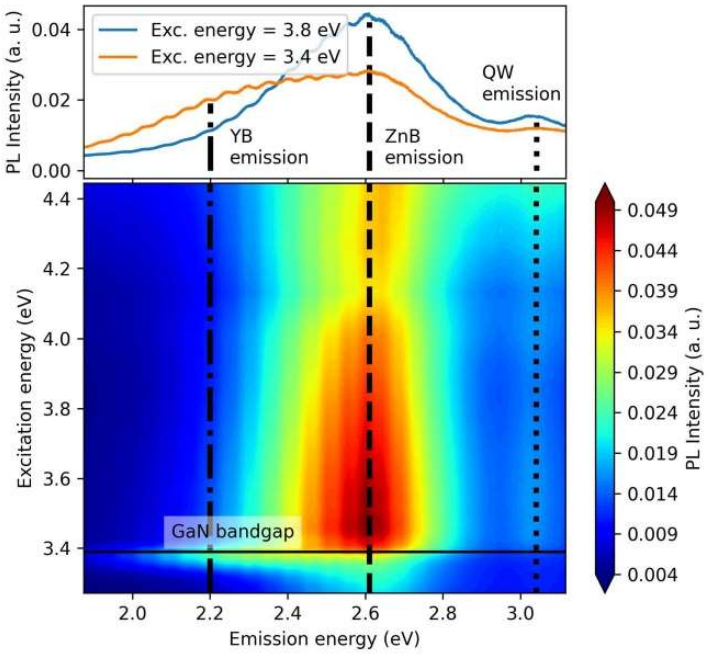

Figure 4: RT Excitation-emission map of sample P1. QW emission at 3.03 eV (dotted line) and ZnB emission at 2.61 eV (dashed line) are clearly observed for all excitation energies above the GaN bandgap. ZnB is observed also below GaN bandgap (3.39 eV, solid line). At 366 nm excitation, yellow band at 2.2 (dash-dot line) is observed. TOP: an emission spectrum from the map at excitation energy 3.8 eV (= 325 nm).

Excitation-emission map is shown in Fig. 4 for sample P1. Zn acceptors are known to have exceptionally large hole capture cross-section coefficients (5×10^{-7} cm^3s^{-1} [17]) making them very effective luminescence centers and they can be the dominant recombination channel, especially at low excitation intensities before all Zn acceptors are saturated. Below GaN bandgap, absorption of excitation light is very weak (only in QWs) which leads to only observable band being ZnB. Under 3.38 eV (= 366 nm) excitation energy, yellow band (YB) at 2.2 eV from carbon impurities which are present in GaN buffer [18–20] emerges, too. The YB is not observed with the above bandgap excitation because in such case, the excitation light is absorbed in the QW region. On the other hand, YB is not observed for wavelengths much longer than GaN bandgap since the excitation of YB happens through shallow below-bandgap states of GaN. The problem of YB luminescence decay kinetics was described earlier in [21]. In [21] we showed that the mean decay time of YB can be accelerated from millisecond range to hundreds of ns by Si or Ge doping of GaN buffer layer.

For the above GaN bandgap excitation wavelengths, ZnB alongside with QW emission are seen.

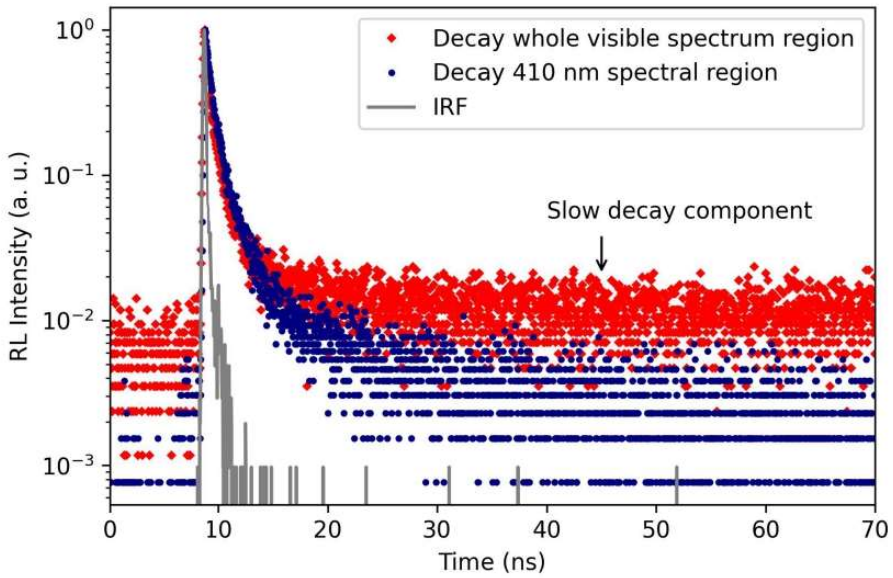

Figure 5: Time decay of luminescence excited by soft X-ray (sample P1). When the whole visible spectral region is measured (red), and with a filter centered at 410 nm (dark blue). Instrument response function (IRF) is also plotted (grey).

The temporal performance of a scintillator was tested by soft X-ray excitation. Beside the very fast component from QW luminescence (main component with characteristic decay time 0.4 ns), a component with very long decay time can be observed (Fig. 5) when no spectral filer is used. However, this component disappears when only QW emission is measured (filtered at 410nm). Since the most pronounced spectral component aside from QW luminescence is ZnB (Fig. 3, 4), we ascribe this long component to this band.

The time decays of ZnB were studied also under optical excitation. The decays are non-exponential and wavelength-dependent. Therefore, time resolved spectra are convenient to understand the recombination mechanism. Time decays obtained for wavelengths with step 5 nm in the range 420 – 600 nm were divided into 20 time windows ranging from a few tens of ns to a few tens of microseconds. Time-resolved spectra were constructed from these time decay curves. Example of the time evolution of the spectra for sample P3 is shown in Fig. 6a (only 7 spectra are shown for better clarity). The ZnB shift towards lower energies at longer times can be clearly observed. Similarly, the shift of the ZnB is also seen with decreasing excitation intensity in steady state conditions (example of sample P3 is presented in Fig. 6b).

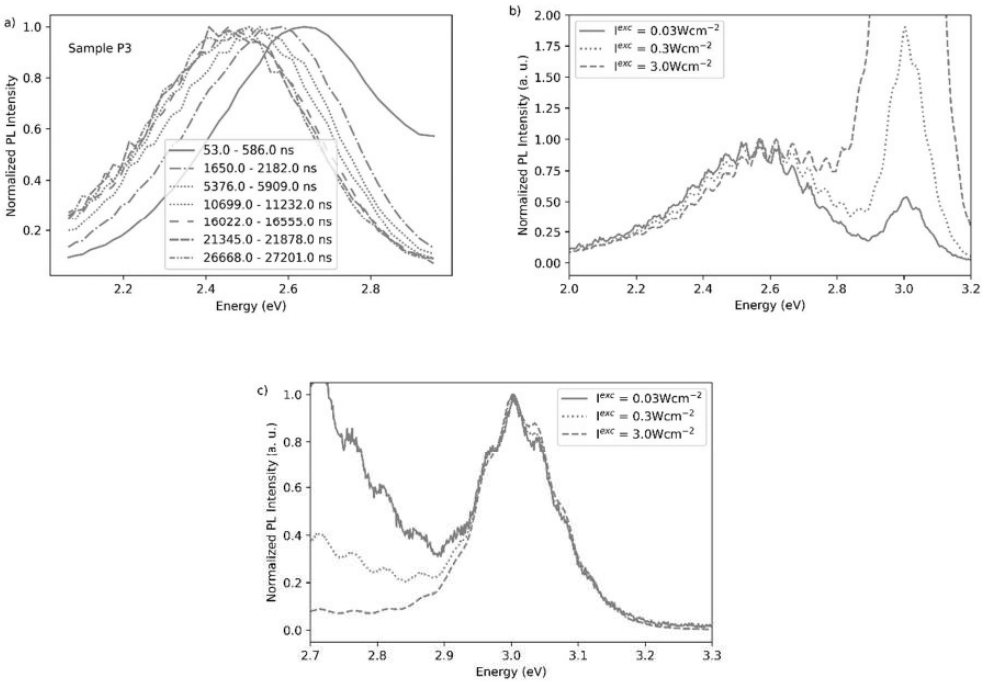

Figure 6: a) Shift of the time-resolved PL spectra of sample P3. b) shift of the steady-state spectra normalized to ZnB maximum of sample P3 with excitation intensity. Shift to the lower energies is clearly observed either with longer decay times or lower excitation intensities. c) PL spectra normalized to QW peak maximum. No shift of QW peak is observed with different excitation intensities.

Since the shape of the band remains almost identical during the shifting, we rule out the possibility that the competition of different channels could be the main source of the band shift, as suggested in [16]. Tunneling currents as the origin of ZnB shifting [9] can be excluded in our case since the excitation is not an electrical, but an optical one. The influence of the electrical field caused by the difference in spontaneous and piezoelectric polarizations between InGaN and GaN should be considered as the cause for the band shift. If this field can be efficiently screened by excited charge, the shift happens both in time resolved-spectra and in excitation intensity-dependent PL spectra. However, this would also result in the shift of QW recombination peak, which is not observed (Fig. 6c). We could argue, that the shift of ZnB is caused by interaction of the Zn^- ions (which remain after in the electric field after the recombination) with the polarization charge. But if we consider the magnitude of the effect, we have to reject this hypothesis: the polarization field in QWs is caused by interface charge in order of 10^5 eV/µm^2 [22]. The number of Zn ions in the 2 nm wide QW and concentration 10^{18} cm^{-3} (upper limit in our samples measured by SIMS), is at least two orders of magnitudes smaller than the interface charge. Therefore, screening of the interface charge cannot lead to significant shift of the ZnB.

Therefore, we will reflect on the possibility of DAP recombination being the source of the blueshift and introduce a model describing the energy shift during the time decay of DAP recombination. In the DAP mechanism, the probability of recombination of one is given by [23]

$$\frac{1}{\tau_{DAP}} = W(R) = W_{max} \cdot e^{-\frac{2R}{a_D}} \qquad (2)$$

The a_D is the Bohr radius of the weakly bound particle, which is the electron in our case. *R* is the distance between donor and acceptor and W_{max} is the limit probability of recombination in the case of an infinitesimally close pair. Moreover, the probability of recombination can be considered as the inversion of radiative lifetime of a given DAP τ_{DAP}.

In the approximation of nearest-neighbor recombination, the luminescence decay time of one DAP will be mono-exponential. Therefore, we can assume that the luminescence intensity decay $I_R(t)$ of a single DAP pair will have form

$$I_R(t) = A \cdot \exp\left(\frac{-t}{\tau_{DAP}(R)}\right) = W(R) \exp\left(\frac{-t}{\tau_{DAP}(R)}\right) \qquad (3)$$

if we substitute the amplitude *A* of the decay with probability of the recombination *W(R)*. To proceed further, the distribution of the donor-acceptor pair distances *G(R)* must be known. In bulk material, theory of DAP distance distribution is well explored, for example [24], but for complicated system such as InGaN/GaN QWs structure, the *G(R)* has to be obtained numerically, as is explained below. With known *G(R)* we can obtain the decay curve of the whole donor-acceptor system simply by summation of $I_R(t)$ for each time *t*

$$I(t) = \sum_R I_R(t) \cdot G(R) \qquad (4)$$

Moreover, we can obtain the time-dependent energy shift from this model. Let E_R be the energy shift of a given pair caused by Coulombic interaction. In the first approximation, the interaction between the charged ions at distance *R* can be described by

$$E_R = k_e \frac{e^2}{\varepsilon R} \qquad (5)$$

where *e* is the elementary charge and ε is the static permittivity of the material (ε_r = 10 was assumed for GaN [25]) and k_e is the Coulomb constant. The mean energy shift of the whole DAP system at given time *t* can then be estimated:

$$E(t) = \frac{\sum_R E_R \cdot I_R(t) \cdot G(R)}{\sum_R I_R(t) \cdot G(R)} \qquad (6)$$

As explained above, to apply the model for the time shift of ZnB, the *G(R)* distribution must be known. Therefore, we used the SIMS profiles of Zn and Si (assumed Si to be the donor involved in the DAP recombination) and performed simulation of random distribution of Zn and Si atoms in the structure according the depth distribution of the atoms in the InGaN QWs. The lateral dimensions were taken large enough to have at least 70 000 Zn atoms for each sample. The depth resolution of the simulation was 1 nm and the studied region involved only the 5 closer-to-substrate QWs because of the SIMS measurement artefacts as mentioned earlier. For these concentration profiles, the nearest-neighbor donor and acceptors were found, and their distance was used. Example of histogram representing the *G(R)* distribution probability is shown in Fig. 7 (sample P3).

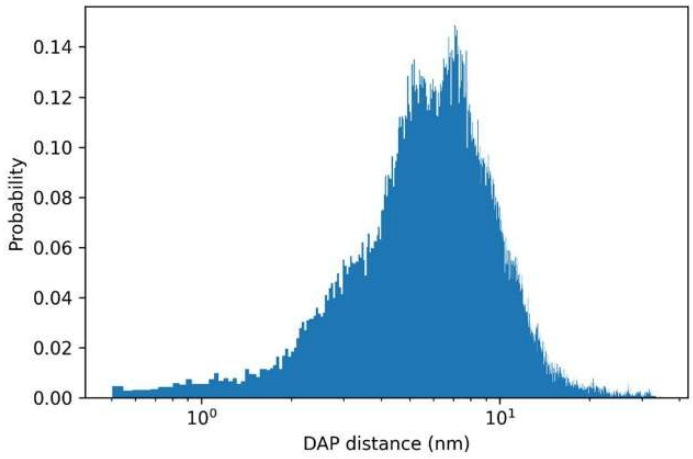

Figure 7: Distribution of donor acceptor pair distances in sample P3.

Unfortunately, we do not have the SIMS data of Si for sample P1. Therefore, even Si distribution was assumed in the InGaN QWs equal to 10^{17} cm^{-3}. Calculation by eq. (4) and eq. (6) and comparison with experimental results are shown in Fig. 8a-c and 9a-c, respectively. Experimental *E(t)* were obtained from fits of the time resolved spectra (example in Fig. 6a) with the eq. 1).

The shift measured experimentally also needs the energy E_0 representing the energy of recombination at infinite long time. Calculation parameters are given in the Fig. 9 and in Tab. 2.

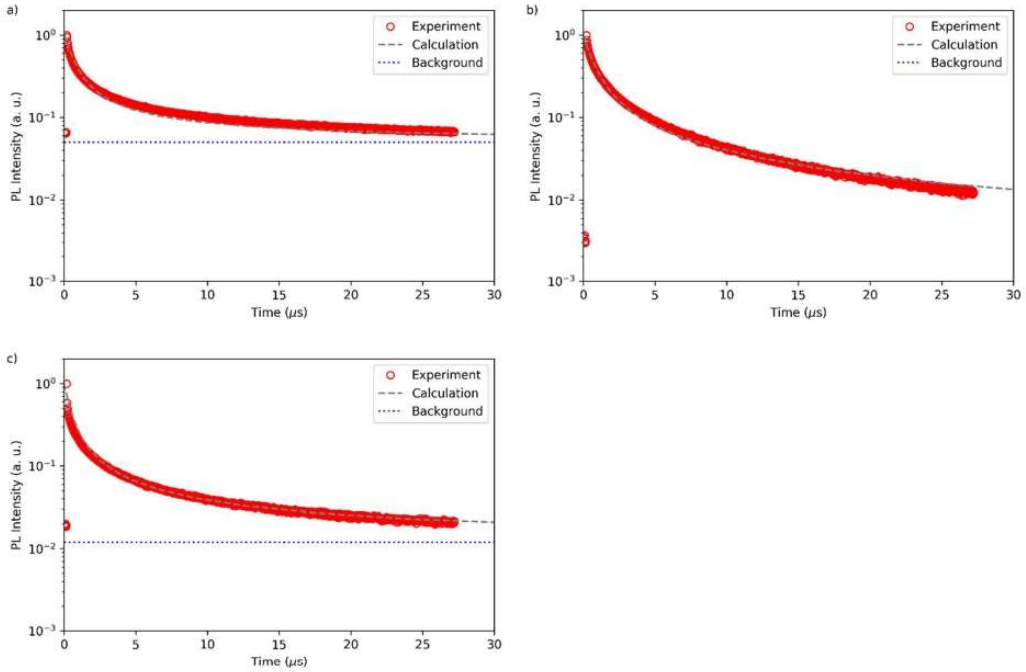

Figure 8: Decay curves of luminescence for samples a) P1, b) P2, c) P3 and the calculated curves using eq. (4) and G(R) from SIMS.

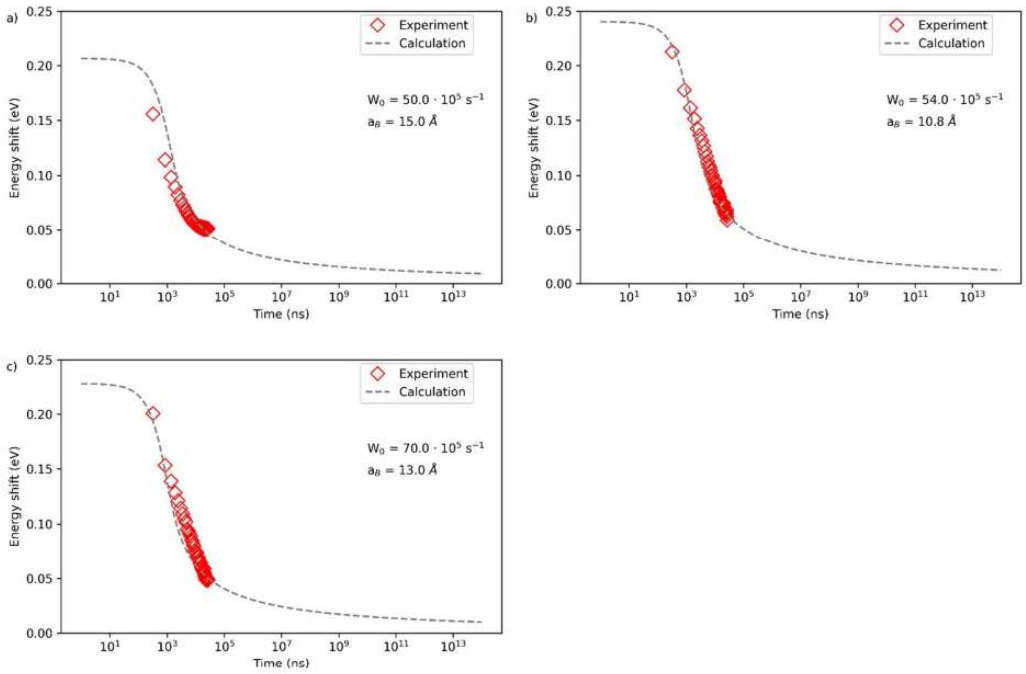

Figure 9: Energy shifts for the samples a) P1, b) P2, c) P3 and the calculated profiles using eq. (6). The parameters of the calculation are given in the picture.

Tab. 1: Calculation parameters for samples P1, P2 and P3.

Sample	a_B (Å)	W_{max} (10^5 s^{-1})	E_0 (eV)
P1	15.0	50	2.39
P2	10.8	54	2.37
P3	13.0	70	2.40

The proposed model reproduces well the experimental data for both decay curves and the energy shifts allowing to deduce the parameters W_{max} and a_B summarized in Tab. 2. The weak dispersion of the obtain values is coherent with the model. One can note a small Bohr radius for the shallow donor. In GaN, the Bohr radius for Si is calculated to be 28 Å [21]. The much smaller value obtained from the calculation can be ascribed to the quantum confinement effect. The lowering of the Bohr radius in the QW and its surroundings is well documented and theoretically explained [26,27]. The quantum confinement is also probably responsible for efficient DAP recombination at room temperature because it increases the activation energy of the donor ensuring the process is not thermally quenched or replaced by electron-acceptor (e-A) recombination mechanism.

We should mention that the Bohr radius lowering is probably not only one-dimensional in the growth direction, but the Bohr radius might also be reduced in the lateral dimension. This would be caused by local potential fluctuations on the nm scale in InGaN alloy which are present because of the random In concentration fluctuations and well width fluctuations [28–30].

Time-resolved measurements clearly show that Zn impurity elimination is necessary for applications requiring the ns resolution. On the other hand, a very efficient luminescence of ZnB at low excitation intensities (Fig. 6b) might benefit the Zn doping of InGaN layers in applications requiring a high light-yield and moderate time-resolution.

Conclusion

In summary, we examined the kinetics of the Zn impurity band in InGaN/GaN heterostructures. The important characteristics of the ZnB are the large shifts of ZnB caused by DAP recombination between Si and Zn donors in InGaN/GaN quantum heterostructures in time-resolved and excitation-intensity dependent PL spectra. A model based on DAP theory has been applied and provided explanation for the experimental data well. A smaller Bohr radius for the donor was found compared to the pure GaN material which implicates the quantum confinement effect playing a role in the recombination process. Higher donor binding energy make from the DAP recombination the dominant mechanism over e-A mechanism even at room temperature in InGaN:Zn(Si). The ZnB luminescence is slow and therefore, detrimental for applications like TOF-PET requiring fast luminescence decay.

Acknowledgement

This work was supported by the Czech Science Foundation project No. 20-05497Y and partly by the Grant Agency of the Czech Technical University in Prague by project No.SGS22/182/OHK4/3T/14.

References

[1] A. Hospodková, M. Nikl, O. Pacherová, J. Oswald, P. Brůža, D. Pánek, B. Foltynski, E. Hulicius, A. Beitlerová, M. Heuken, InGaN/GaN multiple quantum well for fast scintillation application: radioluminescence and photoluminescence study, Nanotechnology. 25 (2014) 455501. https://doi.org/10.1088/0957-4484/25/45/455501.

[2] G. Toci, L.A. Gizzi, P. Koester, F. Baffigi, L. Fulgentini, L. Labate, A. Hospodkova, V. Jary, M. Nikl, M. Vannini, InGaN/GaN multiple quantum well for superfast scintillation application: Photoluminescence measurements of the picosecond rise time and excitation density effect, J. Lumin. 208 (2019) 119–124. https://doi.org/10.1016/J.JLUMIN.2018.12.034.

[3] P. Lecoq, Pushing the Limits in Time-of-Flight PET Imaging, IEEE Trans. Radiat. Plasma Med. Sci. 1 (2017) 473–485. https://doi.org/10.1109/TRPMS.2017.2756674.

[4] S. Nakamura, High-power InGaN/AlGaN double-heterostructure blue-light-emitting diodes, Tech. Dig. - Int. Electron Devices Meet. (1994) 567–570. https://doi.org/10.1109/IEDM.1994.383328.

[5] J.K. Sheu, C.J. Pan, G.C. Chi, C.H. Kuo, L.W. Wu, C.H. Chen, S.J. Chang, Y.K. Su, White-light emission from InGaN-GaN multiquantum-well light-emitting diodes with Si and Zn codoped active well layer, IEEE Photonics Technol. Lett. 14 (2002) 450–452. https://doi.org/10.1109/68.992574.

[6] P.G. Eliseev, V.A. Smagley, P. Perlin, P. Sartori, M. Osinski, Analysis of impurity-related blue emission in Zn-doped GaN/InGaN/AlGaN double heterostructure, Proc. SPIE - Int. Soc. Opt. Eng. 2693 (1996) 97–108. https://doi.org/10.1117/12.238944.

[7] D.O. Demchenko, M.A. Reshchikov, Blue luminescence and Zn acceptor in GaN, Phys. Rev. B - Condens. Matter Mater. Phys. 88 (2013) 115204. https://doi.org/10.1103/PHYSREVB.88.115204/FIGURES/5/MEDIUM.

[8] A. Wolos, Z. Wilamowski, M. Piersa, W. Strupinski, B. Lucznik, I. Grzegory, S. Porowski, Properties of metal-insulator transition and electron spin relaxation in GaN:Si, Phys. Rev. B. 83 (2011) 165206. https://doi.org/10.1103/PhysRevB.83.165206.

[9] P.G. Eliseev, P. Perlin, J. Furioli, P. Sartori, J. Mu, M. Osiński, Tunneling current and electroluminescence in InGaN: Zn,Si/AlGaN/GaN blue light emitting diodes, J. Electron. Mater.

1997 263. 26 (1997) 311–319. https://doi.org/10.1007/S11664-997-0170-0.

[10] J.K. Sheu, T.-W. Yeh, G. Chi, M.J. Jou, Luminescence of the InGaN/GaN blue light-emitting diodes, Disp. Technol. III. 4079 (2000) 143. https://doi.org/10.1117/12.389421.

[11] T. Hubáček, A. Hospodková, J. Oswald, K. Kuldová, J. Pangrác, Improvement of luminescence properties of GaN buffer layer for fast nitride scintillator structures, J. Cryst. Growth. 464 (2017) 221–225. https://doi.org/10.1016/J.JCRYSGRO.2016.12.088.

[12] C. Haller, J.F. Carlin, G. Jacopin, W. Liu, D. Martin, R. Butté, N. Grandjean, GaN surface as the source of non-radiative defects in InGaN/GaN quantum wells, Appl. Phys. Lett. 113 (2018) 111106. https://doi.org/10.1063/1.5048010.

[13] T. Hubáček, A. Hospodková, K. Kuldová, J. Oswald, J. Pangrác, V. Jarý, F. Dominec, M. Slavická Zíková, F. Hájek, E. Hulicius, A. Vetushka, G. Ledoux, C. Dujardin, M. Nikl, Advancement toward ultra-thick and bright InGaN/GaN structures with a high number of QWs, CrystEngComm. 21 (2019) 356–362. https://doi.org/10.1039/C8CE01830H.

[14] J.F. Muth, J.D. Brown, M.A.L. Johnson, Z. Yu, R.M. Kolbas, J.W. Cook, J.F. Schetzina, Absorption Coefficient and Refractive Index of GaN, AlN and AlGaN Alloys, Mater. Res. Soc. Internet J. Nitride Semicond. Res. 4 (1999) 502–507. https://doi.org/10.1557/S1092578300002957.

[15] J. Mooney, P. Kambhampati, Erratum: Get the basics right: Jacobian conversion of wavelength and energy scales for quantitative analysis of emission spectra (Journal of Physical Chemistry Letters (2013) 4:19 (3316?3318) DOI: 10.1021/jz401508t), J. Phys. Chem. Lett. 5 (2014) 3497. https://doi.org/10.1021/JZ502066V/ASSET/IMAGES/LARGE/JZ-2014-02066V_0001.JPEG.

[16] M. Boulou, M. Furtado, G. Jacob, D. Bois, Recombination mechanisms in GaN:Zn, J. Lumin. 18–19 (1979) 767–770. https://doi.org/10.1016/0022-2313(79)90232-1.

[17] M.A. Reshchikov, Measurement and analysis of photoluminescence in GaN, J. Appl. Phys. 129 (2021) 121101. https://doi.org/10.1063/5.0041608.

[18] J.L. Lyons, A. Janotti, C.G. Van De Walle, Carbon impurities and the yellow luminescence in GaN, Appl. Phys. Lett. 97 (2010) 152108. https://doi.org/10.1063/1.3492841.

[19] F. Zimmermann, J. Beyer, C. Röder, F.C. Beyer, E. Richter, K. Irmscher, J. Heitmann, Current Status of Carbon-Related Defect Luminescence in GaN, Phys. Status Solidi. 218 (2021) 2100235. https://doi.org/10.1002/PSSA.202100235.

[20] M.A. Reshchikov, M. Vorobiov, D.O. Demchenko, Ozgur, H. Morkoç, A. Lesnik, M.P. Hoffmann, F. Hörich, A. Dadgar, A. Strittmatter, Two charge states of the C N acceptor in GaN: Evidence from photoluminescence, Phys. Rev. B. 98 (2018) 125207. https://doi.org/10.1103/PHYSREVB.98.125207/FIGURES/17/MEDIUM.

[21] T. Vaněk, V. Jarý, T. Hubáček, F. Hájek, K. Kuldová, Z. Gedeonová, V. Babin, Z. Remeš, M. Buryi, Acceleration of the yellow band luminescence in GaN layers via Si and Ge doping, J. Alloys Compd. 914 (2022) 165255. https://doi.org/10.1016/J.JALLCOM.2022.165255.

[22] O. Ambacher, J. Majewski, C. Miskys, A. Link, M. Hermann, M. Eickhoff, M. Stutzmann, F. Bernardini, V. Fiorentini, V. Tilak, B. Schaff, L.F. Eastman, Pyroelectric properties ofAl(In)GaN/GaN hetero- and quantum well structures, J. Phys. Condens. Matter. 14 (2002) 3399. https://doi.org/10.1088/0953-8984/14/13/302.

[23] M.A. Reshchikov, H. Morkǫ, Luminescence properties of defects in GaN, J. Appl. Phys. 97 (2005). https://doi.org/10.1063/1.1868059.

[24] H. Reiss, C.S. Fuller, F.J. Morin, Chemical Interactions Among Defects in Germanium and

Silicon, Bell Syst. Tech. J. 35 (1956) 535–636. https://doi.org/10.1002/J.1538-7305.1956.TB02393.X.

[25] Y. Lei, 雷勇, H. Shi, 石宏彪, H. Lu, 陆海, D. Chen, 陈敦军, R. Zhang, 张荣, Y. Zheng, 郑有炓, Field plate engineering for GaN-based Schottky barrier diodes, J. Semicond. 34 (2013) 054007. https://doi.org/10.1088/1674-4926/34/5/054007.

[26] S. Perraud, K. Kanisawa, Z.-Z. Wang, T. Fujisawa, Direct Measurement of the Binding Energy and Bohr Radius of a Single Hydrogenic Defect in a Semiconductor Quantum Well, (2008). https://doi.org/10.1103/PhysRevLett.100.056806.

[27] P. (Paul) Harrison, A. Valavanis, Quantum wells, wires and dots : theoretical and computational physics of semiconductor nanostructures, (n.d.).

[28] N.K. Van Der Laak, R.A. Oliver, M.J. Kappers, C.J. Humphreys, Role of gross well-width fluctuations in bright, green-emitting single InGaN/GaN quantum well structures, Appl. Phys. Lett. 90 (2007) 121911. https://doi.org/10.1063/1.2715166.

[29] Y.S. Lin, K.J. Ma, C. Hsu, S.W. Feng, Y.C. Cheng, C.C. Liao, C.C. Yang, C.C. Chou, C.M. Lee, J.I. Chyi, Dependence of composition fluctuation on indium content in InGaN/GaN multiple quantum wells, Appl. Phys. Lett. 77 (2000) 2988–2990. https://doi.org/10.1063/1.1323542.

[30] S. Chichibu, T. Sota, K. Wada, S. Nakamura, Exciton localization in InGaN quantum well devices, J. Vac. Sci. Technol. B Microelectron. Nanom. Struct. Process. Meas. Phenom. 16 (1998) 2204. https://doi.org/10.1116/1.590149.

materials

MDPI

Article

Relation between Ga Vacancies, Photoluminescence, and Growth Conditions of MOVPE-Prepared GaN Layers

Alice Hospodková [1,*], Jakub Čížek [2], František Hájek [1,3], Tomáš Hubáček [1], Jiří Pangrác [1], Filip Dominec [1], Karla Kuldová [1], Jan Batysta [1,3], Maciej O. Liedke [4], Eric Hirschmann [4], Maik Butterling [4] and Andreas Wagner [4]

[1] Institute of Physics CAS, Cukrovarnická 10, 162 00 Prague, Czech Republic
[2] Faculty of Mathematics and Physics, Charles University, V Holešovičkách 2, 180 00 Prague, Czech Republic
[3] Faculty of Nuclear Sciences and Physical Engineering, Czech Technical University, Břehová 7, 115 19 Prague, Czech Republic
[4] Institute of Radiation Physics, Helmholtz-Zentrum Dresden-Rossendorf, Bautzner Landstr. 400, 01328 Dresden, Germany
* Correspondence: hospodko@fzu.cz

Abstract: A set of GaN layers prepared by metalorganic vapor phase epitaxy under different technological conditions (growth temperature carrier gas type and Ga precursor) were investigated using variable energy positron annihilation spectroscopy (VEPAS) to find a link between technological conditions, GaN layer properties, and the concentration of gallium vacancies (V_{Ga}). Different correlations between technological parameters and V_{Ga} concentration were observed for layers grown from triethyl gallium (TEGa) and trimethyl gallium (TMGa) precursors. In case of TEGa, the formation of V_{Ga} was significantly influenced by the type of reactor atmosphere (N_2 or H_2), while no similar behaviour was observed for growth from TMGa. V_{Ga} formation was suppressed with increasing temperature for growth from TEGa. On the contrary, enhancement of V_{Ga} concentration was observed for growth from TMGa, with cluster formation for the highest temperature of 1100 °C. From the correlation of photoluminescence results with V_{Ga} concentration determined by VEPAS, it can be concluded that yellow band luminescence in GaN is likely not connected with V_{Ga}; additionally, increased V_{Ga} concentration enhances excitonic luminescence. The probable explanation is that V_{Ga} prevent the formation of some other highly efficient nonradiative defects. Possible types of such defects are suggested.

Keywords: GaN; defects; positron annihilation spectroscopy; photoluminescence; MOVPE

Citation: Hospodková, A.; Čížek, J.; Hájek, F.; Hubáček, T.; Pangrác, J.; Dominec, F.; Kuldová, K.; Batysta, J.; Liedke, M.O.; Hirschmann, E.; et al. Relation between Ga Vacancies, Photoluminescence, and Growth Conditions of MOVPE-Prepared GaN Layers. *Materials* **2022**, *15*, 6916. https://doi.org/10.3390/ma15196916

Academic Editor: Ioana Pintilie

Received: 1 September 2022
Accepted: 27 September 2022
Published: 5 October 2022

1. Introduction

Optimization of methods for high-quality GaN growth in the 1990s paved the way for GaN-based power-efficient optoelectronic devices [1]. Highly efficient InGaN blue and white LEDs are now commercially available [1]. Thanks to the high polarization coefficient and ability to form heterostructures, AlGaN/GaN high electron mobility transistors can be manufactured, and these can be found in many applications these days [2]. Other applications of GaN-based devices include UV detectors [3], photovoltaic cells [4], and scintillators [5]. Despite extensive research on both the application and basic properties of GaN and related materials in the past three decades, several fundamental questions remain unanswered. One of them is the role or even the presence of Ga vacancies in GaN.

Defects related to Ga vacancies (V_{Ga}) in GaN are extremely important for optoelectronic applications since they are believed to be the main cause for the nonradiative recombination of carriers [6]. Other scholars have proposed that V_{Ga} are responsible for yellow band luminescence and form nonradiative centres if they are in a complex with donors [7–9]. V_{Ga}-related defects deteriorate the frequency properties of high electron mobility transistors (HEMTs), since trapping and releasing a charge in deep levels is a rather slow process,

decreasing the cut-off frequency. V_{Ga} can also decrease electron channel mobility. Another problem of these defects is shortening of the device lifetime, since vacancies enhance the diffusion of atoms in the structure, which can lead to the decomposition of quantum wells (QWs) [10] or the back-diffusion of Mg atoms from the GaN capping layer through the AlGaN barrier [11,12] to the channel region in HEMT structures. Although V_{Ga} and their complexes are very important defects in nitrides, there is a lack of knowledge about the link between formation of these defects and the technological parameters of the preparation of high-quality epitaxial layers by metalorganic vapor phase epitaxy (MOVPE), as well as the influence of vacancies on semiconductor properties.

2. Materials and Methods

The studied samples were prepared by Aixtron CCS 3 × 2 MOVPE apparatus with dynamic adjustment of showerhead height. The following precursors were used for epitaxy: trimethylgallium (TMGa), triethylgallium (TEGa), and ammonia (NH_3). The set of prepared samples is specified in Table 1.

Table 1. Technological growth conditions of samples prepared for VEPAS measurement.

Samples		Temperature	Precursor
N_2 atmosphere	H_2 atmosphere		
TEN1	TEH1	850 °C	TEGa
TEN2	TEH2	900 °C	TEGa
TEN3	TEH3	950 °C	TEGa
TMN1	TMH1	950 °C	TMGa
TMN2	TMH2	1025 °C	TMGa
TMN3	TMH3	1100 °C	TMGa

Samples were prepared with the aim of finding a link between vacancy formation and some MOVPE technological parameters, namely temperature, type of carrier gas, and type of precursor. Growth of samples was always repeated in both atmospheres, H_2 or N_2. The growth temperature was changed from 850 °C to 1100 °C. TEGa was used for the growth in the temperature range of 850–950 °C; growth at higher temperatures with this precursor was not possible due to strong adduct formation. TMGa was used at the higher temperature range of 950–1100 °C. Growth at lower temperatures from TMGa was avoided due to strong carbon incorporation. Four samples, TEN3, TEH3, TMN1, and TMH1 were prepared at the same temperature (950 °C) to compare only the influence of precursor type. All samples had a 1 µm thick GaN layer prepared with relevant technological parameters. Their simple structure is shown in Figure 1a.

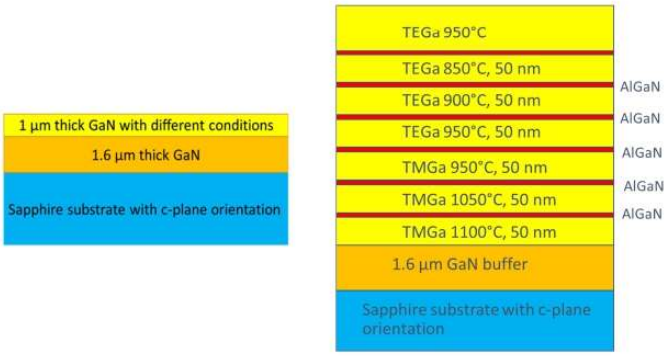

Figure 1. (**a**) Structure of samples prepared for VEPAS and PL measurement, (**b**) Structure of samples prepared for SIMS.

Positron annihilation spectroscopy (PAS) [13,14] is a well-established technique with high sensitivity to vacancies in solids. Positrons emitted by β+ radioisotopes have a continuous energy spectrum with a mean value in the order of hundreds keV. These energetic positrons are therefore called 'fast positrons'. The mean penetration depth of fast positrons into solids is in the order of 10^2–10^3 μm depending on the material density. Consequently, fast positrons can be used for investigations of bulk samples only. For defect studies of thin films, it is necessary to decrease positron energy. This can be achieved by the moderation of fast positrons. A material with negative positron work function [15] can be used as a moderator. A fraction of fast positrons stopped in the moderator diffuses to its surface and escapes into the vacuum due to the negative positron work function. These so called 'slow positrons' are monoenergetic, with an energy of a few eV [16]. Slow positrons are collected in a slow positron beam and guided onto the sample. The energy of slow positrons in the beam can be increased using an electrostatic accelerator. Higher positron energy leads to higher positron penetration depth [16]. Hence, using a variable-energy slow positron beam one can probe the sample from the surface down to various depths. As an example, Figure 2 shows the implantation profiles of positrons with various energies implanted into GaN. The positron implantation profile is well-described by the Makhovian profile [17]. One can see in Figure 2 that varying the energy of slow positrons from 0.5 up to 12 keV enables variation in the mean positron penetration depth into GaN from to 2 to 347 nm. VEPAS is thus well-suited for defect studies of thin films or layered structure. The thickness of GaN films prepared for VEPAS studies is 1 μm (see Figure 1a). Hence, slow positrons are completely stopped inside the GaN layer even for the highest implantation energy of 12 keV used in measurement.

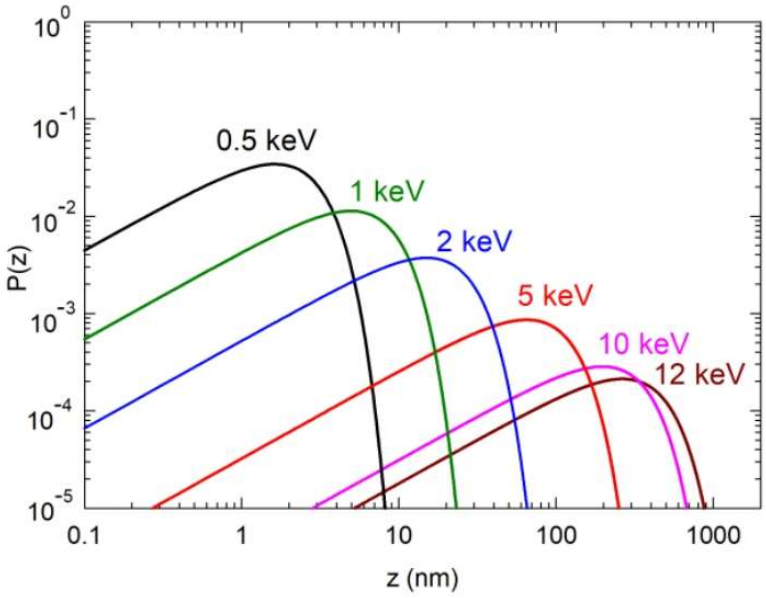

Figure 2. Implantation profiles of positrons with various energies into GaN. Labels indicate positron energy; z denotes the depth from the surface.

Measurement of a positron's lifetime requires a start signal providing a time stamp when a positron was born and a stop signal when the positron was annihilated. The stop signal is given by a 511 keV gamma ray emitted during positron annihilation. In order to obtain the start signal, the positron beam has to be pulsed, i.e., positrons are allowed to appear only in narrow time intervals, providing the start signal. The efficiency of positron moderation is very low ($\leq 5 \times 10^{-3}$) [16] and pulsing of the slow positron beam leads to

further reduction in intensity. As a consequence, a pulsed variable-energy slow positron beam requires a strong positron source.

VEPAS studies in the present paper were carried out on a LINAC-based pulsed variable energy slow positron beam MePS [18] operating at the ELBE facility [19] at Helmholtz-Zentrum Dresden-Rossendorf. Primary fast positrons were created by pair production induced by electron bremsstrahlung radiation. A tungsten moderator was used to obtain slow positrons. A high-intensity LINAC electron beam (average electron beam current 1.6 mA, electron energy 35 MeV) enabled achieving a high intensity of fast positrons necessary for a pulsed slow positron beam. Moreover, narrow electron pulses of ELBE LINAC (width smaller than 10 ps) were used as start signals for precise measurement of positron lifetimes. The annihilation gamma rays providing stop signals were measured using a $CeBr_3$ scintillation detector with digital signal processing. The time resolution of the spectrometer (FWHM of the resolution function) was 230 ps. The energy of slow positrons could be varied in the range from 0.5 to 12 keV.

Photoluminescence (PL) spectra of samples were collected using 325 nm excitation wavelength and a confocal microscope (LabRAM HR Evolution HORIBA, He–Cd laser, objective 74 CG, detector Synapse UV).

Two samples were also prepared for secondary ion mass spectroscopy (SIMS) measurement to study the connection between the contamination of layers and the technology of their preparation (see Figure 1b). These samples contained GaN layers with relevant technological parameters, with a thickness of 50 nm separated by 10 nm thick AlGaN layers that served as markers. All examined layers of the first and second sample were grown in H_2 and N_2 atmospheres, respectively. The concentrations of common contaminants (C, O, H, Si) were measured in EAG laboratories [20].

3. Results and Discussion

3.1. Variable Energy Positron Annihilation Spectroscopy

A positron lifetime spectrum is in general a sum of exponential components convoluted with the response function of the spectrometer. Each component corresponds to a certain positron state and is characterized by its lifetime τ_i and relative intensity I_i. A single-component fit of positron lifetime spectra yields the mean positron lifetime, representing the weighted average of lifetimes of various components, $\overline{\tau} = \sum_i \tau_i I_i$. An example of a single-component fit of positron lifetime spectrum for the TEH1 sample for positron energy E = 10 keV is shown in Figure 3a. The mean positron lifetime is a robust parameter not affected by mutual correlations among fitting parameters and provides useful information about trends in the series of GaN films studied. The mean positron lifetime for GaN layers studied is plotted in Figure 4 as a function of the positron energy. At low energies, almost all positrons are annihilated on the surface and the mean positron lifetime corresponds to the surface state. With increasing energy, positrons penetrate deeper into the GaN layer and the fraction of positrons diffusing back to the surface gradually decreases. Consequently, the mean positron lifetime gradually decreases with increasing positron energy from the surface value down to a value corresponding to when all positrons are annihilated in the GaN layer.

Positrons are attracted and captured by negatively charged Ga vacancies (V_{Ga}). In the empty volume of a V_{Ga}, positrons have lower overlap with the electrons of crystal atoms, which decreases the probability of their annihilation and, hence, the lifetime of positrons trapped in the vacancy is increased. Figure 4 also shows the calculated lifetime values of free positrons in a perfect GaN crystal without defects (bulk) as well as that of positrons trapped in V_{Ga} and of positrons trapped in different clusters with nitrogen vacancies (V_N). Positron lifetime increased with increased empty volume in the defect. Positrons annihilated on the surface influenced the measured mean lifetime values up to the mean penetration depth of 200–300 nm due to the back-diffusion of positrons toward the surface. For higher penetration depths, i.e., incident positron energy above 8 keV, the fraction of positrons diffusing back to the surface becomes negligible and almost all

positrons are annihilated in the GaN layer. The mean positron lifetime values for energies above 8 keV were, therefore, supposed to be relevant for determination of defect type and concentration.

From inspection of Figure 4, one can conclude that the mean positron lifetime at high energies (E > 8 keV) approaches values located between the calculated bulk positron lifetime (i.e., lifetime of free positrons in a defect-free lattice) and the calculated lifetime of positrons trapped in V_{Ga}. This indicates that GaN films contain V_{Ga}, and some positrons are trapped and annihilated in V_{Ga} while the remaining positrons are annihilated in the free state, i.e., not trapped at defects. The only exception comprises TMN3 and TMH3 samples grown at the highest temperature of 1100 °C. In TMN3 and TMH3, the mean positron lifetime at high energies approached a value that was higher than the calculated lifetime for V_{Ga}. This indicates that TMN3 and TMH3 contain defects with a higher open volume than V_{Ga}.

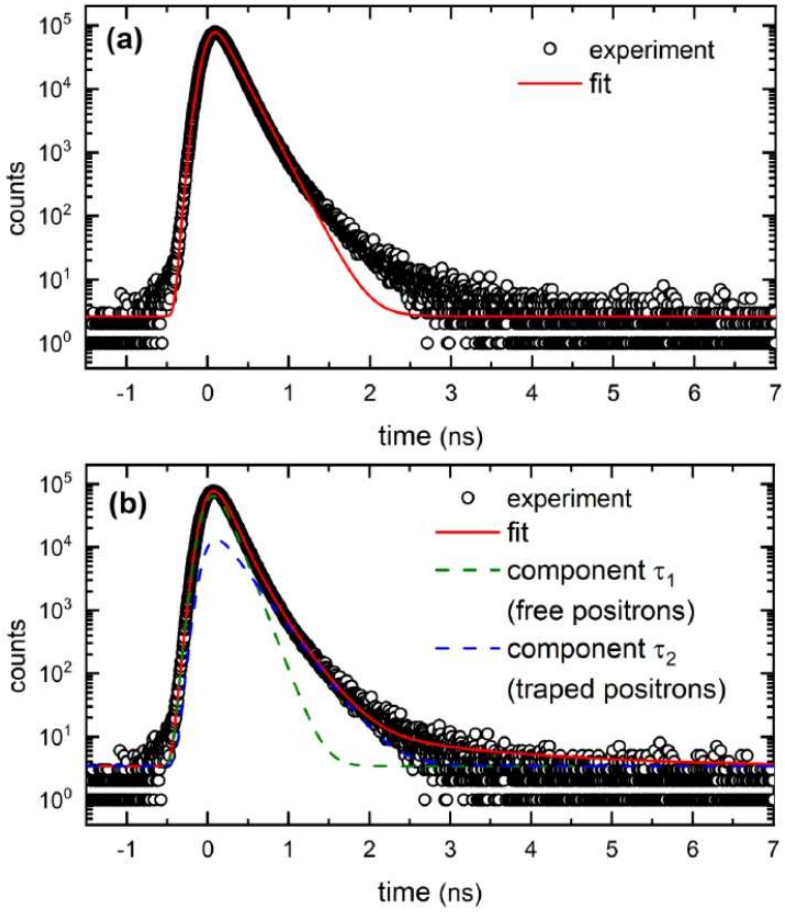

Figure 3. An example of positron lifetime spectrum measured for the TEH1 sample and energy of incident positrons E = 10 keV. Solid line shows fit of the spectrum by model function. (**a**) Single-component fit yielding the mean positron lifetime; (**b**) Two-component fit considering contribution of free positrons (lifetime τ_1) and positrons trapped at defects (lifetime τ_2). Individual components are plotted by dashed lines.

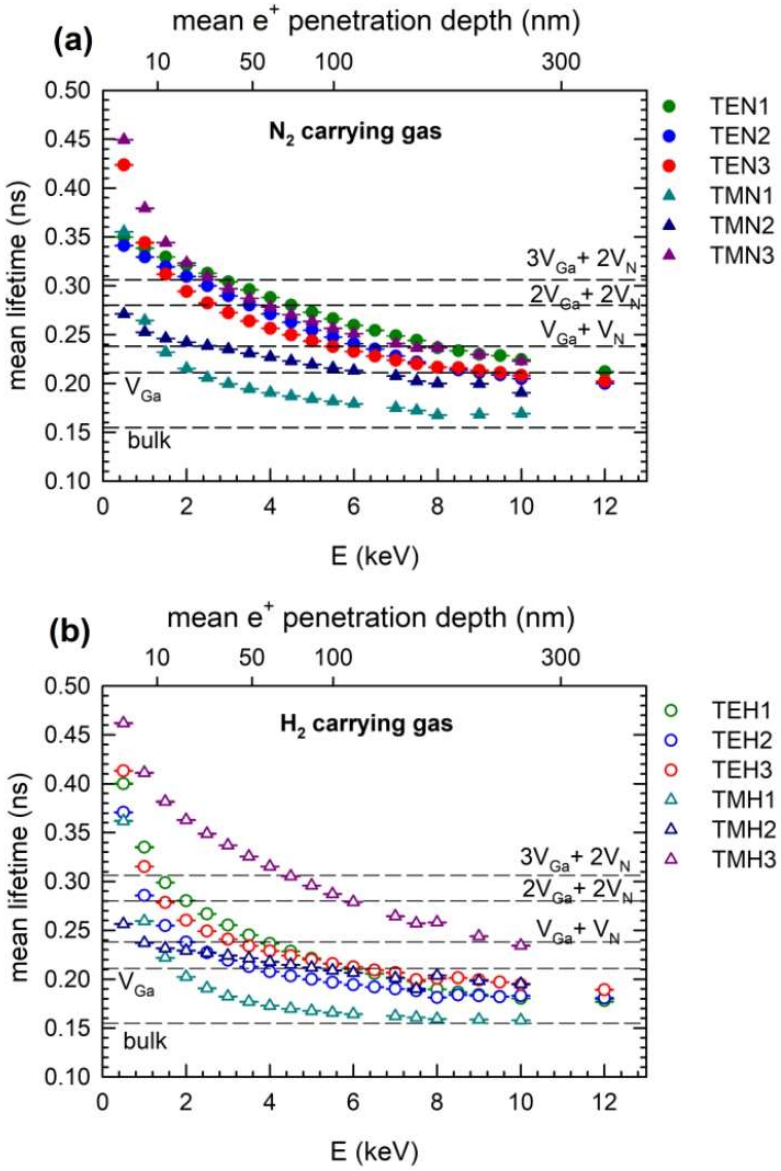

Figure 4. Dependence of the mean positron lifetime on the energy of incident positrons entering the GaN layer prepared under different growth conditions in (**a**) nitrogen and (**b**) hydrogen atmosphere. Upper *x*-axis shows the mean positron penetration depth.

An example of the decomposition of the positron lifetime spectra for the TEH1 sample and the energy of incident positrons E = 10 keV is shown in Figure 3b. From comparison of Figure 3a to Figure 3b it is clear that fitting by two components results in better agreement with experimental points than the single-component fit. The development of positron lifetimes τ_1 and τ_2 and corresponding intensities I_1 and I_2 for sample TEH1 with positron energy is shown in Figures 5a and 5b, respectively. It can be noticed that for penetration depth 300 nm, the positron lifetime τ_2 reached the value calculated for positrons trapped in V_{Ga}, testifying that the TEH1 sample contains V_{Ga}. Results of the breakdown of positron lifetime spectra for other samples are collected in Supplementary Materials. Similar results

as for TEH1 were also obtained for other GaN films deposited at temperatures below 1100 °C. The results of the decomposition of positron lifetime spectra for the TMH3 sample deposited at 1100 °C are plotted in Figure 6. In contrast to the films deposited at lower temperatures, the lifetime τ_2 for the TMH3 sample at high energies approaches a significantly higher value, corresponding to the calculated lifetime of positrons trapped in a complex consisting of two Ga and two N missing ions ($2V_{Ga}+2V_N$ complex). A similar result was obtained for TMN3 film deposited at 1100 °C using N_2 carrying gas (see Supplementary Materials). The development of the lifetime τ_2 measured at the highest positron energy of 12 keV on different GaN film deposition temperatures is plotted in Figure 7a. For deposition temperatures lower than 1100 °C, the lifetime τ_2 remains close to the calculated value for V_{Ga}. However, for films deposited at 1100 °C the lifetime τ_2 increases to the value corresponding to a $2V_{Ga} + 2V_N$ complex. Thus, one can conclude that GaN films grown at temperatures below 1100 °C contain V_{Ga}. However, at higher temperatures the nature of the defects changes and films grown at 1100 °C contain $2V_{Ga} + 2V_N$ complexes.

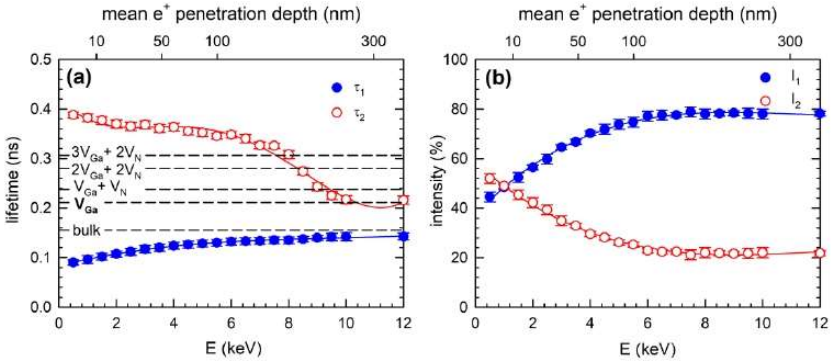

Figure 5. Breakdown results of positron lifetime spectra for sample TEH1 (**a**) lifetimes τ_1 and τ_2 of components resolved in spectra and (**b**) intensities I_1 and I_2 of the components. Dashed lines indicate calculated bulk positron lifetime and lifetimes of positrons trapped in various defects. The mean positron penetration depth is shown in the upper *x*-axis. The solid lines serve to guide the eye.

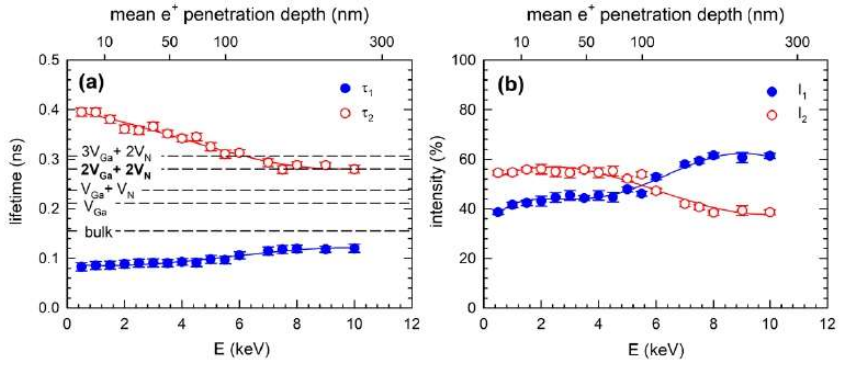

Figure 6. Results of breaking down positron lifetime spectra for the TMH3 sample (**a**) lifetimes τ_1 and τ_2 of the components resolved in spectra and (**b**) intensities I_1 and I_2 of the components. Dashed lines indicate calculated bulk positron lifetime and the lifetimes of positrons trapped in various defects. The mean positron penetration depth is shown in the upper *x*-axis. The solid lines serve to guide the eye.

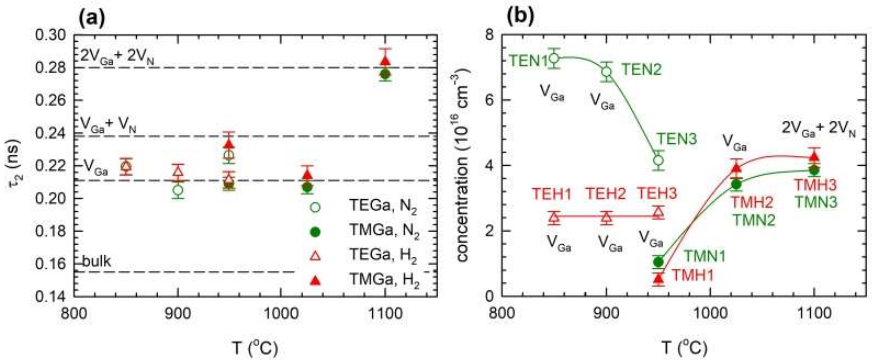

Figure 7. (**a**) The development of the lifetime τ_2 measured for the energy of incident positrons of 12 keV on different film deposition temperatures; (**b**) the concentration of V_{Ga} determined by VEPAS for samples prepared with growth parameters defined in Table 1. Labels indicate notation of sample and dominant type of defects in the sample. Solid lines are plotted to guide eyes only.

The V_{Ga} concentration was calculated from the lifetimes and intensities of both components using the two-state trapping model [21]. Data measured for the highest positron energy of 12 keV corresponding to the highest positron penetration depth were used for determination of the vacancy concentration for all samples. Results for all samples are summarized in Figure 7b. V_{Ga} formation is not only influenced by the temperature, but it is also strongly dependent on the choices of precursor and carrier gas. The temperature dependence of V_{Ga} concentration for samples grown from TEGa and TMGa precursors have opposite characters. Unfortunately, there was not sufficient overlap of temperature intervals in which both precursors could be used for epitaxy; only around 950 °C could both types of precursors be used. TEGa is preferred for temperatures below 950 °C, since at this temperature range TMGa is less decomposed and too much carbon would be incorporated into the layers. At temperatures above 950 °C, TEGa cannot be used due to adduct formation, which impacts the growth rate.

Very characteristic of layers grown from TEGa is that the measured V_{Ga} concentration is significantly higher in a nitrogen atmosphere compared to samples grown in hydrogen. In the case of TEGa grown in nitrogen, V_{Ga} concentration decreases with temperature. This is unexpected from a thermodynamic point of view, since the vacancy concentration should be increasing with temperature as exp ($-E_f/kT$), where E_f is the vacancy formation energy [22]. Several possible hypotheses explaining this behaviour can be suggested. Since the TEGa precursor should be fully decomposed in the studied temperature range [23], limited Ga precursor decomposition can be ruled out. One of the possible explanations is the influence of surface morphology on vacancy formation, because in a N_2 atmosphere the epitaxial surface is rather rough (V-shape defects are formed). A lower V_{Ga} concentration in a H_2 atmosphere can be due to passivation or filling of V_{Ga} by hydrogen incorporated in the GaN lattice. In complexes of V_{Ga} associated with H atoms positrons cannot be trapped or their lifetime is much shorter. For comparison, the lifetime of a positron trapped in a V_{Ga} is 200–211 ps, while positron lifetime for V_{Ga}-H complexes is shortened to 180 ps and for V_{Ga}-2H it is further shortened to 150 ps, so it is even shorter than 155 ps, which is the bulk positron lifetime for GaN, i.e., lifetime of free positrons in a perfect (defect-free) GaN crystal [24].

When TMGa is used as the precursor, V_{Ga} concentration is not influenced by the choice of atmosphere in the MOVPE reactor, but it is strongly enhanced with increasing temperature. The lifetime corresponding to a cluster $2V_{Ga}$–$2V_N$ was measured for the highest growth temperature of 1100 °C, which means that the actual V_{Ga} concentration was twice the concentration of $2V_{Ga}$–$2V_N$ complexes shown in Figure 7b, since each complex contains two V_{Ga}. Significantly different V_{Ga} concentration when TMGa or TEGa was used for the GaN growth suggests that the reaction pathway has important influence on the

vacancy formation. This could be a reason why theoretical predictions of V_{Ga} concentration based on formation energy [25] are underestimated. In the future, layers grown from novel precursors and the vacancy formation in them might help to understand the growth kinetics, as suggested in [26,27].

3.2. Photoluminescence

Knowing the V_{Ga} concentration in particular GaN layers, we investigated its correlation with PL properties. It could bring valuable insight into the quest for yellow band (YB) luminescence origin. In previous works, YB luminescence was attributed to a C_N defect [28], C_N-O_N complex [29], which is energetically favourable, or C_N-Si_{Ga} [30] in n-type GaN layers. Other sources of YB luminescence that were proposed in the literature were V_{Ga}-3H and V_{Ga}-O_N-2H complexes [31] or V_{Ga}-O_N [32]. V_{Ga} were also supposed to be responsible for nonradiative recombination [6].

Typical room-temperature PL spectra for MOVPE-prepared GaN layers (samples TEN1 and TEH1) are shown in Figure 8 to illustrate the position of PL bands. Contrary to expectations, for sample TEN1, with a higher V_{Ga} concentration, neither an increase in YB intensity nor a decrease of PL efficiency was observed.

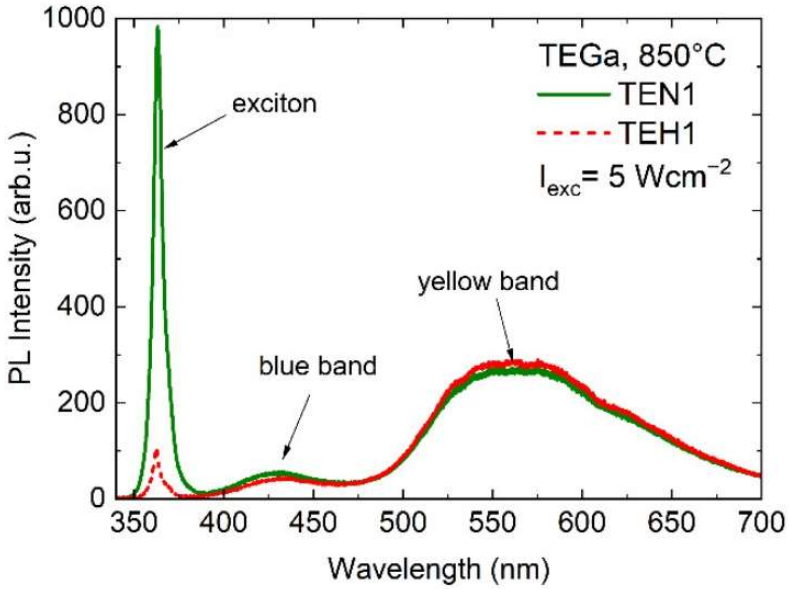

Figure 8. Room-temperature photoluminescence spectra of samples TEN1 and TEH1.

In Figure 9a,b, correlation between excitonic and YB intensity with respect to the V_{Ga} concentration is shown, summarizing the data obtained from all studied layers. No correlation between V_{Ga} concentration and YB luminescence intensity was observed, which suggests that V_{Ga} are not the dominant reason for YB luminescence.

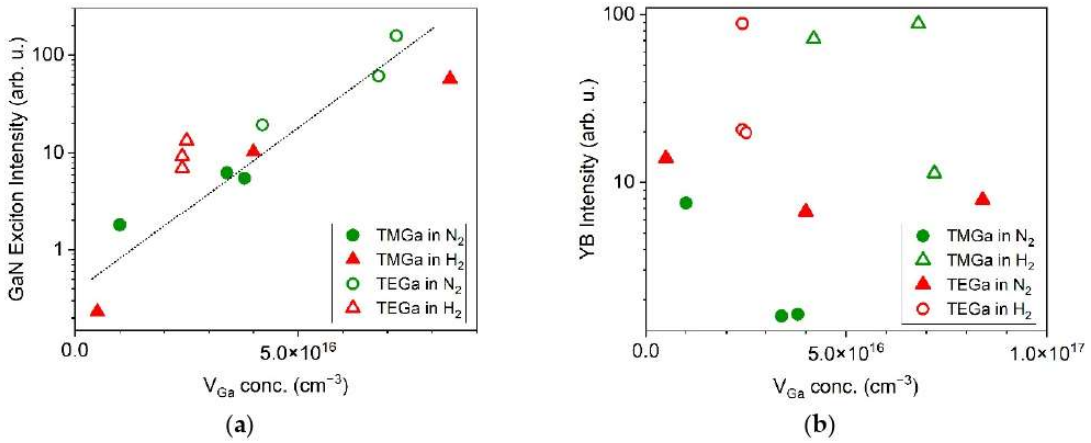

Figure 9. Maximum intensity of (**a**) excitonic and (**b**) yellow band luminescence as a function of V_{Ga} concentration.

However, there is unexpected and clear positive correlation between V_{Ga} concentration and excitonic luminescence. It means that V_{Ga} cannot be efficient nonradiative centre. Since there is no known mechanism in which V_{Ga} presence would enhance free-exciton emission in GaN, we suggest the following explanation for the correlation observed in Figure 9a: higher exciton intensity is caused by the suppression of other recombination channels, especially the nonradiative ones (because enhancement of yellow luminescence was not observed with increasing V_{Ga} concentration, Figure 9b). Correlation between V_{Ga} concentration and GaN exciton intensity means that there exists an anticorrelation between nonradiative centre concentration and V_{Ga} concentration. In other words, the formation of an unknown nonradiative centrum is suppressed when the Ga vacancies are present.

3.3. Secondary Ion Mass Spectroscopy

To find possible candidates for nonradiative defects that are anticorrelated with V_{Ga} and to elucidate whether V_{Ga} form complexes with atoms from impurities, we prepared multilayer samples designed for SIMS characterization according to the scheme in Figure 1b. Hydrogen, oxygen, carbon, and silicon concentration profiles were measured by SIMS. There was one significant feature observed in all GaN layers—contamination from all four elements was higher when H_2 was used for the reactor atmosphere. Interesting correlations between V_{Ga} and carbon for samples grown from TMGa, and between V_{Ga} and hydrogen for samples grown from TEGa were observed. The obtained hydrogen and carbon concentrations for GaN layers prepared according to the above-defined technological parameters are summarized in Figure 10a,b.

In layers grown in a H_2 atmosphere at lower temperatures, hydrogen contamination was approximately three times higher than for samples grown in a N_2 atmosphere. We suppose that NH_3 is less efficiently decomposed in a H_2 atmosphere and hydrogen could be incorporated into the epitaxial layer. Hydrogen can form complexes with V_{Ga} that are invisible to PAS methods, as was explained above. Since in samples grown from TEGa in a H_2 atmosphere the oxygen concentration measured by SIMS was in the order of 10^{17} cm^{-3} (not shown here), we can also suppose the formation of V_{Ga}-O_N-2H, which is energetically favourable. In fact, if H and O are abundant, formation of V_{Ga}-3H, V_{Ga}-2H, or V_{Ga}-O_N-2H complexes is much more probable than formation of isolated V_{Ga}. The smallest formation energy of V_{Ga} is found when the Fermi level is near the conduction band minimum but still reaches a value around 4.5 eV. On the other hand, at the same Fermi level position, the formation energy of V_{Ga}-3H, V_{Ga}-2H, and V_{Ga}-O_N-2H is around 3 eV, 2.6 eV, and 0.5 eV, respectively [33]. Since none of these defects can be detected by VEPAS due to the small

open volume of the defects, their presence may explain the significantly lower detected V_{Ga} concentration in layers grown from TEGa in a H_2 atmosphere. Some of these defects probably also act as nonradiative centres [33].

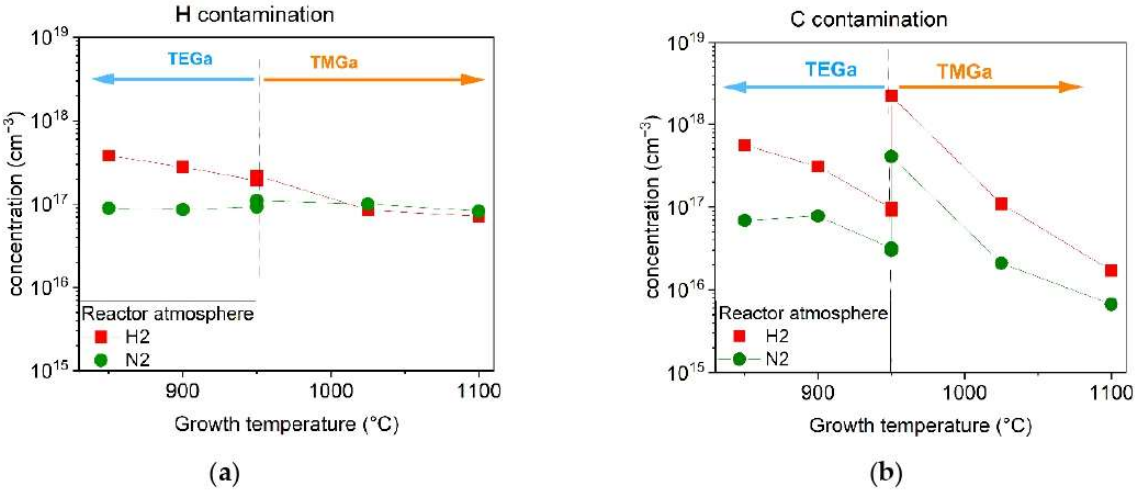

Figure 10. Concentration of (**a**) hydrogen and (**b**) carbon contamination measured by SIMS on layers prepared on multi-layered samples with technological parameters as defined in Table 1.

However, in samples grown from TMGa, hydrogen does not play a significant role. Instead, carbon contamination seems to be anticorrelated with V_{Ga} concentration. It seems that for the lowest temperature of 950 °C, the carbon concentration is so high that it is filling not only V_N, but also V_{Ga}, thus forming n-type C_{Ga} defects. On the other hand, at the highest temperature, when there is low carbon contamination, both types of vacancies remain unfilled and their concentration is so high that they can merge into clusters, as was observed at 1100 °C. According to the PL results, at the highest carbon concentration PL efficiency drops significantly, suggesting the formation of strong nonradiative defects, which could be C_{Ga} according to [34], or it may be due to some complex related to C_{Ga} such as C_{Ga}-C_N or C_{Ga}-H_i.

4. Conclusions

Twelve samples with GaN layers prepared by MOVPE under different technological conditions were investigated by a unique VEPAS method to find a link between technological conditions and V_{Ga} formation. Different correlations between V_{Ga} concentration and technology parameters were observed for layers grown from TEGa and TMGa precursors. In the case of TEGa, V_{Ga} formation was significantly influenced by the type of reactor atmosphere (N_2 or H_2), while no similar behaviour was observed for samples grown from TMGa. V_{Ga} formation was suppressed with increasing temperature for growth from TEGa in a N_2 atmosphere. On the contrary, opposite temperature dependence for V_{Ga} formation was observed for growth from TMGa, with cluster formation for the highest temperature of 1100 °C. Significantly different V_{Ga} formation when TMGa or TEGa was used for the GaN growth suggests that the reaction mechanism has an important influence on formation of vacancies. This could be a reason why V_{Ga} concentrations theoretically predicted from formation energies are underestimated. According to the correlation of PL results with V_{Ga} concentrations determined by VEPAS, it can be concluded that YB luminescence is not generally connected with V_{Ga} in MOVPE-prepared GaN layers. Surprisingly, the presence of V_{Ga} was correlated with intensity of excitonic luminescence. The probable explanation is that the V_{Ga} concentration in GaN layers is anticorrelated with some efficient nonradiative defects. According to SIMS results and correlation with detected V_{Ga} concentrations, we

have suggested several candidates for such nonradiative defects, which could be C_{Ga}, C_{Ga}-C_N, or C_{Ga} -H_i in samples grown from TMGa and V_{Ga}-3H, V_{Ga}-2H, or V_{Ga}-O_N-2H complexes in samples grown from TEGa.

Supplementary Materials: The following supporting information can be downloaded at: https://www.mdpi.com/article/10.3390/ma15196916/s1, Figure S1: Results of decompositions of positron lifetime spectra for the sample TEN1 plotted as a function of the energy of incident positrons. Figure S2: Results of decompositions of positron lifetime spectra for the sample TEN2 plotted as a function of the energy of incident positrons. Figure S3: Results of decompositions of positron lifetime spectra for the sample TEN3 plotted as a function of the energy of incident positrons. Figure S4: Results of decompositions of positron lifetime spectra for the sample TEH1 plotted as a function of the energy of incident positrons. Figure S5: Results of decompositions of positron lifetime spectra for the sample TEH2 plotted as a function of the energy of incident positrons. Figure S6: Results of decompositions of positron lifetime spectra for the sample TEH3 plotted as a function of the energy of incident positrons. Figure S7: Results of decompositions of positron lifetime spectra for the sample TMN1 plotted as a function of the energy of incident positrons. Figure S8: Results of decompositions of positron lifetime spectra for the sample TMN2 plotted as a function of the energy of incident positrons. Figure S9: Results of decompositions of positron lifetime spectra for the sample TMN3 plotted as a function of the energy of incident positrons. Figure S10: Results of decompositions of positron lifetime spectra for the sample TMH1 plotted as a function of the energy of incident positrons. Figure S11: Results of decompositions of positron lifetime spectra for the sample TMH2 plotted as a function of the energy of incident positrons. Figure S12: Results of decompositions of positron lifetime spectra for the sample TMH3 plotted as a function of the energy of incident positrons. References [35,36] are cited in the supplementary materials.

Author Contributions: Conceptualization, A.H., J.Č., F.H. and T.H.; methodology, J.Č., F.H., K.K., F.D., J.P. and T.H.; formal analysis, J.Č. and F.H.; investigation, J.Č., A.H., F.H., K.K., F.D., T.H., J.B., M.O.L., M.B., E.H. and A.W.; writing—original draft preparation, A.H., J.Č. and F.H.; writing—review and editing, J.Č., A.H., K.K., J.P., J.B., F.D. and T.H.; visualization, J.Č. and A.H.; project administration, J.Č. and A.H.; funding acquisition, A.H. and J.Č. All authors have read and agreed to the published version of the manuscript.

Funding: This research was funded by the Czech Science Foundation, project GACR LA 22-28001K (VACCINES), CAS mobility project PAN-20-19 and MEYS CR Czech Nanolab infrastructure LM2018110. Parts of this research were carried out at ELBE at the Helmholtz-Zentrum Dresden-Rossendorf e. V., a member of the Helmholtz Association. We would like to thank the facility staff (X) for assistance. Partial support from the Operational Programme Research, Development and Education financed by European Structural and Investment Funds and the Czech MEYS (Project No. SOLID21 CZ.02.1.01/0.0/0.0/16_019/0000760 is also acknowledged).

Institutional Review Board Statement: Not applicable.

Informed Consent Statement: Not applicable.

Data Availability Statement: Measured data can be provided upon request from hospodko@fzu.cz.

Conflicts of Interest: The authors declare no conflict of interest.

References

1. Nakamura, S. Nobel Lecture: Background story of the invention of efficient blue InGaN light emitting diodes. *Rev. Mod. Phys.* **2015**, *87*, 1139–1151. [CrossRef]
2. Mishra, U.K.; Parikh, P.; Wu, Y.F. AlGaN/GaN HEMTs—An overview of device operation and applications. *Proc. IEEE* **2002**, *90*, 1022–1031. [CrossRef]
3. Li, D.B.; Sun, X.J.; Song, H.; Li, Z.M.; Chen, Y.R.; Jiang, H.; Miao, G. Q Realization of a high-performance GaN UV detector by nanoplasmonic enhancement. *Adv. Mater.* **2012**, *24*, 845–849. [CrossRef] [PubMed]
4. Neufeld, C.J.; Toledo, N.G.; Cruz, S.C.; Iza, M.; DenBaars, S.P.; Mishra, U.K. High quantum efficiency InGaN/GaN solar cells with 2.95 eV band gap. *Appl. Phys. Lett.* **2008**, *93*, 143502. [CrossRef]
5. Hospodková, A.; Nikl, M.; Pacherová, O.; Oswald, J.; Brůža, P.; Pánek, D.; Foltynski, B.; Hulicius, E.; Beitlerová, A.; Heuken, M. InGaN/GaN multiple quantum well for fast scintillation application: Radioluminescence and photoluminescence study. *Nanotechnology* **2014**, *25*, 455501. [CrossRef]

6. Nykanen, H.; Suihkonen, S.; Kilanski, L.; Sopanen, M.; Tuomisto, F. Low energy electron beam induced vacancy activation in GaN. *Appl. Phys. Lett.* **2012**, *69*, 122105. [CrossRef]
7. Neugebauer, J.; Van de Walle, C.G. Gallium vacancies and the yellow luminescence in GaN. *Appl. Phys. Lett.* **1996**, *69*, 503–505. [CrossRef]
8. Saarinen, K.; Laine, T.; Kuisma, S.; Nissila, J.; Hautojarvi, P.; Dobrzynski, L.; Baranowski, J.M.; Pakula, K.; Stepniewski, R.; Wojdak, M.; et al. Observation of native Ga vacancies in GaN by positron annihilation. *Phys. Rev. Lett.* **1997**, *79*, 3030–3033. [CrossRef]
9. Lyons, J.L.; Van de Walle, C.G. Computationally predicted energies and properties of defects in GaN. *NPJ Comput. Mater.* **2017**, *3*, 12. [CrossRef]
10. Bojarska, A.; Muziol, G.; Skierbiszewski, C.; Grzanka, E.; Wisniewski, P.; Makarowa, I.; Czernecki, R.; Suski, T.; Perlin, P. Influence of the growth method on degradation of InGaN laser diodes. *Appl. Phys. Express* **2017**, *10*, 091001. [CrossRef]
11. Gutt, R.; Kohler, K.; Wiegert, J.; Kirste, L.; Passow, T.; Wagner, J. Controlling the Mg doping profile in MOVPE-grown GaN/$Al_{0.2}Ga_{0.8}N$ light-emitting diodes. *Phys. Status Solidi C* **2011**, *8*, 2072–2074. [CrossRef]
12. Chichibu, S.F.; Uedono, A.; Kojima, K.; Ikeda, H.; Fujito, K.; Takashima, S.; Edo, M.; Ueno, K.; Ishibashi, S. The origins and properties of intrinsic nonradiative recombination centers in wide bandgap GaN and AlGaN. *J. Appl. Phys.* **2018**, *123*, 161413. [CrossRef]
13. Krause-Rehberg, R.; Leipner, H. *Positron Annihilation in Semiconductors: Defect Studies*, 1st ed.; Springer: Berlin, Germany, 1999.
14. Čížek, J. Characterization of lattice defects in metallic materials by positron annihilation spectroscopy: A review. *J. Mater. Sci. Technol.* **2018**, *34*, 577–598. [CrossRef]
15. Schultz, P.; Lynn, K.G. Interaction of positron beams with surfaces, thin films, and interfaces. *Rev. Mod. Phys.* **1988**, *60*, 701–801. [CrossRef]
16. Hugenschmidt, C. Positrons insurface physics. *Surf. Sci. Rep.* **2016**, *71*, 547–594. [CrossRef]
17. Puska, M.J.; Nieminen, R.J. Theory of positrons in solids and on solid surfaces. *Rev. Mod. Phys.* **1994**, *66*, 841–899. [CrossRef]
18. Wagner, A.; Butterling, M.; Liedke, M.O.; Potzger, K.; Krause-Rehberg, R. Positron Annihilation Lifetime and Doppler Broadening Spectroscopy at the ELBE Facility. *AIP Conf. Proc.* **1980**, *1970*, 40003. [CrossRef]
19. Gabriel, F.; Gippner, P.; Grosse, E.; Janssen, D.; Michel, P.; Prade, H.; Schamlott, A.; Seidel, W.; Wolf, A.; Wünsch, R. The Rossendorf radiation source ELBE and its FEL projects. *Nucl. Instrum. Methods Phys. Res. Sect. B* **2000**, *161*, 1143–1147. [CrossRef]
20. The Global Leader in Materials Testing Services. EAG Laboratories. Available online: https://www.eag.com/ (accessed on 21 October 2021).
21. West, R.N. Positron studies of condensed matter. *Adv. Phys.* **1973**, *22*, 263–383. [CrossRef]
22. Mendelev, M.I.; Bokstein, B.S. Molecular dynamics study of self-diffusion in Zr. *Philos. Mag.* **2010**, *90*, 637–654. [CrossRef]
23. Xing, G.; Ye, Z.Z. Selection of precursors and their influences on III-nitrides grown by MOCVD. *J. Microw. Optoelectron. Electromagn. Appl.* **2002**, *2*, 1–16.
24. Hautakangas, S.; Makkonen, I.; Ranki, V.; Puska, J.; Saarinen, K.; Xu, X.; Look, D.C. Direct evidence of impurity decoration of Ga vacancies in GaN from positron annihilation spectroscopy. *Phys. Rev. B* **2006**, *73*, 163301. [CrossRef]
25. Xie, Z.J.; Sui, Y.; Buckeridge, J.; Catlow, C.R.A.; Keal, T.W.; Sherwood, P.; Walsh, A.; Farrow, M.R.; Scanlon, D.O.; Woodly, S.M.; et al. Donor and acceptor characteristics of native point defects in GaN. *J. Phys. D Appl. Phys.* **2019**, *52*, 335104. [CrossRef]
26. dos Santos, R.B.; Rivelino, R.; Mota, F.D.; Kakanakova-Georgieva, A.; Gueorguiev, G.K. Feasibility of novel $(H_3C_{)(n)}X(SiH_3)_{(3-n)}$ compounds (X = B, Al, Ga, In): Structure, stability, reactivity, and Raman characterization from ab initio calculations. *Dalton Trans.* **2015**, *44*, 3356–3366. [CrossRef]
27. Freitas, R.R.Q.; Gueorguiev, G.K.; Mota, F.D.; de Castilho, C.M.C.; Stafstrom, S.; Kakanakova-Georgieva, A. Reactivity of adducts relevant to the deposition of hexagonal BN from first-principles calculations. *Chem. Phys. Lett.* **2013**, *583*, 119–124. [CrossRef]
28. Lyons, J.L.; Janotti, A.; Van de Walle, C.G. Carbon impurities and the yellow luminescence in GaN. *Appl. Phys. Lett.* **2010**, *97*, 152108. [CrossRef]
29. Demchenko, D.O.; Diallo, I.C.; Reshchikov, M.A. Yellow Luminescence of Gallium Nitride Generated by Carbon Defect Complexes. *Phys. Rev. Lett.* **2013**, *110*, 87404. [CrossRef]
30. Christenson, S.G.; Xie, W.Y.; Sun, Y.Y.; Zhang, S.B. Carbon as a source for yellow luminescence in GaN: Isolated C-N defect or its complexes. *J. Appl. Phys.* **2015**, *118*, 135708. [CrossRef]
31. Lyons, J.L.; Alkauskas, A.; Janotti, A.; Van de Walle, C.G. First-principles theory of acceptors in nitride semiconductors. *Phys. Status Solidi B* **2015**, *252*, 900–908. [CrossRef]
32. Xie, Z.J.; Sui, Y.; Buckeridge, J.; Sokol, A.A.; Keal, T.W.; Walsh, A. Prediction of multiband luminescence due to the gallium vacancy-oxygen defect complex in GaN. *Appl. Phys. Lett.* **2018**, *112*, 262104. [CrossRef]
33. Dreyer, C.E.; Alkauskas, A.; Lyons, J.L.; Speck, J.S.; Van de Walle, C.G. Gallium vacancy complexes as a cause of Shockley-Read-Hall recombination in III-nitride light emitters. *Appl. Phys. Lett.* **2016**, *108*, 141101. [CrossRef]
34. Zimmermann, F.; Beyer, J.; Roder, C.; Beyer, F.C.; Richter, E.; Irmscher, K.; Heitmann, J. Current Status of Carbon-Related Defect Luminescence in GaN. *Phys. Status Solidi A* **2021**, *218*, 2100235. [CrossRef]
35. Čížek, J. PLRF Code for Decomposition of Positron Lifetime Spectra. *Acta Phys. Pol. A* **2020**, *137*, 177–187. [CrossRef]
36. Mogensen, O.E. *Positron Annihilation Chemistry*, 1st ed.; Springer: Berlin, Germany, 1995.

Journal of Crystal Growth 536 (2020) 125579

Contents lists available at ScienceDirect

Journal of Crystal Growth

journal homepage: www.elsevier.com/locate/jcrysgro

A secret luminescence killer in deepest QWs of InGaN/GaN multiple quantum well structures

A. Hospodková[a,*], F. Hájek[a], J. Pangrác[a], M. Slavická Zíková[a], T. Hubáček[a,b], K. Kuldová[a], J. Oswald[a], T. Vaněk[a,b], A. Vetushka[a], J. Čížek[c], M.O. Liedke[d], M. Butterling[d], A. Wagner[d]

[a] Institute of Physics CAS, v.v.i., Cukrovarnická 10, CZ-16200 Prague 6, Czech Republic
[b] Faculty of Mechatronics, Informatics and Interdisciplinary Studies, Technical University of Liberec, Studentská 2, CZ-46117 Liberec, Czech Republic
[c] Faculty of Mathematics and Physics, Charles University, V Holešovičkách 2, 18000 Praha 8, Czech Republic
[d] Institute of Radiation Physics, Helmholtz-Zentrum Dresden-Rossendorf Bautzner Landstr. 400, 01328 Dresden, Germany

ARTICLE INFO

Communicated by R. Bhat

Keywords:
A3. Quantum wells
A1. Defects
A1. Impurities
A3. Metalorganic vapor phase epitaxy
B1. Nitrides

ABSTRACT

This work suggests new alternative explanation why a single InGaN quantum well (QW) or the deepest QWs in the multiple quantum well (MQW) structures suffer with a high non-radiative recombination rate. According to SIMS results, positron annihilation spectroscopy and photoluminescence measurements we suggest that vacancy of Ga in complex with hydrogen atoms can play a dominant role in non-radiative Shockley-Read-Hall recombination of the deepest QWs in InGaN/GaN MQW structures. Vacancy of gallium originate dominantly in GaN buffer layers grown at higher temperatures in H_2 atmosphere and are transported to the InGaN/GaN MQW region by diffusion, where they are very effectively trapped in InGaN layers and form complex defects with hydrogen atoms during epitaxy of InGaN layers. Trapping of gallium vacancies is another suggested mechanism explaining why the widely used In containing prelayers help to increase the luminescence efficiency of the InGaN/GaN MQW active region grown above them. Understanding the mechanism why the luminescence efficiency is suppressed in deeper QWs may be very important for LED community and can help to develop new improved technologies for the growth of InGaN/GaN MQW active region.

1. Introduction

Although InGaN/GaN multiple quantum well (MQW) structures are widely used for light emitting and laser diodes (LEDs and LDs) for more than two decades, there are still some not answered questions. One of them is a strong luminescence efficiency of InGaN/GaN MQW structure despite a high dislocation density [1], which is often in the order of 10^9 cm^{-2}. Different explanations such as random alloy fluctuation of InGaN inducing potential fluctuation and hindering carriers from migration towards non-radiative centers (NRCs) [2,3] were suggested. Other accepted explanation is a formation of quasi barriers around dislocations caused by thinning QW width in V-pit walls, suggested by Hangleiter [4]. These quasi barriers in V-pits help to separate carriers confined in InGaN QWs from dislocations which are situated in the center of V-pits suppressing thus the non-radiative recombination rate. These V-pits open during the epitaxy at lower temperature and with N_2 used as a carrier gas [5]. It was shown that the optimal diameter of V-pits to reach the maximum efficiency of luminescence is around 200 nm [6,7]. Both mechanisms, composition fluctuation as well as V-pits, may play their role in suppression of non-radiative recombination on dislocations. Another problem, which is still waiting to be fully explained, is why a single InGaN QW (SQW) [8,9] or the deepest QWs in the MQW structure [7,10,11] suffer with a high non-radiative recombination rate. Improvement of luminescence efficiency of InGaN/GaN MQW active region can be achieved by introduction of In containing prelayers such as InGaN layers [8–10], InGaN/GaN superlattice [12,13] or InAlN layers [9]. Although such buffer layers are already widely used in industrial production, there is still a controversy about the mechanism which helps to suppress the Shockley-Read-Hall (SRH) recombination. In this work we would like to suggest new possible hypothesis, which can explain the low PL efficiency of deepest QWs observed by many research groups. Our hypothesis is supported by several indirect proofs.

2. Experimental details

InGaN/GaN MQW samples with different buffer layers were prepared on Aixtron 3 × 2 CCS MOVPE apparatus equipped with LayTec EpiCurveTT system for in situ measurement of reflectivity and

* Corresponding author.
E-mail address: hospodko@fzu.cz (A. Hospodková).

https://doi.org/10.1016/j.jcrysgro.2020.125579
Received 12 October 2019; Received in revised form 28 February 2020; Accepted 29 February 2020
Available online 29 February 2020

temperature. High temperature (HT) buffer layers were grown with trimethylgallium (TMGa) and ammonia (NH_3) precursors with hydrogen as a carrier gas. Low temperature (LT) buffer layers and MQW region was prepared from triethylgallium (TEGa), trimethylindium (TMIn) and ammonia precursors with nitrogen as a carrier gas. Structures were grown on sapphire substrates with standard c-plane orientation. Details about the growth parameters of GaN buffer layer were described in earlier publication [14]. Before the growth of the MQW active region, 1 μm thick GaN layer doped with silicon was added (target doping 1×10^{18} cm^{-3}). The QW were usually grown with nominal thickness 1.5 nm and In concentration close to 5% according to XRD and HRTEM results. Only the sample prepared for secondary ion mass spectroscopy has different structure which will be specified later in the text.

Two types of photoluminescence (PL) excitation were used for sample characterization. The 375 nm excitation wavelength was used for PL measurement to excite all QWs. The resulting PL was detected using a combination of a double monochromator SDL-1 and a GaAs photo-multiplier tube. Synchronous detection technique was implemented by chopping the laser beam at a modulation frequency of about 35 Hz, and by employing a lock-in amplifier. The excitation intensity was 10 W/cm^2, but the absorption coefficient is very low (light is absorbed almost only in thin QWs) so this measurement is very sensitive to the non-radiative SRH recombination rate.

PL spectra of samples A-D, see Fig. 3, were measured at RT with 325 nm excitation wavelength with a confocal microscope (LabRAM HR Evolution, He-Cd laser, objective 74 CG, spot diameter 2 μm).

Secondary ion mass spectroscopy (SIMS) measurements were provided by EAG laboratories.

Atomic force microscopy (AFM) images were taken by Dimension Icon AFM in semicontact mode using ASPIRE tips.

Vacancy type point defects were studied by variable energy positron annihilation spectroscopy (VEPAS) which is a unique non-destructive method for detection of negatively charged or neutral vacancies in semiconductors [15]. VEPAS investigations were carried out on a pulsed slow positron beam MePS [16]. The energy of incident positrons was varied in the range from 1 to 16 keV. It corresponds to the mean positron penetration depth into GaN from 15 to 1250 nm calculated using the Makhovian positron implantation profile [17]. Positron lifetime spectra were measured using a digital spectrometer with time resolution of ≈250 ps (FWHM of resolution function). At least 10^7 positron annihilation events were collected in each positron lifetime spectrum.

3. Results and discussions

The phenomenon of increased non-radiative SRH recombination in QWs situated deeper in a MQW structure is demonstrated in Fig. 1 with comparison of the PL spectra of three MQW structures with 2, 10 or 30 QWs with nominal thickness 1.5 nm and In content close to 5% separated by 5 nm thick GaN barriers according to the HRTEM results.

Two main maxima can be distinguished in the PL spectra, excitonic with the peak wavelength around 430 nm and broad defect related band with maximum around 530 nm. We have found that the defect band is caused by Zn contamination of our samples. It has all typical features of PL caused by Zn contamination [18–20] and additionally, we have proved the Zn contamination of our samples by SIMS, as will be shown bellow. The structures with lower QW number suffer from considerably higher SRH recombination, which we can see for the case of two QWs, where the excitonic peak is almost missing, while for the samples with higher number of QWs the upper QWs have much lower non-radiative recombination rate and the excitonic peak has relatively high intensity. Additionally, we have observed more than ten times enhanced PL intensity in case of excitonic maximum for sample with 30 QWs with respect to sample with 10 QWs. This phenomenon of increased PL efficiency with increased QW number in the structure was

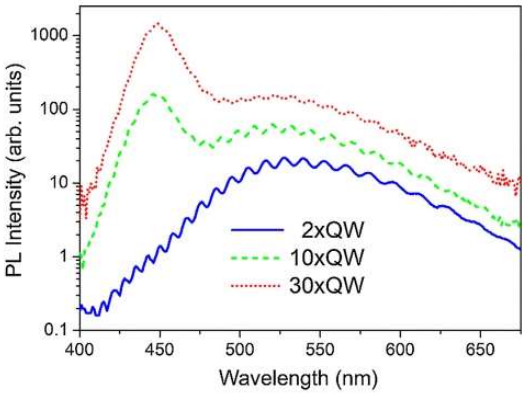

Fig. 1. Room temperature PL spectra (excitation wavelength 375 nm) of three samples with InGaN QWs prepared with the same QW technology differing only in the QW number. The excitonic QW emission is quenched by SRH recombination for sample with two QWs.

observed by many research groups. Three main explanations were suggested in the literature: strain relaxation, enhanced V-pit formation or trapping some unknown types of impurities, which are present on the epitaxial surface during the growth process [8,9].

3.1. V-pit Hypothesis

To distinguish the most probable mechanism, a set of four MQW samples A-D with different types of buffer layers under the upper 10 QWs was prepared. The technological parameters of InGaN/GaN MQW active region were kept the same for all four samples. Sample A has only high temperature (HT) buffer layer grown at H_2 atmosphere and temperature 1050 °C without any prelayer. Sample B, C and D were prepared with different type of prelayers on the top of HT buffer sample. In case of sample B the prelayer consist of 10 InGaN/GaN QWs as the buffer layer for upper ten QWs. Sample C was prepared with low temperature buffer layer grown at N_2 atmosphere and temperature 820 °C. Samples B and C were prepared with intentionally similar V-pit sizes (see Fig. 2), the depth of V-pits is around 10 nm in both cases. The difference is that structure C has no In present in the buffer layer. Structure D was grown with the same growth parameters as structure C (LT buffer), only with H_2 used as a carrier gas for the LT buffer. The surface morphology of the buffer layers is shown in Fig. 2.

PL spectra of samples A-D, see Fig. 3, were measured at RT with 325 nm excitation wavelength. The excitation wavelength of 325 nm was chosen so that 70% of the excitation light is absorbed in the upper 10 QWs (100 nm region). The strongest PL intensity was achieved for sample B with additional 10 QWs (this means 10 + 10 QWs) used as the buffer layer. Its intensity was enhanced more than four times compared to sample A (10 QWs only), although the contribution of the lower 10 QWs in sample B is almost negligible, corresponding to approximately one half of the PL intensity of sample A, because only 30%, not 70%, of incident light is absorbed in the deeper 10 QWs. Weaker PL intensity enhancement was observed when low temperature buffer was added below the active region (sample C). Surprisingly, no enhancement of PL intensity was observed for structure D with low temperature buffer grown with H_2 as a carrier gas, although shallow V-pits were also present in this structure. Since both samples B and C have the same V-pit size, we can conclude that the size of V-pits cannot be the dominant reason of suppressing the SRH recombination.

Similar conclusion that bigger V-pits are not the only reason for the PL enhancement in structures with In containing buffer layers was previously reported in [8]. In that work, a PL of SQW was enhanced by InGaN prelayer, although it was prepared on low dislocation GaN

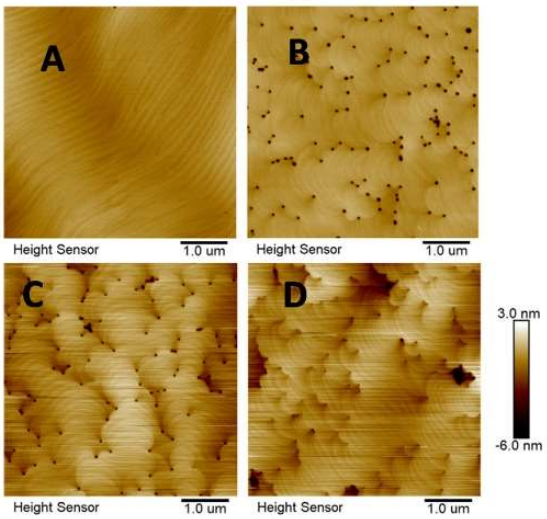

Fig. 2. AFM images of surfaces of different buffer layers, which were used prior to the growth of samples A-D. The V-pit size for buffer layers B and C are similar with the depth around 10 nm.

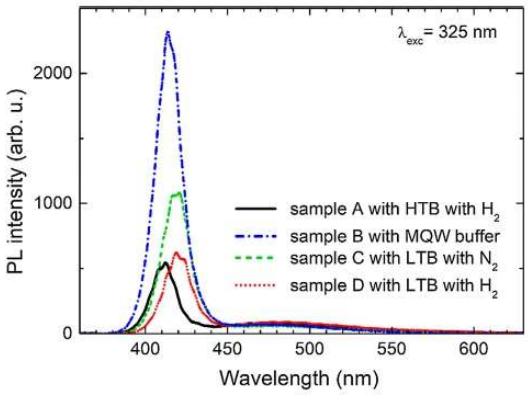

Fig. 3. PL spectra of four samples with 10 InGaN QWs prepared with the same QW parameters and technology of preparation, differing only in underlying buffer layers. The excitation wavelength was 325 nm to obtain luminescence from the upper 10 QWs especially in case of sample B.

substrate without any V-pits.

3.2. In containing layers as traps of unknown defect

According to Haller et al. [8], In containing prelayers serve as traps for some impurity or defect which is present on the epitaxial surface. That is why we have ordered SIMS analysis of our structures with HT and LT buffers for different possible contaminants such as O, C, Si, and Zn. In concentration was measured as the marker of InGaN QWs.

Except Zn concentration profile no unexpected results were obtained, only small increase of oxygen concentration in QWs due to the lower growth temperature. Zn contamination was expected according to the presence of broad defect band in luminescence spectra of our samples [18–20]. Our Zn contamination profile seems to reveal a trapping effect of deepest InGaN QW, see Fig. 4. In agreement with this contamination profile, we have also previously observed enhanced defect band luminescence from the deepest QWs in our structures [21]. However, the Zn contamination cannot be the sought source of non-

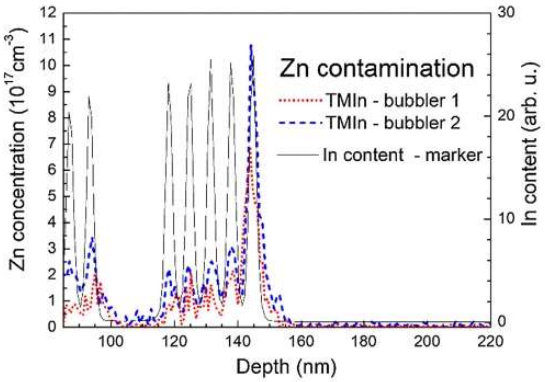

Fig. 4. SIMS measurement of Zn contamination profile in lower QWs of MQW region for samples similar to structure A but with different TMIn sources, uncalibrated In concentration is used as a marker of QWs.

radiative recombination in the deepest InGaN QWs, because Zn is known to form highly efficicent luminesence center [20]. Zn contamination is supposed to originate in precursor contamination, probably TEGa or TMIn). Since the concentration of Zn in the reactor atmosphere is supposed to be the same for all QWs, the first QW has probably higher efficiency of Zn incorporation. Zn atoms incorporate to Ga sublattice. Higher concentration of V_{Ga} on the epitaxial surface can lead to increased Zn incorporation to these unoccupied lattice sites. Another enhancement mechanism could be the Si doping of GaN buffer layer and shift Fermi level at the beginning of QW region.

To study the defect trapping in InGaN QWs we have prepared a special structure for SIMS analysis schematically shown in Fig. 5 containing four separate regions. During the growth of region I, no TMIn was introduced to the reactor, but the temperature cycling was kept identical to the growth of InGaN/GaN QWs. The reason was to confirm

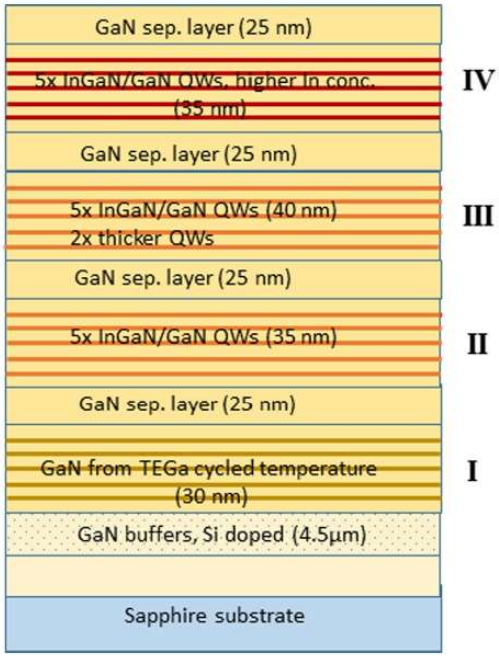

Fig. 5. A scheme of the structure prepared for SIMS analysis.

that temperature cycling during the growth is not responsible for the defect trapping. In region II, III and IV always five QWs were grown with different InGaN QW thicknesses or concentrations. The concentration of In in InGaN QWs was grown to be 0.06 in region I and II and 0.12 in the region III, the QW thickness was 1.6 nm in regions I and III, while in region II it was 3.2 nm.

Depth concentration profiles of several possible contaminants such as H, Zn, O, C, S, Se, Mg, Si were measured on prepared structure by SIMS, concentration profiles of In and Si were used as markers. The Si doped region is identical with HT buffer layer grown at elevated temperature 1050 °C in H_2 atmosphere, In is a marker for three groups of QWs which differ in QW thickness and composition, as described above. Except hydrogen and zinc, concentration of all measured elements was below the detection limit (not presented here). Only the hydrogen and zinc analyses gave us an interesting concentration profiles with an evidence of increased contamination in the two deepest InGaN QW groups, see Fig. 7(b) and (c). The peak value of hydrogen concentration was found to be as high as $1{\cdot}10^{18}$ cm^{-3}. This experiment also proved that the In containing layer serves as a trap for hydrogen containing defects and as a barrier for their further penetration to upper layers, because the enhanced concentration of hydrogen was detected only in the two deepest groups of InGaN QWs. The hydrogen concentration dropped below the detection limit for the upper 5 QWs. Thicker QWs in the second QW group were more effective in trapping the H atoms. We suppose that the detected hydrogen is dominantly present in the structure in the form of V_{Ga}-3H complex defect (Ga vacancy surrounded by three hydrogen atoms), which is predicted to be strong non-radiative defect. According to Dreyer at al. [22], even such a low concentration of hydrogen containing defects as 10^{15} cm^{-3} can be detrimental for QW luminescence. We suppose that the hydrogen is bonded to the nitrogen dangling bonds surrounding the V_{Ga}, see suggested possible hydrogen positions in Fig. 6. However, not all suggested hydrogen positions around V_{Ga} can be occupied, they can be placed on different nitrogen atoms in their bonding or antibonding positions [23]. InGaN layers represent probably something like a potential well for diffusing V_{Ga} so their concentration is higher in InGaN layers than in surrounding GaN. Increased concentration of V_{Ga} can enhance observed Zn or hydrogen incorporation in the deepest QWs, since Zn incorporates to the empty sites of Ga sublattice and hydrogen forms complexes with V_{Ga}.

We have also checked whether the increased concentration of some elements can be induced by lowering the temperature. That is why the region between Si doping and the first InGaN layer (see Fig. 5) was grown at the same temperature cycling as for the MQW growth, but without the presence of TMIn. No enhanced defect trapping was observed in this region (see Fig. 7(b) and (c)). Thus, the presence of In atoms for trapping V_{Ga} seems to be crucial, since V_{Ga} (or any vacancies such as V_{In} or even V_N) would lower the strain in InGaN layers caused by introduction of big In atoms.

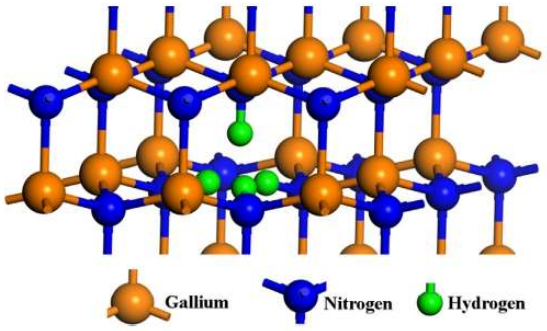

Fig. 6. GaN lattice structure containing V_{Ga}, with suggested possible hydrogen atoms positions bonded to the nitrogen dangling bonds surrounding the V_{Ga}, most probably only three or two hydrogen atoms decorate the V_{Ga}.

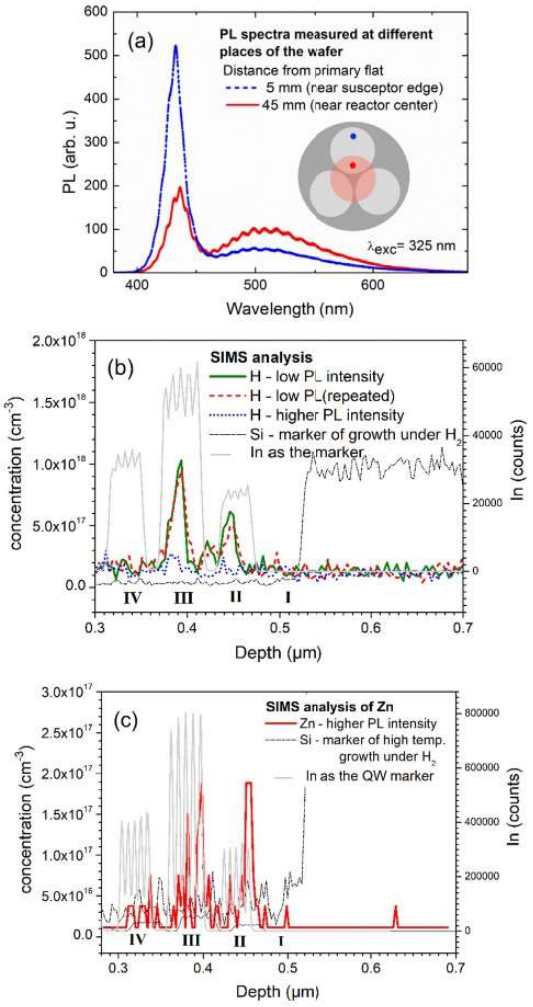

Fig. 7. (a) PL spectra measured at different places on the wafer, see inset, (b) results of SIMS analysis for hydrogen concentration measured at places with the highest and the lowest PL intensity. SIMS analyses were done with a 3 nm step. (c) SIMS profile of Zn contamination, analysis was done with a 1 nm step. The structure was prepared according to scheme in Fig. 6. In atom counts and Si concentration were used as markers in (b) and (c). Drop of Si concentration represents the end of the HT GaN buffer grown in H_2 atmosphere.

Interesting feature is shifted hydrogen profile with respect to the In concentration, which can be noticed in concentration profiles in Fig. 7 (b) and (c). We suppose that this shift can be very probably caused by SIMS method itself, since it is destroying the lattice during measurement and mobile hydrogen can diffuse out of the structure, thus it can be detected earlier than big In atoms. Such hydrogen behavior can also explain increased hydrogen detection in GaN spacer between first and second group of five QWs.

Another possible but rather speculative explanation of shifted hydrogen profile could be anti-correlation of both increased concentration of contaminants, hydrogen and zinc were found dominantly in the deepest ten QWs. The Zn concentration in upper QW group is significantly lower even though the TMIn flow rate was 1.5 times higher. Since we suppose that Zn incorporation is enhanced for QWs with empty Ga sites, suppressed Zn contamination of upper QW group can

also support the hypothesis of trapped V_{Ga} in the deeper QWs.

For unknown reason the PL efficiency of our structures is repeatedly highly inhomogeneous across the wafer as can be demonstrated on PL of sample with 10 QWs (see Fig. 7(a)) which was prepared with the same technological parameters as the first 5 QWs in the structure for the SIMS measurement. We have checked whether this phenomenon is not caused by different density of dislocation or V-pit formation, but we have repeatedly obtained the same value for density of dislocations on both places, which were for screw dislocation density $1.2 \cdot 10^8$ cm^{-2} and for edge and mixed dislocations $5.5 \cdot 10^8$ cm^{-2}. Consequently, also the V-pit density was the same. Since we know, that in some extend, it might be a general problem of 3 × 2 CCS MOVPE reactor, we have checked the hydrogen contamination on two places from the same wafer: with lower PLintensity (near the reactor center - red dashed line) and with higher PL intensity (near the susceptor edge - blue dotted line). Hydrogen was repeatedly detected only on the part of the sample from the region near the reactor center with a very low PL efficiency, see Fig. 7(b) with interesting concentration profile. Hydrogen was detected only in ten deepest QWs, for upper five QWs the hydrogen concentration was under the detection limit although the In concentration of the upper QW group was higher than in the five deepest QWs. We can exclude out diffusion of hydrogen atoms during cooling procedure since cooling process was carried out in H_2 atmosphere. This result is another proof of strong trapping mechanism of the complex defect with hydrogen in the deepest InGaN QWs in the structure.

Since all results suggest that trapping of V_{Ga} and formation of V_{Ga}-nH complex might be responsible for increased non-radiative recombination in the deepest QWs we have decided to prove the hypothesis by variable energy positron annihilation spectroscopy (VEPAS) which is a unique non-destructive method for detection of negatively charged or neutral vacancies in semiconductors [24,25]. This method is capable to detect presence of V_{Ga} in crystal structure. Positrons penetrating to the structure are captured by vacancy defects in crystal structure especially in case when they are negatively charged. The life time of captured positrons is increased due to the lower overlap with electrons. The typical values of positron life time in GaN crystal with V_{Ga} was measured to be 200–250 ps. The positron life time for V_{Ga}-H complex is calculated to be 180 ps and 150 ps for V_{Ga}-2H complex according to [25]. Shorter mean life time of these complex defects indicate lower empty volume of the defect caused by filling the empty space of vacant Ga atom by hydrogen atoms. Positron life time in perfect GaN crystal without any vacancies was published to be around 155 ps [26]. Unfortunately, this technique has very low depth resolution limited by positron diffusion length, which is several hundreds of nanometers. So the spatial resolution is much worse than the QW thickness. Nevertheless, we have measured the mean value of positron life time for structure prepared for SIMS measurement in both places with higher and lower PL efficiency and compared it with values obtained for sample containing only simple GaN layer prepared in hydrogen atmosphere. For GaN layer grown in H_2 atmosphere at the growth temperature 1050 °C (used in our structures as buffer layer) the mean positron life time was measured to be 195 ps. Using the two state simple trapping model [24] and the specific positron trapping rate $\nu_v = 10^{15}$ s^{-1} typical for negatively charged vacancies in semiconductors [15] the concentration of V_{Ga} of $1 \cdot 10^{17}$ cm^{-3} was estimated for high temperature GaN buffer layer.

However, the mean positron life time was 170 ps for sample with InGaN QWs. Such short value indicates presence of V_{Ga}-2H and V_{Ga}-3H complexes or values of crystal with extremely low V_{Ga} concentration. Additionally, shorter mean positron lifetime was detected in the place with lower PL efficiency and higher H contamination (165 ps). Since formation of InGaN layer without any V_{Ga} is not probable and SIMS results indicate high H contamination in layers, the short life time of positrons in InGaN layers derived from VEPAS data give us supporting evidence for the formation of V_{Ga}-nH complexes.

It is important, that V_{Ga}-nH complexes were not confirmed by VEPAS data in GaN buffer layers, only presence of V_{Ga} was derived from measured mean positron life time. We suppose that enhanced formation of V_{Ga}-nH complexes in InGaN layers is caused by lower growth temperature with suppressed decomposition of ammonia. The chemistry of MOVPE process may also explain the discrepancy of our experimental data with theoretical expectation of Dreyers at all [22], where V_{Ga}-nH complexes were expected to be formed only in layers with high In concentration. The chemical reactions could not be included in this theoretical work. However, the chemistry of MOVPE process may significantly influence the defect formation as well as incorporation of contaminants, such as C or H atoms.

With understanding of the mechanism of enhanced non-radiative recombination in the deepest InGaN QWs we can also try to elucidate the origin of PL inhomogeneity of small 3 × 2 CCS reactor. It can be noticed, that in the reactor center not only QW main maximum has lower intensity, but also the Zn related maximum is double enhanced, see Fig. 7(a). This observation suggests that PL inhomogeneity is not caused by less efficient decomposition of ammonia, but rather by enhanced formation of V_{Ga} defects near the reactor center. This conclusion is not in contradiction to the latest reactor producer results, suggesting that some inhomogeneity may be caused by increased temperature of metalorganics coming from uncovered part of susceptor at the reactor center.

4. Conclusion

According to SIMS results and PL measurements, we have concluded that complexes of V_{Ga} with hydrogen atoms probably play a significant role in the non-radiative SRH recombination of the deepest QWs in InGaN/GaN MQW structures. Ga vacancies originate dominantly in the GaN buffer layers grown at higher temperatures and in H_2 atmosphere and are transported by diffusion during the subsequent growth to the InGaN/GaN MQW region or may be even “surfacting” on the epitaxial surface. During the growth of the deepest InGaN layers they are effectively trapped and incorporated because the vacancies decrease the strain in InGaN layers caused by incorporation of big In atoms. Due to the lower growth temperature of InGaN layers and inefficient decomposition of ammonia V_{Ga}-nH complexes are formed according to PAS and SIMS data, which represent non-radiative defects suppressing luminescence efficiency of deepest QWs in the structure. Trapping of V_{Ga} by InGaN layers and formation of V_{Ga}-nH complexes is newly suggested mechanism, which should be considered when explaining why the widely used In containing prelayers help to increase the luminescence efficiency of the InGaN/GaN MQW active region grown above them. However, this mechanism is not excluding other previously reported mechanisms by other research groups. The way how In containing prelayers improve the PL efficiency of InGaN/GaN MQW structures seems to be a complex of mechanisms. Understanding all of them is very important for LED community and can help to develop new improved technology for the growth of InGaN/GaN MQW active region.

Declaration of Competing Interest

The authors declare that they have no known competing financial interests or personal relationships that could have appeared to influence the work reported in this paper.

Acknowledgements

The authors acknowledge the support of the GACR project no. 16-11769S and MSMT project no. NPU LO1603 – ASTRANIT. Partial support of LNSM infrastructure is also gratefully acknowledged. TACR project no. TH02010580.

References

[1] S. Nakamura, M. Senoh, T. Mukai, P-GaN/N-InGaN/N-GaN double-heterostructure blue-light-emitting diodes, Jpn. J. Appl. Phys., Part 2 (32) (1993) L8–L11.

[2] S.F. Chichibu, A. Uedono, T. Onuma, B.A. Haskell, A. Chakraborty, T. Koyama, P.T. Fini, S. Keller, S.P. DenBaars, J.S. Speck, U.K. Mishra, S. Nakamura, S. Yamaguchi, S. Kamiyama, H. Amano, I. Akasaki, J. Han, T. Sota, Origin of defect-insensitive emission probability in In-containing (Al, In, Ga)N alloy semiconductors, Nat. Mater. 5 (2006) 810–816.

[3] M. Gladysiewicz, R. Kudrawiec, Theoretical studies of the influence of structural inhomogeneities on the radiative recombination time in polar InGaN quantum wells, Phys. Status Solidi A 209 (2012) 752–760.

[4] A. Hangleiter, F. Hitzel, C. Netzel, D. Fuhrmann, U. Rossow, G. Ade, P. Hinze, Suppression of nonradiative recombination by V-shaped pits in GaInN/GaN quantum wells produces a large increase in the light emission efficiency, Phys. Rev. Lett. 95 (2005) 127402.

[5] F. Dominec, A. Hospodková, T. Hubáček, M. Zíková, J. Pangrác, K. Kuldová, A. Vetushka, E. Hulicius, Influence of GaN buffer layer under InGaN/GaN MQWs on luminescent properties, J. Cryst. Growth 507 (2019) 246–250.

[6] T. Hubáček, A. Hospodková, K. Kuldová, J. Oswald, J. Pangrác, V. Jarý, F. Dominec, M. Slavická Zíková, F. Hájek, E. Hulicius, A. Vetushka, G. Ledoux, C. Dujardin, M. Nikl, Advancement toward ultra-thick and bright InGaN/GaN structures with a high number of QWs, CrystEngComm 21 (2019) 356–362.

[7] Ch.-Y. Chang, H. Li, Y.-T. Shih, T.-Ch. Lu, Manipulation of nanoscale V-pits to optimize internal quantum efficiency of InGaN multiple quantum wells, Appl. Phys. Lett. 106 (2015) 091104.

[8] C. Haller, J.-F. Carlin, G. Jacopin, D. Martin, R. Butté, N. Grandjean, Burying non-radiative defects in InGaN underlayer to increase InGaN/GaN quantum well efficiency, Appl. Phys. Lett. 111 (2017) 262101.

[9] C. Haller, J.-F. Carlin, G. Jacopin, W. Liu, D. Martin, R. Butté, N. Grandjean, GaN surface as the source of non-radiative defects in InGaN/GaN quantum wells, Appl. Phys. Lett. 113 (2018) 111106.

[10] J. Yang, D.G. Zhao, D.S. Jiang, P. Chen, Z.S. Liu, L.C. Le, X.G. He, X.J. Li, H. Yang, Effects of quantum well number on spectral response of InGaN/GaN multiple quantum well solar cells, Phys. Status Solidi A 211 (2014) 2157–2160.

[11] A. Hospodková, J. Oswald, M. Zíková, J. Pangrác, K. Kuldová, K. Blažek, G. Ledoux, C. Dujardin, M. Nikl, On the correlations between the excitonic luminescence efficiency and the QW numbers in multiple InGaN/GaN QW structure, J. Appl. Phys. 121 (2017) 214505.

[12] G.M. Christian, S. Hammersley, M.J. Davies, P. Dawson, M.J. Kappers, F.C.-P. Massabuau, R.A. Oliver, C.J. Humphreys, Room temperature PL efficiency of InGaN/GaN quantum well structures with prelayers as a function of number of quantum wells, Phys. Status Solidi C 13 (2016) 248–251.

[13] S.J. Leem, Y.C. Shin, K.C. Kim, E.H. Kim, Y.M. Sung, Y. Moon, S.M. Hwang, T.G. Kim, The effect of the low-mole InGaN structure and InGaN/GaN strained layer super lattices on optical performance of multiple quantum well active layers, J. Cryst. Growth 311 (2008) 103–106.

[14] T. Hubáček, A. Hospodková, J. Oswald, K. Kuldová, J. Pangrác, Improvement of luminescence properties of GaN buffer layer for fast nitride scintillator structures, J. Cryst. Growth 46 (2017) 221–225.

[15] R. Krause-Rehberg, H.S. Leipner, Positron Annihilation in Semiconductors vol. 127, Springer-Verlag, Berlin, 1999.

[16] A. Wagner, M. Butterling, M.O. Liedke, K. Potzger, R. Krause-Rehberg, Positron annihilation lifetime and Doppler broadening spectroscopy at the ELBE facility, AIP Conf. Proc. 1970 (2018) 040003.

[17] Ch. Hugenschmidt, Positrons in surface physics, Surf. Sci. Rep. 71 (2016) 547–594.

[18] S. Nakamura, Zn-doped InGaN growth and InGaN/AlGaN double-heterostructure blue-light-emitting diodes, J. Cryst. Growth 145 (1994) 911.

[19] S.J. Chang, et al., Si and Zn co-doped InGaN-GaN white light-emitting diodes, IEEE Trans. Electr. Dev. 50 (2) (2003) 519.

[20] D.O. Demchenko, M.A. Reshchikov, Blue luminescence and Zn acceptor in GaN, Phys. Rev. B 88 (2013) 115204.

[21] A. Hospodková, T. Hubacek, J. Oswald, J. Pangrác, K. Kuldová, M. Hyvl, F. Dominec, G. Ledoux, C. Dujardin, InGaN/GaN structures: effect of the quantum well number on the cathodoluminescent properties, Appl. Phys. Lett. 108 (2016) 141101.

[22] C.E. Dreyer, A. Alkauskas, J.L. Lyons, J.S. Speck, Ch.G. Van de Walle, Gallium vacancy complexes as a cause of Shockley-Read-Hall recombination in III-nitride light emitters, Appl. Phys. Lett. 108 (2016) 141101.

[23] A.F. Wright, Interaction of hydrogen with gallium vacancies in wurtzite GaN, J. Appl. Phys. 90 (2001) 1164.

[24] R.N. West, Positron studies of condensed matter, Adv. Phys. 22 (1973) 263–383.

[25] S.F. Chichibu, A. Uedono, K. Kojima, H. Ikeda, K. Fujito, S. Takashima, M. Edo, K. Ueno, S. Ishibashi, The origins and properties of intrinsic nonradiative recombination centers in wide bandgap GaN and AlGaN, J. Appl. Phys. 123 (2018) 161413.

[26] S. Hautakangas, I. Makkonen, V. Ranki, M.J. Puska, K. Saarinen, Direct evidence of impurity decoration of Ga vacancies in GaN from positron annihilation spectroscopy, Phys. Rev. B 73 (2006) 193301.

Journal of Crystal Growth 565 (2021) 126151

Contents lists available at ScienceDirect

Journal of Crystal Growth

journal homepage: www.elsevier.com/locate/jcrysgro

Luminescence redshift of thick InGaN/GaN heterostructures induced by the migration of surface adsorbed atoms

Tomáš Vaněk [a,b,*], František Hájek [a,c], Filip Dominec [a], Tomáš Hubáček [a], Karla Kuldová [a], Jiří Pangrác [a], Tereza Košutová [a], Pavel Kejzlar [b], Petr Bábor [d,g], Artur Lachowski [e,f], Alice Hospodková [a]

[a] Institute of Physics CAS, v.v.i, Cukrovarnická 10, 16200 Prague 6, Czech Republic
[b] Technical University of Liberec, Studentská 2, 46117 Liberec, Czech Republic
[c] Faculty of Faculty of Nuclear Sciences and Physical Engineering, Czech Technical University in Prague, Břehová 7, 11519 Praha 1, Czech Republic
[d] CEITEC - Central European Institute of Technology, Brno University of Technology, Purkyňova 656/123, 61200 Brno, Czech Republic
[e] Institute of High Pressure Physics, Polish Academy of Sciences, Sokolowska 29/37, 01142 Warsaw, Poland
[f] Faculty of Materials Science and Engineering, Warsaw University of Technology, Wołoska 141, 02507 Warsaw, Poland
[g] Institute of Physical Engineering, Faculty of Mechanical Engineering, Brno University of Technology, Purkyňova 123, 61200 Brno, Czech Republic

ARTICLE INFO

Communicated by T. Paskova

Keywords:
A1. Characterization
A1. Growth models
A3. MOVPE
B1. Nitrides
B3. Scintillators

ABSTRACT

Nitride heterostructures with an extremely high number of InGaN/GaN multiple quantum wells (MQWs) were grown and studied by multiple techniques. Large redshift (282 meV) in photoluminescence (PL) spectra was observed with an increasing number of quantum wells (QWs) in the structure from 10 to 60. From the comparison of structures grown on sapphire and GaN substrates, the phenomenon of giant redshift is explained. A theory based on the surface migration of the adsorbed atoms from the semi-polar V-pit facets to the c-plane facets is suggested and proven by several experimental techniques including scanning transmission electron microscopy (STEM), secondary ion-mass spectroscopy (SIMS), secondary electron microscopy (SEM), white light interferometry (WLI), and spectrally and spatially resolved cathodoluminescence (SSRCL). Finally, a change in the surface morphology caused by the growing size of the V-pits and the transformation of the c-plane surface areas is discussed.

1. Introduction

Nitride semiconductor heterostructures have been widely studied for almost three decades since the discovery of the first blue LEDs [1]. They have been vastly utilized in the industry due to their excellent properties such as high radiation resistance, high exciton binding energy, high luminescence efficiency at room temperature, and their suitability for high power and high-frequency applications [2,3]. Nitride heterostructures are mainly grown by metalorganic vapor phase epitaxy (MOVPE). The advantage of MOVPE technology is that it allows us to tune the luminescence and morphology parameters of the final structure very accurately. Recently, the InGaN/GaN heterostructures with the thick active MQW region have become important for various luminescence applications as well as solar cell applications, where the demands on a large detection volume for sufficient radiation stopping power have emerged [4–7]. Although InGaN/GaN heterostructures have been studied in detail, phenomena coming with the thick structures have not been described yet. Some of them are connected with well-known surface artifacts called V-pits.

V-pits in InGaN/GaN heterostructures are known for their positive effect on the light yield in the LEDs as they increase the light extraction efficiency and isolate carriers in the QW from threading dislocations [8]. However, for thick active layers, V-pits are oversized since their size is growing with the active layer thickness [9]. In this paper, the results obtained from structures with different thicknesses of the MQW active region ranging from 250 nm for 10 QWs to 2μm for 80 QWs are shown. The discussion is focused on a surface morphology change due to the enlargement of V-pits. Finally, a very unexpected influence on the luminescence properties of QWs is discussed.

* Corresponding author at: Institute of Physics CAS, v.v.i, Cukrovarnická 10, 16200 Prague 6, Czech Republic.
E-mail address: vanekt@fzu.cz (T. Vaněk).

https://doi.org/10.1016/j.jcrysgro.2021.126151
Received 30 January 2021; Received in revised form 6 April 2021; Accepted 14 April 2021
Available online 20 April 2021

2. Experimental

The InGaN/GaN MQW heterostructures were prepared in an Aixtron 3x2″ CCS MOVPE system equipped with Laytec EpiCurveTT in situ measurement. We prepared six samples with the number of QWs ranging from 10 to 80 grown on a sapphire substrate (S10, S20, S30, S40, S60, S80) and three samples grown on GaN substrate (G40, G60, G80). All samples were grown under the same growth conditions except the nucleation and coalescence layer that are not necessary on GaN substrate. C-oriented Al_2O_3 substrates were firstly baked out at 1050 °C for 5 min before the growth and then nitrified by NH_3. The 25 nm thick GaN nucleation layer was grown at 540 °C and covered by a 3.9 μm thick GaN buffer layer grown at 1050 °C with an upper 0.8 μm thick layer doped by Si (the target Si concentration was 1×10^{18} cm^{-3}). The MQW active region contains n × 5 (n = 2, …,16) pairs of InGaN QWs and GaN barriers separated from each other by 26 nm thick GaN spacers, see the scheme of the structure in Fig. 1. The MQW structure was finally covered by a 20 nm thick GaN cap layer. For the sample with 10 QWs, the structure parameters were determined by X-ray diffraction analysis (XRD), the indium concentration in QWs was 8.8 ± 0.7%, QWs thickness 1.9 ± 0.1 nm (grown at 760 °C), and the GaN barrier thickness 18 ± 1 nm (grown at 870 °C). TMGa and SiH_4 with H_2 carrier gas were used as precursors for nucleation and buffer layer, while TMIn and TEGa with N_2 carrier gas were used for the MQW region growth to suppress the carbon incorporation [10,11]. The nitrogen source was NH_3 during the whole growth.

The PL data were obtained by LabRAM HR Evolution spectrometer equipped with He-Cd excitation laser (λ = 325 nm) and a reflective microscope objective illuminating a 2 μm spot. We used ION-TOF TOF. SIMS 5 instrument for In depth profiling. All depth profiles were performed in dual beam mode using 15 keV Bi_3^+ liquid metal ion gun (LMIG) as a primary ion source, a 1 keV oxygen ion sputter source both mounted at 45° with respect to the sample surface and an electron flood gun. Two scanning electron microscopes were used for cathodoluminescence and morphological characterization. Philips XL30 ESEM equipped with GaAs photomultiplier tube and homemade inbuilt grid monochromator with a spectral window less than 20 nm and tunable acceleration voltage 2–30 keV for spectrally and spatially resolved cathodoluminescence and UHR FE-SEM ZEISS Ultra Plus were used for detailed surface visualization. The topographical information was also supported by white light interferometer Zygo – New View 7200 which has nanometric accuracy in the z-direction. Finally, the HAADF-STEM (high-angle annular dark-field STEM) figures were obtained by FEI TECNAI G2 F20 S-TWIN microscope operating at 200 kV equipped with a Fischione 3000 HAADF detector, and the SmartLab of Rigaku was used for XRD.

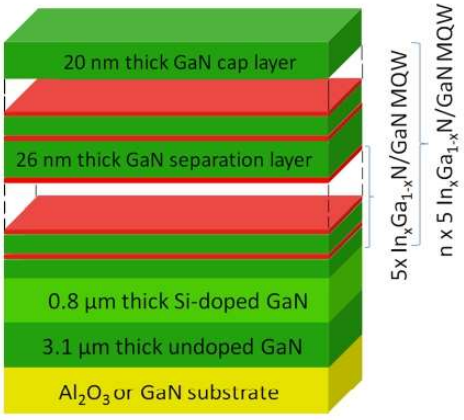

Fig. 1. Scheme of the structure grown by MOVPE with the active region composed from n × 5 (n = 2, …,16) pairs of InGaN QWs and GaN barriers.

3. Results and discussion

We have observed an almost linear luminescence redshift by 282 meV with the increasing number of QW from 10 to 60 QWs (Fig. 2). The excitation wavelength used for this measurement was 325 nm, corresponding to the photon energy above the bandgap of GaN, so the penetration depth of photons is around 100 nm, and only approximately the top five QWs should be excited. Generally, the luminescence redshift in the QWs can be caused by an increasing In concentration or an increasing thickness of QWs.

However, the amount of In in the QWs, measured by SIMS on the 20 QWs sample, seems to be decreasing in the direction towards the surface, see Fig. 3c. The average amount of In in each stack of five QWs separated by GaN spacers was counted relatively to the total intensity of all detected ions. Concretely, we normalized integrals of the In intensities obtained in the stacks by the total intensities of all ions in the same depth regions. The In profile representing MQW structure deteriorates with the depth of measurement as the background In concentration in barriers and spacers increases, see Fig. 3a. The major sources of this signal degradation are probably surface V-pits (see Fig. 4). In general, a mixing of atoms in the material occurs during sputtering. In the case of such a rough surface, it leads to the pushing of In atoms from semi-polar QWs on the sidewalls of V-pits to c-plane areas. Therefore, these visible changes of In amounts between QWs in a single stack, thicknesses of QWs, or amounts of In in the spacers are misleading and cannot be evaluated from the SIMS results. Even if we use the signal only from the c-plane areas (blue spots in Fig. 3b). This is also the reason why we don't present SIMS results from samples grown on the sapphire substrate with more than 20 QWs.

V-pits naturally cover the surface of InGaN/GaN MQW because they open on the top of the threading dislocations when the temperature ramps-down before the MQW growth, and nitrogen is used as carrier gas [6]. The temperature decrease and absence of hydrogen are necessary for In incorporation into GaN. Although V-pits improve optical properties of the structure, as was written earlier, they also reduce the volume of scintillating material. The reduction of the c-plane surface area (marked in yellow ovals in Fig. 4) due to the growing size of V-pits with higher QW number causes the fading luminescence intensity of top QWs in samples with the high number of QWs, see Fig. 2a (S40, S60) and [9]. Moreover, a new generation of V-pits (see zoom in S30 image of Fig. 4) opens after approximately 15 QWs, probably as a result of strain relaxation of MQW structure. Their opening further accelerates the roughening of the surface, which we can observe as a sudden change of reflectance curve in the reflectance measurement of Fig. 4. The luminescence intensity of samples with the small number of QWs (S10, S20) is also low, but the reason being most probably point defects penetrating from the GaN buffer layer as was suggested recently [12–14].

The interpretation of the SIMS signal taken from the sample with such a rough surface is difficult. Therefore, we performed the same measurement of sample grown on the GaN substrate to be certain about the In amount trend in the QWs stacks. GaN buffer layer was grown directly on the GaN substrate because there is no lattice mismatch between the substrate and the MOVPE-grown layer. The consequence is about two orders lower threading dislocation density (10^6 cm^{-2} in comparison with 10^8 cm^{-2} during growth on the sapphire substrate) and lower V-pit density, see SEM picture of the surface in Fig. 5b. Consequently, the indium profile in SIMS (Fig. 5a) deteriorates much less for the sample grown homoepitaxially on GaN, than for the sample on the sapphire substrate. Even the measured In signal in spacers between MQW stacks declines by more than two orders comparing to QWs, which makes the average amount of In between QWs stacks more precise and comparable. The same linear decreasing trend of In amount in the QWs stacks towards the surface was observed (Fig. 5c). Please note that the sample in Fig. 5c has twice more QWs than the sample in Fig. 3c.

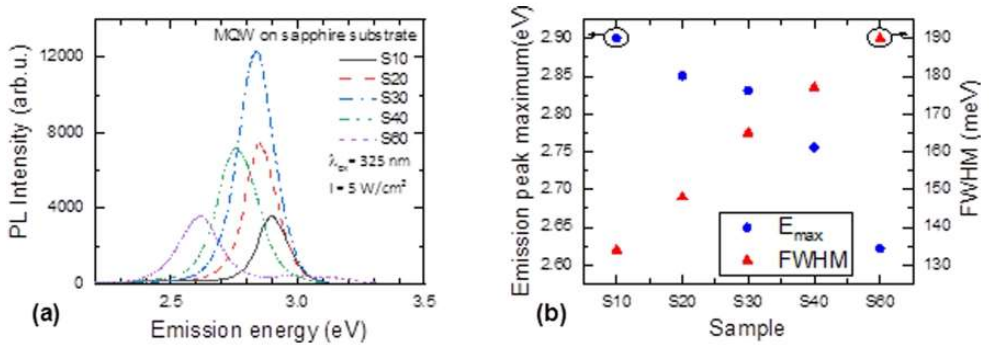

Fig. 2. **(a)** PL spectra of samples with various numbers of QWs prepared on sapphire substrates. **(b)** dependence of the emission energy and full width at half maximum (FWHM) of QWs PL peak on the QWs number.

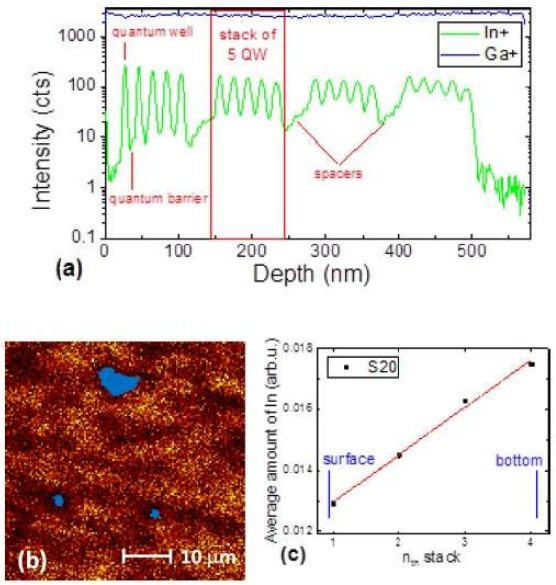

Fig. 3. **(a)** SIMS depth profile of In and Ga atoms of sample S20, **(b)** blue marked c-plane regions from that the profile was taken, and **(c)** the average amount of In in each stack of five QWs. (For interpretation of the references to color in this figure legend, the reader is referred to the web version of this article.)

Furthermore, the CL with 5 kV acceleration voltage (low penetration depth of primary electrons) also confirms the higher emission energy of top QWs compared to the QWs near the substrate in the sample with GaN substrate, see Fig. 5d. The origin of the In decrease may be both a physical or a technological problem and will be the topic of future research, but it disproves that the luminescence redshift, observed on samples grown on sapphire, is due to the higher In content in top QWs.

Another reason for the observed redshift can be the increased thickness of top QWs, but it is impossible to obtain such information from SIMS results. HAADF-STEM measurement of sample S80 (Fig. 6a) shows an increasing thickness of MQW stacks and also GaN spacers between them. It is known that V-pits grow in size because the GaN growth rate in the semi-polar direction is lower than in the c-plane direction [15]. Herein, we explain the increasing thickness of upper layers by the migration of surface adsorbed atoms from the semi-polar facets of V-pits to c-plane facets due to the difference in incorporation rates of both In and Ga adsorbed atoms, see Fig. 6c. A similar PL shift induced by the surface migration of atoms has already been published for trench defects [16]. In the case of the analogous sample grown in the same run but on the GaN substrate (resulting in fewer V-pits) (Fig. 6b), the thickness of spacers and MQW stacks does not change. This proves that V pits and the connected migration are responsible for thickness changes of GaN spacers and MQW stacks. In addition, the declining integrity of upper QWs confirms the decreasing In trend measured by SIMS.

Except for the increasing overall thickness, these migrating atoms also transform the morphology of the c-plane facets to a valley-like shape with thicker regions on the borders of V-pits and thinner in the center of the c-plane, see Fig. 7a and b.

Fig. 8b shows the SSRCL map measured at emission energy 2.67 eV. The c-planes appear bright at this energy. The situation is different at a lower energy (Fig. 8a): bright lines surrounding c-plane facets are clearly resolved at energy 2.51 eV. This is in perfect agreement with the aforementioned observations from SEM and WLI suggesting thicker c-plane QWs in the vicinity of V-pits. The acceleration voltage was set to 3 kV (penetration depth around 60 nm). Therefore electrons excite only top QWs. The increasing inhomogeneity of QW thickness in one QW layer leading to the increasing range of emission energy also explains the increasing FWHM that has been observed in Fig. 2b. Black regions in both Fig. 8a and 8b are regions where electrons impact the surface of V-pits and excite semi-polar QWs on their sidewalls. The thickness of the semi-polar QWs is about one third of the c-plane QWs, so their luminescence energy is shifted almost to UV [17]. Consequently, the SSRCL image measured with the emission energy of 3 eV is color-inverse to the SSRCL images set to exciton emission energy of the c-plane QWs (compare the c-plane area marked by the yellow oval in Fig. 8c with other SSRCL images and SEM image).

4. Conclusion

We have investigated the luminescence and morphology properties of thick InGaN/GaN MQW heterostructures. With the increasing size and density of V-pits, luminescence intensity from top QWs decreases because of the reduction of scintillation volume. Simultaneously, the increased surface area of the semi-polar facets on V-pit sidewalls results in thicker c-plane facets. We suggest that it is due to the atom migration of both In and Ga adsorbed atoms from the semi-polar facets with a low incorporation rate toward c-plane facets. The surface transformation to the valley-like morphology was well observable by WLI and SEM and confirmed by SSRCL. The thickness of QWs grows especially in the regions surrounding V-pits which results in the large 282 meV PL redshift of top QWs on the sample with 60 QWs in comparison with the 10 QWs sample. The theory of atom migration from V-pit surfaces has also been supported by the HAADF-STEM results. They showed the increasing thickness of GaN spacers and MQW regions with the rising number of

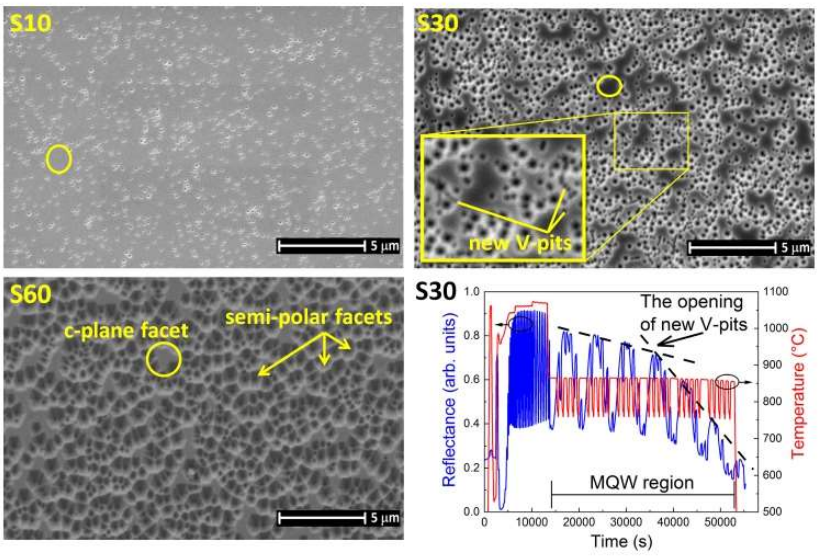

Fig. 4. Surface of samples with the different number of QWs S10, S30, and S60 (different thickness ofMQW region and sizes of V-pits) measured by SEM and in-situ measurement of reflectance and surface temperature of S30 during the growth.

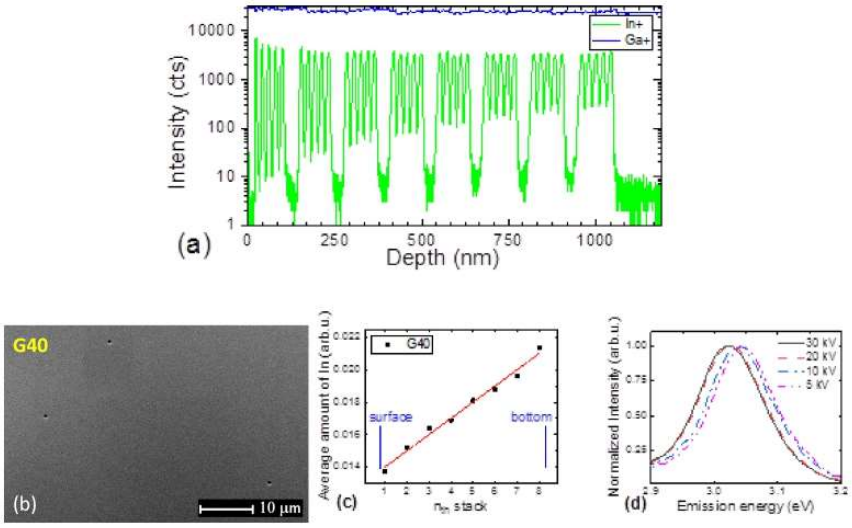

Fig. 5. **(a)** SIMS depth profile of In and Ga atoms of sample G40 grown on GaN substrate, **(b)** SEM picture of the same sample, **(c)** average concentration of In in each stack of five QWs, and **(d)** CL spectra of c-plane QWs exciton emission for different acceleration voltages.

QWs for the sample grown on the sapphire substrate, while in the case of sample grown on the GaN substrate with fewer V-pits the thicknesses have not changed. The HAADF-STEM measurement of the sample G80 also confirmed the surprising decreasing trend of In amount in QWs towards the surface, which has been firstly observed by SIMS. This phenomenon will be a topic for further research.

Structures with high QW number have potential application in detector structures like sollar cells or scintillators. The increased roughness has a positive effect on light extraction in scintillator applications. On the other hand, the light guide properties of the structure deteriorate. Furthermore, the radiation stopping power of the structure decreases. Thus some technological V-pit' size controlling during the growth would be useful. In the case of solar cell applications, we believe that the rough surface can enhance light absorption. Thinner QWs on the V-pit facets can also help to carrier diffusion to contacts. However, this problem needs to be studied in more detail.

CRediT authorship contribution statement

Tomáš Vaněk: Conceptualization, Investigation, Data curation, Writing - original draft. **František Hájek:** Investigation, Writing - review & editing. **Filip Dominec:** Methodology, Software, Writing - review & editing. **Tomáš Hubáček:** Conceptualization, Investigation, Writing - review & editing. **Karla Kuldová:** Investigation, Writing - review & editing. **Jiří Pangrác:** Investigation, Writing - review & editing. **Tereza Košutová:** Investigation, Writing - review & editing. **Pavel**

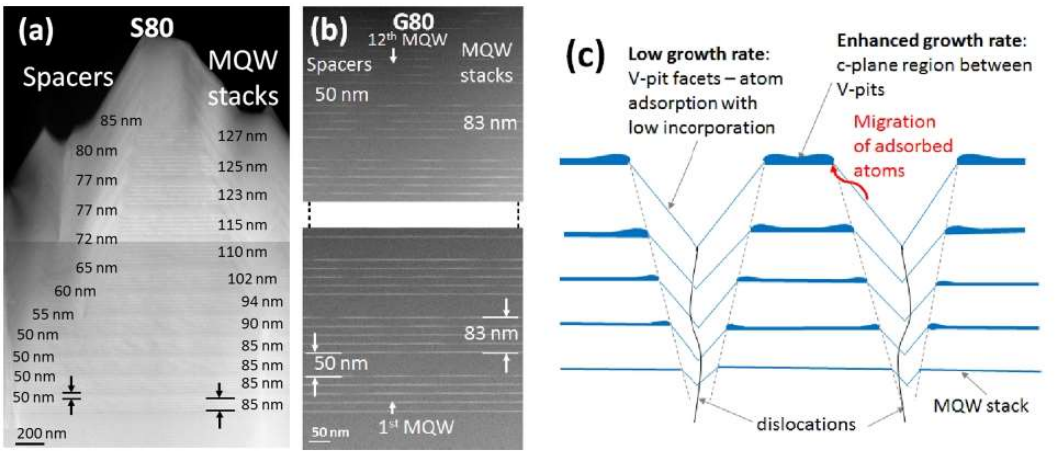

Fig. 6. HAADF-STEM images with marked thicknesses of GaN spacers and InGaN/GaN MQW stacks of sample S80 **(a)**, respectively sample G80 **(b)**. **(c)** scheme of the MQW region geometry influenced by increased V-pit size in upper QWs.

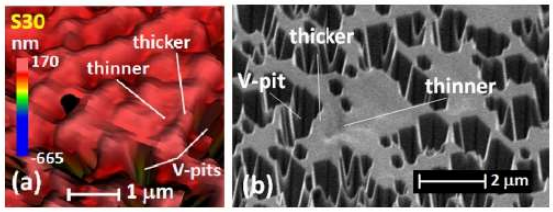

Fig. 7. **(a)** WLI image of the surface of sample S30 with valley-like c-plane surface morphology, **(b)** SEM surface image of the same sample taken under an angle for highlighting of thicker borders of c-planes.

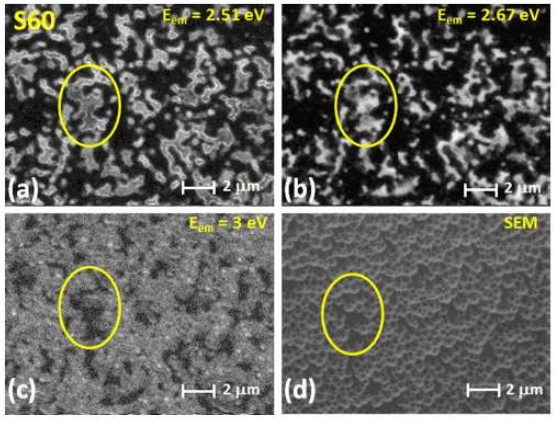

Fig. 8. SSRCL images of sample S60 for acceleration voltage 3 kV and emission energies set to **(a)** thicker regions of c-plane QWs close to V-pits, **(b)** the center of c-plane regions, **(c)** semi-polar QWs on the sidewalls of V-pits, and **(d)** SEM image of the same sample area.

Kejzlar: Investigation. **Petr Bábor:** Investigation, Writing - review & editing. **Artur Lachowski:** Investigation, Writing - review & editing. **Alice Hospodková:** Conceptualization, Writing - review & editing, Supervision.

Declaration of Competing Interest

The authors declare that they have no known competing financial interests or personal relationships that could have appeared to influence the work reported in this paper.

Acknowledgment

The authors acknowledge for partial support of the Operational Programme Research, Development and Education financed by European Structural and Investment Funds and the MEYS CR (Project No. SOLID21 CZ.02.1.01/0.0/0.0/16_019/0000760) and for support of TACR project FW03010298. CzechNanoLab project LM2018110 funded by MEYS CR is also gratefully acknowledged for the financial support of the measurements at CEITEC Nano Research Infrastructure. We also thank prof. Holy for writing a fitting program for X-ray analysis.

References

[1] S. Nakamura, Growth of $In_xGa_{(1-x)}N$ compound semiconductors and high-power InGaN/AlGaN double-heterostructure violet-light-emitting diodes, Microelectron. J. 25 (1994) 651–659, https://doi.org/10.1016/0026-2692(94)90131-7.
[2] S. Nakamura, Background Story of the Invention of Efficient InGaN Blue-Light-Emitting Diodes (Nobel Lecture), Angew. Chem. Int. Ed. 54 (27) (2015) 7770–7788.
[3] M.H. Crawford, LEDs for Solid-State Lighting: Performance Challenges and Recent Advances, IEEE J. Select. Topics Quantum Electron. 15 (4) (2009) 1028–1040.
[4] N.G. Young, et al., High performance thin quantum barrier InGaN/GaN solar cells on sapphire and bulk (0001) GaN substrates, Appl. Phys. Lett. 103 (2013) 173903, https://doi.org/10.1063/1.4826483.
[5] P. Lecoq, Development of new scintillators for medical applications, Nucl Instrum Methods Phys Res Sect. A 809 (2016) 130–139, https://doi.org/10.1016/j.nima.2015.08.041.
[6] A. Hospodková, et al., InGaN/GaN Structures: Effect of the Quantum Well Number on the Cathodoluminescent Properties, Phys. Status Solidi B 255 (2018) 1700464, https://doi.org/10.1002/pssb.201700464.
[7] R.M. Turtos, et al., Light yield of scintillating nanocrystals under X-ray and electron excitation, J. Lumin. 215 (2019) 116613, https://doi.org/10.1016/j.jlumin.2019.116613.
[8] A. Hangleiter, et al., Suppression of Nonradiative Recombination by V-Shaped Pits in GaInN/GaN Quantum Wells Produces a Large Increase in the Light Emission Efficiency, Phys. Rev. Lett. 95 (2005) 127402, https://doi.org/10.1103/PhysRevLett.95.127402.
[9] Tomáš Hubáček, Alice Hospodková, Karla Kuldová, Jiří Oswald, Jiří Pangrác, Vítězslav Jarý, Filip Dominec, Markéta Slavická Zíková, František Hájek, Eduard Hulicius, Alexej Vetushka, Gilles Ledoux, Christophe Dujardin, Martin Nikl, Advancement toward ultra-thick and bright InGaN/GaN structures with a high number of QWs, CrystEngComm 21 (2) (2019) 356–362.
[10] A. Saxler, D. Walker, P. Kung, X. Zhang, M. Razeghi, J. Solomon, W.C. Mitchel, H. R. Vydyanath, Comparison of trimethylgallium and triethylgallium for the growth of GaN, Appl. Phys. Lett. 71 (22) (1997) 3272–3274.

[11] Keun-Man Song, Dong-Joon Kim, Yong-Tae Moon, Seong-Ju Park, Characteristics of GaN grown by metalorganic chemical vapor deposition using trimethylgallium and triethylgallium, J. Cryst. Growth 233 (3) (2001) 439–445.
[12] C. Haller, et al., GaN surface as the source of non-radiative defects in InGaN/GaN quantum wells, Appl. Phys. Lett. 113 (2018) 111106, https://doi.org/10.1063/1.5048010.
[13] C. Haller, et al., Burying non-radiative defects in InGaN underlayer to increase InGaN/GaN quantum well efficiency, Appl. Phys. Lett. 111 (2017) 262101, https://doi.org/10.1063/1.5007616.
[14] A. Hospodková, et al., A secret luminescence killer in deepest QWs of InGaN/GaN multiple quantum well structures, J. Cryst. Growth 536 (2020) 125579, https://doi.org/10.1016/j.jcrysgro.2020.125579.
[15] T. Wunderer, et al., Fabrication of 3D InGaN/GaN structures providing semi-polar GaN planes for efficient green light emission, Phys. Status Solidi C 6 (2009) S490–S493, https://doi.org/10.1002/pssc.200880867.
[16] F.C.-P. Massabuau, et al., The impact of trench defects in InGaN/GaN light emitting diodes and implications for the "green gap" problem, Appl. Phys. Lett. 105 (2014) 112110, https://doi.org/10.1063/1.4896279.
[17] S. Kurai, et al., Nanoscopic spectroscopy of potential barriers formed around V-pits in InGaN/GaN multiple quantum wells on moderate temperature GaN pit expansion layers, J. Appl. Phys. 124 (2018) 083107, https://doi.org/10.1063/1.5043578.